Master's thesis

NTNU
Norwegian University of Science and Technology
Faculty of Information Technology and Electrical Engineering
Department of Engineering Cybernetics

Herman Biørn Amundsen

Robust Nonlinear ROV Motion Control for Autonomous Inspections of Aquaculture Net Pens

Master's thesis in Cybernetics and Robotics
Supervisor: Kristin Ytterstad Pettersen, ITK
January 2020

NTNU
Norwegian University of
Science and Technology

Herman Biørn Amundsen

Robust Nonlinear ROV Motion Control for Autonomous Inspections of Aquaculture Net Pens

Master's thesis in Cybernetics and Robotics
Supervisor: Kristin Ytterstad Pettersen, ITK
January 2020

Norwegian University of Science and Technology
Faculty of Information Technology and Electrical Engineering
Department of Engineering Cybernetics

NTNU
Norwegian University of
Science and Technology

Problem Formulation

Thesis description:

The Artifex project is developing technologies for future remote operations at fish farms where the main objective is to develop robots for regular remote inspection, maintenance and repair operations without onsite personnel. The ROV used in the Artifex project requires proper controllers to accomplish the assigned tasks automatically, and choosing the right control strategy may determine the success of the operation. The task of the thesis is to develop new and improve existing control and guidance systems for a ROV conducting robust and autonomous inspections of aquaculture net pens.

The following subjects should be considered:

1. Literature review in relation to:
    (a) Maneuvering controllers and models, with focus on disturbance compensation
    (b) Sea state at exposed aquaculture locations
    (c) Bathymetric SLAM
2. Suggest new control and guidance systems, as well as improving existing control and guidance systems with respect to robustness.
3. Perform an analysis of the stability properties of the suggested control and guidance systems.
4. Software validation of the controllers in FhSim.
5. Field validation of the controllers.

Supervisor: Prof. Kristin Ytterstad Pettersen, Dept. of Engineering Cybernetics, NTNU
Co-supervisor: Dr. Walter Caharija, SINTEF Ocean

Acknowledgment

This thesis is carried out at the Norwegian University of Science and Technology (NTNU) as the final requirement of the 5-year MSc program Cybernetics and Robotics. It has been written over the last six months under the supervision of Professor Kristin Ytterstad Pettersen and Walter Caharija. The thesis has been carried out as a collaboration with SINTEF Ocean as part of the Artifex project, and continuous the work of my specialization thesis, delivered in the summer of 2019. The contributions of this thesis is listed below.

The net pen geometry approximation method and guidance law has been developed and implemented by me in collaboration with Caharija. I have independently developed and implemented the velocity controllers and different sliding mode controllers presented.

The six degree-of-freedom ROV model used in simulations has been implemented in FhSim by Caharija and Per Rundtop, former research engineer at SINTEF Ocean. A DVL sensor model has also been implemented by Caharija and Rundtop. The thruster allocation has been developed by Rundtop. The PID heading and depth controllers have been developed by Caharija.

A draft to a scientific paper which is to be submitted to IEEE Journal of Oceanic Engineering has been written in collaboration with Caharija and Prof. Pettersen. The paper is included in Appendix B.

This lasts months have been exciting, and I have learned tremendous. I would like to thank my supervisor Professor Kristin Ytterstad Pettersen for trusting me with this thesis and for valuable feedback throughout the last year. Furthermore, I owe a great deal to my co-supervisor Walter Caharija. Your enthusiasm and uplifting spirits, as well as your knowledge, have been a key motivation for me. I would also like to thank SINTEF Ocean for giving me the opportunity to work on such an exciting problem, and helping me with resources needed. Thanks also go out to my family for their support and to all of my friends in Trondheim for making these 5 years memorable.

Trondheim, January 2020

Herman Biørn Amundsen

Abstract

This thesis presents a method for controlling a remotely operated vehicle (ROV) to autonomously traverse and inspect an aquaculture net pen. The method is based on the measurements from a Doppler velocity log (DVL), and uses these measurements to estimate the ROV attitude and position relative to the net pen. The traveled distance of the 4 hydro-acoustic DVL beams is measured, and from these four measurements, the net pen surface is approximated as a plane. The ROV heading and distance relative to the approximated net pen surface are used as inputs in a guidance law.

The proposed nonlinear guidance law is based upon the nonlinear line-of-sight (LOS) guidance law, and utilizes that the ROV is fully actuated in the north-east plane to guide the ROV to the desired path independent of the vehicle heading. Through Lyapunov analysis, the asymptotic convergence of the crosstrack error is proven. Finally, for control of the vehicle states the thesis proposes both a 1st order sliding mode control law and a super-twisting algorithm with adaptive gains, and through simulations the performance of the control laws are compared to that of classical PID control.

The system have been designed and tested using the simulation platform FhSim, provided by SINTEF Ocean. In simulations, the ROV performs well, and is able to accurately traverse the net pen in the presence of both currents and waves. Furthermore, practical experiments using an Argus Mini ROV have been conducted both at a water basin and at SINTEF ACE, a full scale aquaculture laboratory. The results from the experiments verifies the performance of the presented method, and the ROV traverses the net pen successfully.

Sammendrag

Denne oppgaven presenterer en metode for a kontrollere en fjernstyrt undervannsbåt (ROV) til å autonomt traversere og inspisere en not for bruk i fiskeoppdrett. Metoden er basert på Doppler velocity log- (DVL) målinger, og bruker disse målingene til å estimere ROVens posisjon og orientering relativt til nota. Reiseavstanden til de 4 hydroakustiske DVL-strålene er målt, og fra disse fire målingene så er notoverflaten approksimert som et plan. ROVens pekeretning og avstand til den approksimerte notoverflaten blir videre brukt i en guidingslov.

Den foreslåtte ulineære guidningsloven er basert på siktlinje-banefølging (LOS), og bruker at ROVen er full-aktuert i det horisontale planet til å styre ROVen mot den ønskede banen uavhengig av ROVens pekeretning. Gjennom Lyapunov-analyse så blir det vist at ROVens distanse til referansebanen konvergerer mot null. For å regulere tilstandene til ROVen, så foreslås både en 1. ordens sliding mode-regulator og en super-twisting algoritme med adaptive pådrag, og gjennom simuleringer er responsen til de foreslåtte regulatorene sammenlignet med klassisk PID-regulatorer.

Systemet har blitt designet og tested via simuleringsplattformen FhSim, utviklet av SINTEF Ocean. ROVen presterer bra under simuleringer, og er i stand til å presist følge nota under påvirkning av både bølger og havstrøm. Videre har det blitt gjennomført praktiske eksperimenterer både i basseng, samt på SINTEF ACE, et fullskala fiskeoppdrettslaboratorium. Eksperimentene viser at ROVen er i stand til å autonomt følge nota.

Contents

I Introduction 1

1 Introduction 3
- 1.1 Motivation . . . 3
- 1.2 Outline . . . 5

II Theory 7

2 Marine Craft Dynamics 9
- 2.1 Notation . . . 9
- 2.2 Reference Frames . . . 9
- 2.3 Vectorial Notation . . . 10
  - 2.3.1 Generalized Coordinates . . . 11
- 2.4 Kinematics . . . 11
  - 2.4.1 Kinematic Subsystems . . . 12
- 2.5 Kinetics . . . 12
  - 2.5.1 Hydrodynamics . . . 13
  - 2.5.2 Restoring Forces . . . 14
- 2.6 Course, Heading and Crab Angle . . . 14
- 2.7 Environmental Forces and Moments . . . 15
  - 2.7.1 Wave-induced Forces and Moments . . . 15
  - 2.7.2 Ocean Currents . . . 16
- 2.8 Actuation . . . 16
- 2.9 Summary . . . 17

3 Motion Control of Marine Vehicles 19
- 3.1 Guidance Systems . . . 19
  - 3.1.1 Path Following . . . 19
- 3.2 Navigation systems . . . 21
  - 3.2.1 State estimation . . . 21
  - 3.2.2 Sensors . . . 21
- 3.3 Control Systems . . . 23
  - 3.3.1 PID Control . . . 23
  - 3.3.2 Feedback Linearization . . . 23
  - 3.3.3 Optimal Control Theory . . . 23
  - 3.3.4 Sliding Mode Control . . . 24
  - 3.3.5 Adaptive Control . . . 24
  - 3.3.6 Control Allocation . . . 24

4 Literature Review 25

4.1 Sea State at Aquaculture Sites . . . 25
4.2 Bathymetric SLAM and Altitude Estimation . . . 26
4.3 Path Following . . . 27
    4.3.1 Integral Line-Of-Sight Guidance . . . 27
    4.3.2 Path Following for Curved Paths . . . 28
    4.3.3 Line-Of-Sight Guidance for Fully-Actuated Vehicles . . . 29
4.4 Higher-Order Sliding Mode Control . . . 29
4.5 Differential games and mixed H_2/H_∞ control . . . 31
4.6 Learning Model Predictive Control For Iterative Tasks . . . 31

III Method **33**

5 Overview and Control Objective **35**
5.1 Objectives for Net Pen Approximation . . . 35
5.2 Objectives for Motion Control . . . 36
5.3 Outline . . . 36

6 Net Pen Geometry Approximation from DVL Measurements **39**
6.1 DVL Beams Representation . . . 39
6.2 Net Pen Approximation . . . 39
6.3 Calculation of the Desired Heading . . . 40
6.4 ROV Distance Relative to the Approximated Net Pen . . . 41
6.5 Prediction of Approaching Corners . . . 42
6.6 An Alternative Approach: Generating a Desired Curved Path Relative to the Net Pen . . . 43
    6.6.1 Past, Present and Future Plane Approximations . . . 43
    6.6.2 Waypoint Generation . . . 43
    6.6.3 Curve Generation From Waypoints . . . 44
    6.6.4 Net Normal Angle and Crosstrack Error . . . 44

7 Guidance System **45**
7.1 Guidance Law . . . 45
7.2 Crosstrack Error with Feedforward . . . 48
7.3 Tracking Supervisor and Speed Reduction . . . 48

8 Control System **51**
8.1 PID Controllers . . . 51
8.2 First-order Sliding Mode Controllers . . . 52
    8.2.1 Stability Analysis . . . 53
8.3 Super-Twisting Algorithm with Adaptive Gains . . . 55

IV Results **57**

9 ROV Model and Simulation Setup **59**
9.1 ROV Model . . . 59
    9.1.1 Sensors . . . 61
    9.1.2 Thrusters . . . 61
9.2 Environmental Disturbances . . . 62
9.3 FhSim . . . 62

9.3.1 GUI and Visualization 64

10 Simulation Results **65**
10.1 Net Approximation 65
10.2 Guidance Law 66
10.2.1 Path Following 66
10.2.2 Speed Reduction Function 67
10.3 Control Laws 71
10.3.1 PID Control 71
10.3.2 1st Order Sliding Mode Control 71
10.3.3 Adaptive Super-Twisting Algorithm 72
10.3.4 Final Remarks on Tuning 73
10.4 Net Following 80

11 Experimental Results **83**
11.1 Basin Tests 83
11.2 Full-scale Test at SINTEF ACE Aquaculture Laboratory 85

V Discussion **93**

12 Discussion **95**
12.1 Performance of the Net Pen Geometry Approximation 95
12.2 DVL Measurements 97
12.3 Performance of the Guidance Law 98
12.4 Performance of the Proposed Control Laws 99
12.5 Robustness to Environmental Loads 100

13 Conclusions **103**
13.1 Future Work 104

Appendices **107**

A Proof of Theorem 2 **109**

B Paper to be Submitted to IEEE Journal of Oceanic Engineering **115**

Bibliography **127**

List of Figures

1.1 Illustration of the Artifex concept (A.M. Lien, SINTEF Ocean AS) . . . 4

2.1 Illustration of the body-fixed coordinate frame. 10
2.2 The geometrical relationship between the course angle χ, the heading angle ψ and the crab angle β. Picture from [24]. 15

3.1 A typical structure of a GNC system. 19
3.2 Graphical representation of the LOS guidance law. Picture from [24]. The notation of the crosstrack error e relates to the notation y_e used in this thesis. 20
3.3 DVL system pointing towards the seabed. Picture from [53]. 22

4.1 The integral line of sight guidance law. At steady state, a nonzero crab angle ψ_{ss} allows an underactuated vehicle counteract the currents. Picture taken from [12]. 27
4.2 The LOS guidance geometry for curved paths. Picture is taken from [26]. 29

5.1 Overview of the guidance, navigation and control system. 35
5.2 ROV with a DVL traversing a net pen. 36
5.3 ROV position relative to the net pen, where $\boldsymbol{p}_{b/\text{net}}$ is the vector from the CO to the nearest point on the net pen, $\boldsymbol{p}_{\text{projection}}$ its projection onto the north-east plane and ψ^* is the angle from x^n to $\boldsymbol{p}_{\text{projection}}$. 37

6.1 The DVL beam vector components. 40
6.2 Relationship between $\boldsymbol{n}^n, \boldsymbol{n}^n_{\text{projection}}$ and ψ_d. 41
6.3 Traditional circular fish cage. Picture from [43]. 42

7.1 Geometric interpretation of the LOS guidance law with feed forward from approximated future plane. 48
7.2 Signal flow with speed reduction function. 49

8.1 Block diagram of 1st order sliding mode controllers. 52

9.1 Argus Mini (courtesy of Argus Remote Systems AS). 60
9.2 Thruster configuration of Argus Mini. 62
9.3 Applied force of a single thruster as a function of the normalized commanded input. Fitted to a quadratic model. 63
9.4 Overview of FhSim architecture. 63
9.5 Visualization of ROV traversing a net pen in FhSim. 64
9.6 Xbox Controller with mapping of buttons 64

10.1 Net pen geometry approximation 66
10.2 Straight line path following without environmental disturbances 68

10.3 Straight line path following with constant, irrotational current 68
10.4 Straight line path following with constant, irrotational current and waves. 69
10.5 Curved line path following with constant, irrotational current. 69
10.6 Net following with speed reduction. 70
10.7 Step response of PID controllers. 73
10.8 Thruster forces and moments during step response with PID control. . . 74
10.9 Response of PID controllers with sinusoidal reference signal 74
10.10 Step response with 1st order SMC. 75
10.11 Thruster forces and moments during step response with 1st order SMC. 75
10.12 Response of 1st order SMC with sinusoidal reference signal. 76
10.13 Sliding variables in 1st order SMC with step in reference. Notice the steady-state error in surge/sway. 76
10.14 1st order sliding mode depth control with modeling error. 77
10.15 Step response with adaptive STA. 77
10.16 Thruster forces and moments during step response with adaptive STA. . 78
10.17 Adaptive gain during adaptive STA with step in reference. 78
10.18 Response of adaptive STA with sinusoidal reference signals. 79
10.19 Adaptive STA heading control pulse response. 79
10.20 Net following without environmental disturbances. 81
10.21 Net following with environmental disturbances. 82

11.1 ROV with DVL attached. 84
11.2 Shape of water basin. Horizontal projection. 84
11.3 Basin wall following using DVL. 88
11.4 Net pen Following at SINTEF ACE Rataran 31th Oct. 2019. ”Loss” marks loss of DVL pings, ”jump” marks jump in DVL measured distance. 89
11.5 Net pen following at SINTEF ACE Rataran 31th Oct. 2019 with integral gain $\sigma = 0.05$. 90
11.6 Net pen following at SINTEF ACE Rataran 14th Nov. 2019. 91

12.1 Net pen geometry approximation from DVL beams. 96

13.1 Images from ROV front camera during net pen following. 105

List of Tables

2.1.1 The states, forces and moments of a 6 DOF vessel 9

10.3.1 Control law design parameters. 71

11.1.1 Parameters and references during basing trial. 85
11.2.1 Parameters and references during SINTEF ACE trials. 86

List of Abbreviations

(I)LOS	(Integral) Line-of-sight
AUV	Autonomously underwater vehicle
CB/CG/CO	Center of buoyancy/gravity/origin
DOF	Degree-of-freedom
DVL	Doppler velocity log
EOM	Equations of motion
GNC	Guidance, navigation and control
GNSS	Global navigation satellite system
MPC	Model predicative control
NED	North-east-down
ROV	Remotely operated vehicle
SMC	Sliding mode control
STA	Super-twisting algorithm
UGAS/UGES/ULES	Uniformly globally/locally asymptotically/exponentially stable
USBL	Ultra-short baseline
USGES	Uniformly semi-globally exponentially stable

Part I

Introduction

Chapter 1

Introduction

This master thesis explores methods of automating remotely operated vehicle (ROV) inspections of aquaculture net pens. As net pens are dynamic structures, the shape of net pens will be time-varying in the presence of environmental loads such as ocean currents and waves. This can be problematic for guidance systems based upon geo-referenced positions, as they yield no information of the position of the ROV relative to the unknown net pen position and shape. In response to this, the thesis explores how a Doppler velocity log (DVL) system can be used as a mean for navigation of the ROV by computing the ROV position relative to the net pen. Finally, the thesis also concerns the design of guidance and control systems, with the aim of making the ROV autonomously transverse the net, as well as being robust to environmental disturbances.

1.1 Motivation

With a steadily increasing global population of more than 7 billion people, producing enough food is a major challenge. Furthermore, land-based agriculture often yield a big carbon footprint. With the majority of earth's surface being covered by oceans, marine food production will be essential in terms of meeting global food demands while simultaneously decreasing carbon emissions. Aquaculture is the fastest growing food production industry in the world, and by 2030 the World Bank projects that 62% of all seafood consumed will be raised in fish farms [3].

The ocean has historically been of great importance for Norway and the Norwegian economy, with a vast coastal line and a continental shelf four times the size of the Norwegian mainland. The Norwegian aquaculture industry has been experiencing a rapid growth since the 1970s, and in 2017 there were a total of 1070 registered sites for salmon fish farming along the Norwegian coast [37] and the aquaculture industry had a revenue of 62 billion NOK [51]. However, the aquaculture industry faces several challenges, such as fish welfare, HSE and fish escapes. In 2010, it was reported that more than two thirds of the registered fish escape incidents in the Norwegian aquaculture industry stems from holes in the net [30]. Escapes from fish farms are a threat to the wild fish population, for example from transfer of diseases or alteration of wild fish genetics through interbreeding. Inspection, maintenance and repair operations of net pens are important countermeasures against this threat.

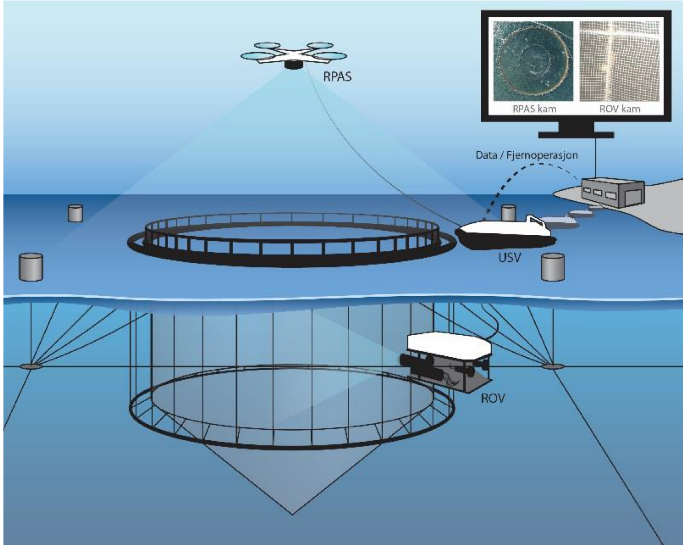

Figure 1.1: Illustration of the Artifex concept (A.M. Lien, SINTEF Ocean AS)

Traditionally, Norwegian aquacultural sites have utilized professional divers for inspection and repairs of net pens. However, diving operations are particularly exposed to risk. In a recent pole for the Norwegian labor union Industri Energi[21], 57% of Norwegian inshore divers stated that they have experienced a work-related fear of death or severe injuries. This is a key motivation for replacing the divers with ROVs, a trend that has been increasing for the last decade. Typically, the pilot steers the ROV based upon information from a forward-looking camera and sensors such as compass and depth sensors. Due to water flow turbidity, lighting conditions and surrounding biomass, piloting of ROVs are challenging, and full coverage of the net cannot be expected. To enable safe and reliable inspections of net pens, new control methods are required. Furthermore, there is an ongoing effort towards developing new methods in aquaculture robotics that can enable remote or autonomous operations [23], which will both increase safety and reduce operational costs..

Another trend in recent years is that fish farms tend to relocate to locations more exposed to environmental loads such as winds, waves and currents. These locations have a greater water flow, which is beneficial in terms of waste dispersal and water quality. However, more exposed locations poses new challenges to the fish farming industry, due to the severity and irregularity of the environmental loads. For marine motion control, one often assume that environmental loads are constant or slowly varying in space and time. This assumption may not hold for aquaculture at exposed sites, and more robust control systems may be needed.

As part of the ongoing development in autonomy in the fish farming industry, SINTEF Ocean is developing a project for future remote operations at fish farms called Artifex. The main objective of the Artifex project is to develop robots for remote autonomous inspection, maintenance and repair operations at fish farming sites. In particular, an Unmanned Surface Vehicle (USV) is used as a platform for carrying a Remotely Operated Vehicle (ROV) for underwater operations, and a Remotely Piloted Aircraft Systems (RPAS) for airborne inspection tasks, see Fig. 1.1. Project partners for the Artifex project are Maritime Robotics AS, Argus Remote Systems AS, Lerow AS, NTNU and WavEC. This thesis is concerned with motion control of the ROV.

The thesis problem relate to several interesting scientific challenges. While navigation of marine surface vessels is an area largely explored, underwater navigation still faces big challenges. A key reason is that global navigation satellite system (GNSS) signals, such as GPS signals, don't penetrate the water surface, thus proving inefficient underwater. Other methods for estimating the position of underwater vehicles therefore has to be considered. DVL is one instrument that is often being used for underwater navigation. The primary use of DVL has historically been to derive the velocity over ground of the vehicle. In [19], however, a method for using DVL to approximate the vehicle altitude was presented. This method is the inspiration for the thesis, which further explores the possibility of using DVL as a tool for positioning and attitude measurement relative to a dynamic net pen.

Path following is another concern of this thesis, which is a fundamental part of autonomous marine operations. The line-of-sight (LOS) method is an intuitive method, with proven stability [13]. For the case of underactuated vehicles, the method is based upon minimizing the vehicle distance to the desired path by controlling the vehicle heading. This thesis explores how the LOS guidance law can be utilized by a fully-actuated vehicle, which is able to minimize the crosstrack error while still maintaining a fixed heading.

Finally, the thesis investigates the performance of different control structures for controlling the position and motion of marine vehicles with the aim of increasing robustness to environmental loads. More precisely, a 1st order sliding mode control (SMC) law and 2nd order sliding mode control law called super-twisting algorithm (STA) is suggested, and their performance is compared to that of traditional PID control.

1.2 Outline

This thesis is written in 6 parts and 14 chapters. A short description is given below:

- Part 2 presents the background theory necessary for this thesis, as well as the literature review. It is assumed that the reader is familiar with dynamic systems and control theory.
  - Chapter 2 presents the basic background theory to marine craft dynamics. The chapter also presents the notation used in the thesis.
  - Chapter 3 presents some principles to guidance, navigation and motion control of marine vehicles.
  - Chapter 4 presents the literature review done in relation to this thesis.
- Part 4 describes the method used in the thesis.
  - Chapter 5 presents the control objectives.
  - Chapter 6 proposes a method for net pen geometry approximation.
  - Chapter 7 proposes a guidance system of the ROV.
  - Chapter 8 proposes the control system of the ROV.
- Part 5 describes the simulations and experiments done for the thesis, as well as presenting and discussing the results.
  - Chapter 9 presents the model of the ROV, as well as tools used in simulation and control design.

  - Chapter 10 presents results from simulation and experiments.

- In Part 6, the results and findings from the thesis are discussed. The chapter also proposes further work to be done.

- Appendix B includes a draft to a paper which is to be submitted to IEEE Journal of Oceanic Engineering.

Part II

Theory

Chapter 2

Marine Craft Dynamics

This chapter present the basics of marine craft dynamics. The notations and equations are represented using Fossens Robotics-like vectorial model [24]. This is an efficient way of describing 6 DOF differential equations with coupling effects in matrix form, inspired by the classic robotic model

$$\boldsymbol{M}(\boldsymbol{q},\dot{\boldsymbol{q}})\dot{\boldsymbol{q}} + \boldsymbol{C}(\boldsymbol{q})\boldsymbol{q} = \boldsymbol{\tau} \tag{2.1}$$

2.1 Notation

The different states and forces of a 6 DOF marine craft are defined as in SNAME [45], and are given by Table 2.1.1.

DOF		Positions & Euler angles	Linear & angular velocities	Forces & moments
1	Surge	x	u	X
2	Sway	y	v	Y
3	Heave	z	w	Z
4	Roll	ϕ	p	K
5	Pitch	θ	q	M
6	Yaw	ψ	r	N

Table 2.1.1: The states, forces and moments of a 6 DOF vessel

2.2 Reference Frames

When considering motion of marine crafts, it is convenient to define several reference frames. For operations over vast areas, eg. aviation or marine vessels traveling over large distances, it is typical to use earth-centered reference frames. However, this thesis only considers operations over small areas, and therefore uses reference frames as defined below.

NED: The North-East-Down (NED) coordinate system $\{n\} = (x_n, y_n, z_n)$ is obtained by defining a tangential plane relative to the Earth's surface. Its x axis points towards the true north, y_n points east, while z_n points downwards normal to the tangential plane. For marine crafts operating in a local area, $\{n\}$ can be considered to be inertial.

BODY: The body-fixed reference frame $\{b\} = (x_b, y_b, z_b)$ is a moving coordinate system that has its origin o_b attached to the object of interest. For this thesis, x_b is defined to be from aft to fore, y_b towards starboard, while z_b from top to bottom. The center of origin o_b will be referred to as the CO. The CO can be placed at any point of the vehicle, and is usually decided to simplify the EOM of the vehicle or based on the sensor locations. Figure 2.1 provides an illustration of the body-fixed coordinate frame.

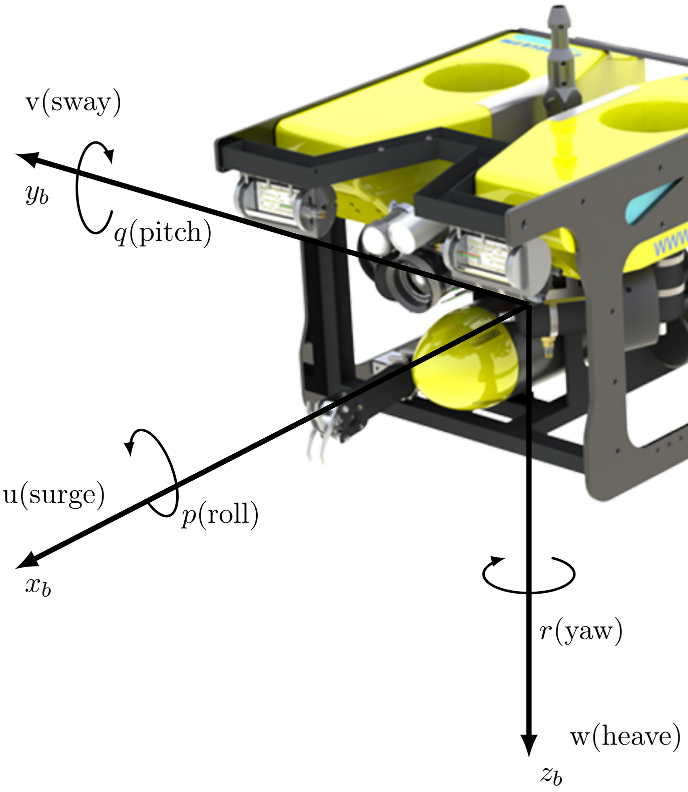

Figure 2.1: Illustration of the body-fixed coordinate frame.

2.3 Vectorial Notation

Throughout this thesis, the position, orientation and motion of a vehicle is given as vectors and generalized coordinates. Vectors and matrices are **bold**, and sub- and superscript is defined as the following:

$\mathbf{v}^e_{b/n}$ = linear velocity of the point o_b with respect to {n} expressed in {e}

$\mathbf{\Theta}_{nb}$ = Euler angles between {n} and {b}

2.3.1 Generalized Coordinates

The linear and angular position and velocity vectors are given by

$$\mathbf{p}^n_{b/n} \triangleq \begin{bmatrix} x_n \\ y_n \\ z_n \end{bmatrix}, \qquad \boldsymbol{\Theta}_{nb} \triangleq \begin{bmatrix} \phi \\ \theta \\ \psi \end{bmatrix}, \tag{2.2}$$

$$\mathbf{v}^b_{b/n} \triangleq \begin{bmatrix} u \\ v \\ w \end{bmatrix}, \qquad \boldsymbol{\omega}^b_{b/n} \triangleq \begin{bmatrix} p \\ q \\ r \end{bmatrix} \tag{2.3}$$

where $\mathbf{p}^n_{b/n} \in \mathbb{R}^3$ is the linear position, $\boldsymbol{\Theta}_{nb} \in \mathbb{R}^3$ are the Euler angles, $\mathbf{v}^b_{b/n} \in \mathbb{R}^3$ is the linear velocity and $\boldsymbol{\omega}^b_{b/n} \in \mathbb{R}^3$ is the angular velocity.

The generalized position and velocity vectors are given by

$$\boldsymbol{\eta} = \begin{bmatrix} (\boldsymbol{p}^n_{b/n})^T & (\boldsymbol{\Theta}_{nb})^T \end{bmatrix}^T \qquad \boldsymbol{\nu} = \begin{bmatrix} (\boldsymbol{v}^b_{b/n})^T & (\boldsymbol{\omega}^b_{b/n})^T \end{bmatrix}^T \tag{2.4}$$

respectively.

The force and moments vector is given by

$$\boldsymbol{\tau} = \begin{bmatrix} X & Y & Z & K & M & N \end{bmatrix} \tag{2.5}$$

2.4 Kinematics

The 6 DOF kinematic EOM can be expressed as

$$\begin{gathered} \dot{\boldsymbol{\eta}} = \mathbf{J}_\Theta(\boldsymbol{\Theta})\boldsymbol{\nu} \\ \Updownarrow \\ \begin{bmatrix} \dot{\mathbf{p}}^n_{b/n} \\ \dot{\boldsymbol{\Theta}}_{nb} \end{bmatrix} = \begin{bmatrix} \mathbf{R}^n_b(\boldsymbol{\Theta}_{nb}) & \mathbf{0}_{3x3} \\ \mathbf{0}_{3x3} & \mathbf{T}_\Theta(\boldsymbol{\Theta}_{nb}) \end{bmatrix} \begin{bmatrix} \boldsymbol{\nu}^b_{b/n} \\ \boldsymbol{\omega}^b_{b/n} \end{bmatrix} \end{gathered} \tag{2.6}$$

where

$$\mathbf{R}^n_b(\boldsymbol{\Theta}_{nb}) \triangleq \begin{bmatrix} c\psi & -s\psi c\phi + c\psi s\theta s\phi & s\psi s\phi + c\psi c\phi s\theta \\ s\psi c\phi & c\psi c\phi + s\phi s\theta s\psi & -c\psi s\phi + s\theta s\psi c\phi \\ -s\theta & c\theta s\phi & c\theta c\phi \end{bmatrix} \tag{2.7}$$

$$\mathbf{T}_\Theta(\boldsymbol{\Theta}_{nb}) \triangleq \begin{bmatrix} 1 & s\phi t\theta & c\phi t\theta \\ 0 & c\phi & -s\phi \\ 0 & s\phi/c\theta & c\phi/c\theta \end{bmatrix} \tag{2.8}$$

and $s\cdot = \sin(\cdot)$, $c\cdot = \cos(\cdot)$, $t\cdot = \tan(\cdot)$.

Remark 1. *Notice that (2.8) suffers a singularity when $\theta = \pm 90°$. To overcome this problem, an alternative is to describe the kinematics in quaternions, which is a non-minimal attitude representation, see for instance [1, 20, 24].*

2.4.1 Kinematic Subsystems

In many cases, it might be a possible to neglect in motion in certain DOFs and defining subsystems of (2.6). Most ROVs are designed to be stable in roll and pitch, one can therefore assume that ϕ, θ are small and can be neglected. The kinematic equations can therefore be expressed by

$$\dot{\boldsymbol{\eta}} = \mathbf{J}_{\psi}(\psi)\boldsymbol{\nu} \tag{2.9}$$

where $\boldsymbol{\eta} = [x, y, z, \psi]^T, \boldsymbol{\nu} = [u, v, w, r]^T$, and

$$\mathbf{J}_{\psi}(\psi) \triangleq \begin{bmatrix} c\psi & -s\psi & 0 & 0 \\ s\psi & c\psi & 0 & 0 \\ 0 & 0 & 1 & 0 \\ 0 & 0 & 0 & 1 \end{bmatrix} \tag{2.10}$$

For surface vessels or ROVs stable in heave (for instance by the use of a depth controller), the equations can further be simplified to

$$\dot{\boldsymbol{\eta}} = \mathbf{R}(\psi)\boldsymbol{\nu} \tag{2.11}$$

where $\boldsymbol{\eta} = [x, y, \psi]^T, \boldsymbol{\nu} = [u, v, r]^T$, and

$$\mathbf{R}(\psi) \triangleq \mathbf{R}_{z,\psi} = \begin{bmatrix} c\psi & -s\psi & 0 \\ s\psi & c\psi & 0 \\ 0 & 0 & 1 \end{bmatrix} \tag{2.12}$$

is the principal rotation matrix around the z axis.

2.5 Kinetics

According to [24], the general 6 DOF kinetic EOM for marine vehicles is given by

$$\mathbf{M}\dot{\boldsymbol{\nu}} + \mathbf{C}(\boldsymbol{\nu})\boldsymbol{\nu} + \mathbf{D}(\boldsymbol{\nu})\boldsymbol{\nu} + \mathbf{g}(\boldsymbol{\eta}) = \boldsymbol{\tau}_c + \mathbf{w} \tag{2.13}$$

where
$\mathbf{M} = \mathbf{M}_{RB} + \mathbf{M}_A$ is the mass matrix including the rigid body and added mass terms
$\mathbf{C}(\boldsymbol{\nu}) = \mathbf{C}_{RB}(\boldsymbol{\nu}) + \mathbf{C}_A(\boldsymbol{\nu})$ is the centripetal-Coriolis matrix including rigid body and added mass terms
$\mathbf{D}(\boldsymbol{\nu})$ is the damping matrix
$\mathbf{g}(\boldsymbol{\eta})$ is a vector of gravitational/buoyancy forces and moments
$\boldsymbol{\tau}_c = [\tau_u, \tau_v, \tau_w, \tau_p, \tau_q, \tau_r]^T$ is a vector of control inputs
$\mathbf{w}$ is a vector of environmental disturbances and modelling errors

Considering (2.13), the following properties hold [1, 24] for a rigid body moving through an ideal fluid:

- $\mathbf{M}_{RB} = \mathbf{M}_{RB}^T > 0$
- $\dot{\mathbf{M}}_{RB} = 0$
- $\mathbf{D}(\boldsymbol{\nu}) > 0$
- $\mathbf{C}(\boldsymbol{\nu}) = -\mathbf{C}^T(\boldsymbol{\nu})$

Let

$$\mathbf{M} = \begin{bmatrix} \mathbf{M}_{11} & \mathbf{M}_{12} \\ \mathbf{M}_{21} & \mathbf{M}_{22} \end{bmatrix} \tag{2.14}$$

where $\boldsymbol{M}_{ij} \in \mathbb{R}^3$. Define furthermore $\boldsymbol{\nu}_1 \triangleq \mathbf{v}^b_{b/n}$ and $\boldsymbol{\nu}_2 \triangleq \boldsymbol{\omega}^b_{b/n}$. Then the centripetal-Coriolis matrix can always be parameterized by [24]

$$\mathbf{C}(\boldsymbol{\nu}) = \begin{bmatrix} \mathbf{0}_{3x3} & -\mathbf{S}(\mathbf{M}_{11}\boldsymbol{\nu}_1 + \mathbf{M}_{12}\boldsymbol{\nu}_2) \\ -\mathbf{S}(\mathbf{M}_{11}\boldsymbol{\nu}_1 + \mathbf{M}_{12}\boldsymbol{\nu}_2) & -\mathbf{S}(\mathbf{M}_{21}\boldsymbol{\nu}_1 + \mathbf{M}_{22}\boldsymbol{\nu}_2) \end{bmatrix} \tag{2.15}$$

where $\mathbf{S}$ is the cross-product operator. The term $\boldsymbol{C}(\boldsymbol{\nu})\boldsymbol{\nu}$ includes the so-called Munk-moments, which is known to have a destabilizing effect.

2.5.1 Hydrodynamics

Added mass:
Added mass refers to the additional inertia of surrounding fluid that is accelerated when a body is moving in a fluid. The added mass matrix is given by

$$\mathbf{M}_A = - \begin{bmatrix} X_{\dot{u}} & X_{\dot{v}} & X_{\dot{w}} & X_{\dot{p}} & X_{\dot{q}} & X_{\dot{r}} \\ Y_{\dot{u}} & Y_{\dot{v}} & Y_{\dot{w}} & Y_{\dot{p}} & Y_{\dot{q}} & Y_{\dot{r}} \\ Z_{\dot{u}} & Z_{\dot{v}} & Z_{\dot{w}} & Z_{\dot{p}} & Z_{\dot{q}} & Z_{\dot{r}} \\ K_{\dot{u}} & K_{\dot{v}} & K_{\dot{w}} & K_{\dot{p}} & K_{\dot{q}} & K_{\dot{r}} \\ M_{\dot{u}} & M_{\dot{v}} & M_{\dot{w}} & M_{\dot{p}} & M_{\dot{q}} & M_{\dot{r}} \\ N_{\dot{u}} & N_{\dot{v}} & N_{\dot{w}} & N_{\dot{p}} & N_{\dot{q}} & N_{\dot{r}} \end{bmatrix}, \tag{2.16}$$

where for instance $X_{\dot{u}} = \partial X / \partial \dot{u}$.

In general, there are no specific properties for $\boldsymbol{M}_A$ [1]. However, for a body completely submerged in fluid, it can be considered $\boldsymbol{M}_A > 0$. Furthermore, for a submerged body with low velocity and three planes of symmetry, which is common for underwater vehicles, the added mass can be approximated as

$$\mathbf{M}_A = -\text{diag}\{X_{\dot{u}}(0), Y_{\dot{v}}(0), Z_{\dot{w}}(0), K_{\dot{p}}(\omega_{\text{roll}}), M_{\dot{q}}(\omega_{\text{pitch}}), N_{\dot{r}}(0)\} \tag{2.17}$$

where $\omega_{\text{roll}}, \omega_{\text{pitch}}$ are the natural frequency in roll and pitch respectively [18].

Damping terms:
For underwater vehicles, potential damping and other wave related damping effects can be neglected. The damping is then dominated by skin friction and vortex shredding. The damping can be approximated by

$$\boldsymbol{D}(\boldsymbol{\nu}) = \boldsymbol{D} + \boldsymbol{D}_n(\boldsymbol{\nu}), \tag{2.18}$$

where the linear terms stems from skin friction, and the nonlinear term are quadratic damping from vortex shredding. For low speed operations, $\boldsymbol{D}$ will dominate $\boldsymbol{D}_n(\boldsymbol{\nu})$, vice versa for high speed operations.

Typically, the elements of $\boldsymbol{D}$ and $\boldsymbol{D}_n(\boldsymbol{\nu})$ can be calculated by hydrodynamics programs by using strip theory. This theory assumes slender body types, and therefore cannot be considered valid for ROVs. A possibility is to approximate the ROV as a box and calculate the damping terms analytically from this. However, this theory will typically lead to underestimations, because of the many cavities and appendages of the ROV body [18].

Due to this difficulty in finding damping terms, and because the diagonal terms are dominant, the damping matrices are often approximated by

$$\begin{aligned} \mathbf{D} &= -\operatorname{diag}\{X_u, Y_v, Z_w, K_p, M_q, N_r\} \\ \mathbf{D}_n(\boldsymbol{\nu}) &= -\operatorname{diag}\{X_{|u|u}|u|, Y_{|v|v}|v|, Z_{|w|w}|w|, K_{|p|p}|p|, M_{|q|q}|q|, N_{|r|r}|r|\} \end{aligned} \tag{2.19}$$

where the diagonal elements are negative constants.

2.5.2 Restoring Forces

Define the vehicle weight W and buoyancy B

$$W \triangleq mg, \qquad B \triangleq \rho g \nabla, \tag{2.20}$$

where m is the mass, ρ the water density, g the gravity acceleration and ∇ the displacement of water. Most ROVs are designed to be slightly positively buoyant, ie. $B > W$, such that in the case of a system shut down the ROV will slowly rise to the surface.

Furthermore, define the vector $\boldsymbol{r}_g^b$ from the center of gravity (CG) to the CO:

$$\boldsymbol{r}_g^b = \begin{bmatrix} x_g \\ y_g \\ z_g \end{bmatrix} \tag{2.21}$$

and similarly the vector $\boldsymbol{r}_b^b$ from the center of buoyancy (CB) to the CO:

$$\boldsymbol{r}_b^b = \begin{bmatrix} x_b \\ y_b \\ z_b \end{bmatrix} \tag{2.22}$$

The restoring forces from gravity and buoyancy can then be described by the vector

$$\boldsymbol{g}(\boldsymbol{\eta}) = \begin{bmatrix} (W-B)\sin(\theta) & & \\ -(W-B)\cos(\theta)\sin(\phi) & & \\ -(W-B)\cos(\theta)\cos(\phi) & & \\ -(y_gW - y_bB)\cos(\theta)\cos(\phi) & + & (z_gW - z_bB)\cos(\theta)\sin(\phi) \\ (z_gW - z_bB)\sin(\theta) & + & (x_gW - x_bB)\cos(\theta)\cos(\phi) \\ -(x_gW - x_bB)\cos(\theta)\sin(\phi) & - & (y_gW - y_bB)\sin(\theta) \end{bmatrix} \tag{2.23}$$

2.6 Course, Heading and Crab Angle

This section will present the concepts of course, heading and crab angle, which are important when considering maneuvering of marine vessels.

Definition 1. **(Course angle χ)**
The angle from x_n to the velocity vector of the vehicle, positive rotation about z_n.

Definition 2. (**Heading (yaw) angle ψ**)
The angle from x_n to x_b, positive rotation about z_n.

Definition 3. (**Crab (sideslip) angle β**)
The angle from x_b to the velocity vector of the vehicle, positive rotation about z_n.

Furthermore, these definitions satisfies $\chi = \psi + \beta$, see figure 2.2. The crab angle can be calculated as $\beta = \sin^{-1}(v/U)$ where $U = \sqrt{u^2 + v^2}$ is the speed of the vehicle, alternatively as $\beta = \tan^{-1}(v/u)$.

Remark 2. *This thesis follows the definition of β according to [24]. In SNAME [45], the sign is opposite, that is $\beta_{\text{SNAME}} = -\beta$.*

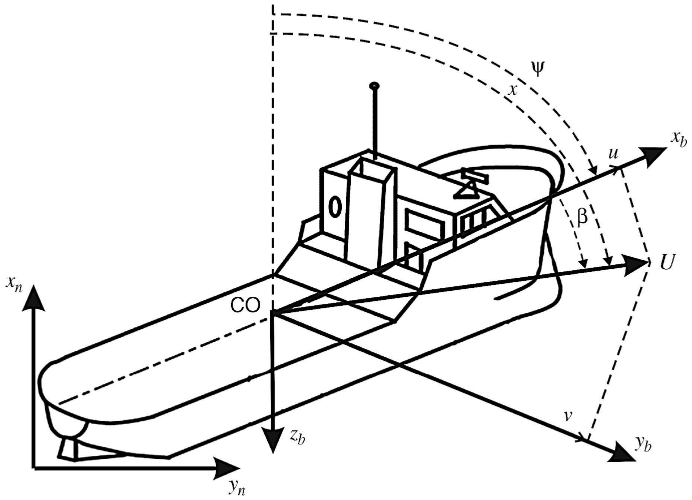

Figure 2.2: The geometrical relationship between the course angle χ, the heading angle ψ and the crab angle β. Picture from [24].

2.7 Environmental Forces and Moments

This section presents the basic behind currents, and wave forces, two major environmental disturbances. In most ROV operations, wave forces can be neglected, as they are surface phenomenons. However, for operations in shallow water, they need to be considered as well. As ROVs mostly are completely submerged, wind forces are neglected in this thesis.

2.7.1 Wave-induced Forces and Moments

Waves are mainly generated by wind, but other forces such as tidal forces and the Earths rotation generates waves as well. Waves can be divided into two categories: wind waves generated by local wind and swell waves that are generated far off at sea.

The wave-induced forces can be separated into two effects:

- **First-order wave-induced forces:** wave-frequency (WF) motion observed as zero-mean oscillatory motions, denoted $\boldsymbol{\tau}_{\text{wave1}}$

- **Second-order wave-induced forces:** wave drift forces observed as nonzero slowly varying components, denoted $\boldsymbol{\tau}_{\text{wave2}}$

While a control system should compensate for the effect of second-order wave-induced forces, according to [24] the control system should not compensate for the first-order wave-induced forces. These effects are outside of the bandwith of the controllers, and should be filtered away from the measurements fed back to the control system.

There exists different theories for how induced wave forces can be calculated. A common method is through Response Amplitude Operators (RAOs) [24, 60]. Typically, a marine ship RAOs can be calculated by hydrodynamic programs from the ship hull. The induced wave forces can be calculated from the wave amplitude and the RAOs. An alternative method is to use state-space models where the RAOs and vehicle dynamics in a cascade is modeled through constant, tunable gains. Typically, this is not as accurate, but as this method does not require a priori known vehicle geometry, it can be a good approach for design and testing of control systems.

The zone where waves are effective is typically down to depths at about half of the wave lengths. Furthermore, the wave loads decreases exponentially with depth [22].

2.7.2 Ocean Currents

Define the relative velocity $\boldsymbol{\nu}_r := \boldsymbol{\nu} - \boldsymbol{\nu}_c$, where $\boldsymbol{\nu}_c \in \mathbb{R}^6$ is the velocity of the current expressed in $\{b\}$. Then the equations of motions can be extended to

$$\mathbf{M}_{RB}\dot{\boldsymbol{\nu}} + \mathbf{C}_{RB}(\boldsymbol{\nu})\boldsymbol{\nu} + \mathbf{g}(\boldsymbol{\eta}) + \mathbf{M}_A\dot{\boldsymbol{\nu}}_r + \mathbf{C}_A(\boldsymbol{\nu}_r)\boldsymbol{\nu}_r + \mathbf{D}(\boldsymbol{\nu}_r)\boldsymbol{\nu}_r = \boldsymbol{\tau}_c + \boldsymbol{\tau}_{\text{wave,1}} + \boldsymbol{\tau}_{\text{wave,2}} \quad (2.24)$$

In most control applications, the current is considered constant and irrotational in $\{n\}$. For many cases, this is a good approximation and simplifies the equations of motions considerably. The generalized ocean current velocity is then given by

$$\boldsymbol{\nu}_c = [u_c, v_c, w_c, 0, 0, 0]^T \quad (2.25)$$

Furthermore, $\dot{\boldsymbol{V}}_c = 0$, where $\boldsymbol{V}_c := \text{blockdiag}\{\boldsymbol{R}_b^n(\boldsymbol{\Theta}_{nb}), \mathbf{0}\}\boldsymbol{\nu}_c = \left[V_x, V_y, V_z, 0, 0, 0\right]^T$ is the current velocity in $\{n\}$. The dynamic model can then be expressed by

$$\dot{\boldsymbol{\eta}} = \mathbf{J}_\Theta(\boldsymbol{\eta})\boldsymbol{\nu}_r + \mathbf{V}_c \quad (2.26)$$

$$\mathbf{M}\dot{\boldsymbol{\nu}}_r + \mathbf{C}(\boldsymbol{\nu}_r)\boldsymbol{\nu}_r + \mathbf{D}(\boldsymbol{\nu}_r)\boldsymbol{\nu}_r + \mathbf{g}(\boldsymbol{\eta}) = \boldsymbol{\tau}_c + \boldsymbol{\tau}_{\text{wave,1}} + \boldsymbol{\tau}_{\text{wave,2}} \quad (2.27)$$

2.8 Actuation

A marine craft usually has several actuators, and it is necessary to distribute the generalizes control forces $\boldsymbol{\tau}_c$ to the different actuators. A rigid body is said to be fully actuated if it has actuators that can provide forces or moments in all DOFs, if not it is said to be underactuated.

Most marine surface vessels have its main propellers and rudder at the aft of the ship. Other actuators can include tunnel thrusters in the transverse direction, azimuth thrusters that can be rotated or control surfaces such as stabilizing fins. Since the aft propellers typically will dominate transverse or azimuth thrusters at high speed, surface vessels in transit are most often actuated only in surge and yaw, thus being underactuated. For ROVs with three planes of symmetry, it is common to arrange the thrusters in a configuration which makes the vehicle actuated in at least 4 DOFs (surge, sway, heave, yaw).

The generalized actuator forces and moments relate to the control forces and moments by

$$\boldsymbol{\tau}_c = \mathbf{T}(\boldsymbol{\alpha})\mathbf{f} \tag{2.28}$$

where $\boldsymbol{\alpha}$ is a vector of azimuth angles, $\mathbf{T}(\boldsymbol{\alpha})$ is a thrust configuration matrix and $\mathbf{f}$ is the control forces and moments. For nonrotatable thrusters, which is common for ROVs, (2.28) can be simplified as

$$\boldsymbol{\tau}_c = \mathbf{B}\mathbf{f}, \tag{2.29}$$

where $\mathbf{B}$ is a constant configuration matrix.

2.9 Summary

Gathering the results from previous sections, the complete kinetic and kinematic equations for ROVs to be used in control design can be written as

$$\begin{gathered}\dot{\boldsymbol{\eta}} = \mathbf{J}_\Theta(\boldsymbol{\eta})\boldsymbol{\nu}_r + \boldsymbol{V}_c \\ \mathbf{M}_{RB}\dot{\boldsymbol{\nu}} + \mathbf{C}_{RB}(\boldsymbol{\nu})\boldsymbol{\nu} + \mathbf{g}(\boldsymbol{\eta}) + \mathbf{M}_A\dot{\boldsymbol{\nu}}_r + \mathbf{C}_A(\boldsymbol{\nu}_r)\boldsymbol{\nu}_r + \mathbf{D}(\boldsymbol{\nu}_r)\boldsymbol{\nu}_r = \mathbf{B}\mathbf{f} + \boldsymbol{\tau}_{\text{wave},2}\end{gathered} \tag{2.30}$$

For operation below the wave effected zone and in constant, irrotational currents, the equations of motion can be simplified to

$$\begin{gathered}\dot{\boldsymbol{\eta}} = \mathbf{J}_\Theta(\boldsymbol{\Theta})\boldsymbol{\nu}_r + \boldsymbol{V}_c \\ \mathbf{M}\dot{\boldsymbol{\nu}}_r + \mathbf{C}(\boldsymbol{\nu}_r)\boldsymbol{\nu}_r + \mathbf{D}(\boldsymbol{\nu}_r)\boldsymbol{\nu}_r + \mathbf{g}(\boldsymbol{\eta}) = \mathbf{B}\mathbf{f}\end{gathered} \tag{2.31}$$

Chapter 3

Motion Control of Marine Vehicles

This chapter will present the basics of marine motion control system. A marine motion control system is usually constructed as three independent blocks denoted as *Guidance*, *Navigation* and *Control* (GNC) systems, interconnected as in Figure 3.1.

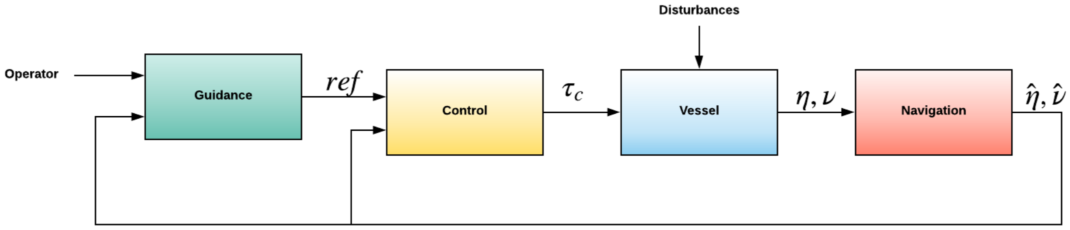

Figure 3.1: A typical structure of a GNC system.

3.1 Guidance Systems

A guidance system computes the reference position, velocity or acceleration vectors to be used as control inputs by the control system. The inputs to the guidance systems are usually the estimated states from the navigation system and instructions from the human operator. Typically, three scenarios for guidance is considered:

- Setpoint regulation
- Trajectory tracking
- Path following

This thesis considers path following, as the task is to traverse a net pen independent of time.

3.1.1 Path Following

Path following is an essential part for most applications in marine autonomy. Unlike trajectory tracking, path following is the objective of following a predefined path *independent* *of time.* As inputs, most path following schemes takes waypoints decided by the operator, and its output is a desired course angle which will guide the vehicle towards the next waypoint.

Line-Of-Sight Path Following

Line-of-sight (LOS) [25, 49] guidance is an intuitive and commonly used method for straight-line path following. The method imitates a helmsman steering the ship towards a point lying at a constant distance ahead of the vehicle on a predefined path.

The base of the method is to generate a set of straight lines between given waypoints. Consider a straight line between two waypoints $\mathbf{p}_k^n = [x_k, y_k]^T, \mathbf{p}_{k+1}^n = [x_{k+1}, y_{k+1}]^T$. As seen from Figure 3.2, the path has been rotated by an angle α_k relative to the x^n axis. The angle is frequently called the *path-tangential angle* and is given by

$$\alpha_k = \text{atan2}(y_{k+1} - y_k, x_{k+1} - x_k) \tag{3.1}$$

The coordinates of the vehicle in the path-fixed reference frame can be computed according to

$$\begin{bmatrix} s(t) \\ y_e(t) \end{bmatrix} = \begin{bmatrix} \cos(\alpha_k) & \sin(\alpha_k) \\ -\sin(\alpha_k) & \cos(\alpha_k) \end{bmatrix} (\mathbf{p}^n(t) - \mathbf{p}_k^n) \tag{3.2}$$

where $\mathbf{p}^n(t) = [x(t), y(t)]^T$ is the position of the vehicle in $\{n\}$, $s(t)$ is the along-track distance and $y_e(t)$ the crosstrack error.

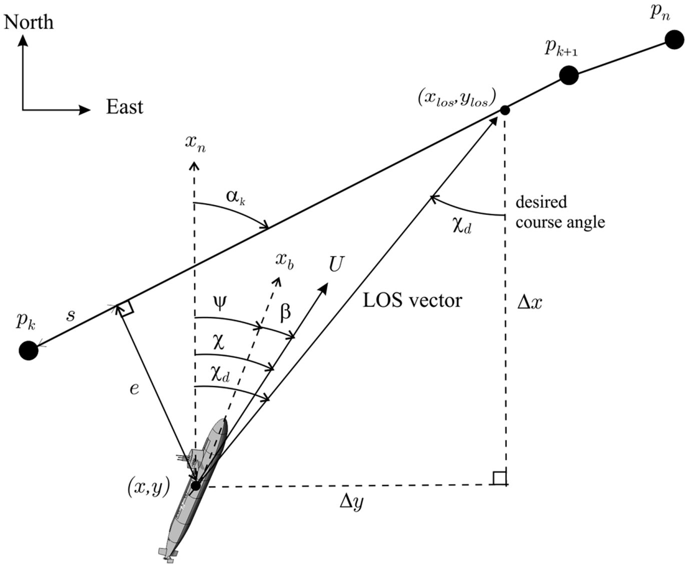

Figure 3.2: Graphical representation of the LOS guidance law. Picture from [24]. The notation of the crosstrack error e relates to the notation y_e used in this thesis.

The objective of the LOS guidance system is to generate a desired course angle χ_d which will lead to

$$\begin{aligned} \lim_{t\to\infty} y_e(t) &= 0 \\ \lim_{t\to\infty} \chi(t) &= \alpha_k \end{aligned} \tag{3.3}$$

It can be shown [27] that in the case with a zero crab-angle, the following guidance law will satisfy (3.3) when combined with a control system:

$$\psi_d(y_e) = \alpha_k + \psi_{\mathrm{LOS}}(y_e) = \alpha_k + \arctan(\frac{-y_e}{\Delta}) \tag{3.4}$$

where ψ_d is the desired heading, and $\Delta > 0$ is a constant knows as the lookahead distance.

3.2 Navigation systems

The objective of a navigation system is to estimate the states of the vehicle. This is usually done be combining a set of sensors and a state estimators.

3.2.1 State estimation

There exist a wide range of state estimators for marine vehicles. The most common is Kalman filter, or, in the nonlinear case, the Extended Kalman filter. Although the Kalman filter usually yields good results and the industry is well familiar with it, the drawback is that is difficult and time-consuming to tune the state estimator. Therefore, there have been extensive research on alternatives such as the nonlinear passive observer, which is based upon Lyapunov theory.

This thesis will not focus on state estimators. For further reading on Kalman filters or nonlinear passive observers, the reader is referred to [24]. For design and analysis of observers for ROVs, the reader is referred to [16, 17].

3.2.2 Sensors

There exists a wide range of sensors for marine vehicles, many of which can be mounted on a ROV. This section will briefly describe a few.

Geo-referenced Positioning Systems

For surface vessels, GNSS is the standard for measuring geo-referenced positions. This method is both cheap, accurate and robust. However, GNSS signals don't penetrate the sea surface, and underwater operations thus require other methods.

For geo-referenced positioning underwater, acoustic positioning systems are often used. In this case, a set of transducers and transponders are placed underwater or mounted on the underwater vehicle, and from the acoustic signals, the transponder position relative to the transducers can be calculated. The three most common acoustic underwater positioning systems are long baseline systems, short baseline systems or ultra-short baseline systems (USBL), all of which have different pros and cons.

The accuracy and range of acoustic positioning systems are dependent on the frequency of the systems. Higher frequency yields higher precision, but also yields a shorter range. High accuracy systems with a long range, require lots of power, which implies heavy and expensive equipment. In general, all acoustic positioning systems require either equipment fixed below the sea surface or mounted upon a mothervessel, which can be costly and limiting with respect to operational range.

IMU

An IMU measures acceleration, turn rates and magnetic components in 3 DOFs. They are small, cheap and accurate, and thus applicable in most applications. A drawback of IMUs are that they are prawn to drifting, and regularly need to be calibrated. For further discussions on IMUs, see [24].

Compass

Compass is an old and well known equipment for measuring heading. They are often cheap and small. The drawback, however, is that compasses are prawn to magnetic disturbances.

Pressure gauges

Pressure gauges are used to measure the depth of underwater vehicles. The depth of the vehicle can be calculated by measuring the pressure relative to the atmospheric pressure.

Doppler Velocity Log

DVL systems are another popular navigational tool for marine vehicles. They consist of a transducer head which sends multiple hydro-acoustic signals towards the seabed. The velocity is then calculated by measurement of the Doppler shift in the reflected acoustic signals. The most common DVL configuration is the Janus configuration, which consist of four transducers pointing towards the fore, aft, port and starboard of the vehicle, as seen in Figure 3.3.

A DVL outputs the surge, sway and heave velocity, and the measurement equations are given by [18]

$$\boldsymbol{v}^d_{d/e} = \boldsymbol{R}^d_b(\boldsymbol{\Theta}_{db}) \left(\boldsymbol{v}^b_{b/n} + \boldsymbol{\omega}^b_{b/n} \times \boldsymbol{r}^b_{\mathrm{dvl/b}} \right) + \boldsymbol{w}^d_{\mathrm{dvl/b}} \tag{3.5}$$

Here, $\boldsymbol{v}^d_{d/e} \in \mathbb{R}^3$ is the measured velocity in the DVL frame $\{d\}$, $\boldsymbol{R}^d_b(\boldsymbol{\Theta}_{db})$ is the rotation matrix between $\{d\}$ and $\{b\}$, $\boldsymbol{r}^b_{\mathrm{dvl/b}} \in \mathbb{R}^3$ is the vector from CO to the origin of $\{d\}$, while $\boldsymbol{w}^d_{\mathrm{dvl/b}} \in \mathbb{R}^3$ is the measurement noise. For further discussion on the theory of DVL, see [53].

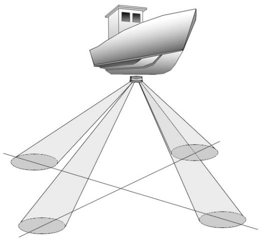

Figure 3.3: DVL system pointing towards the seabed. Picture from [53].

In [19], DVL measurements are used to measure a ROV altitude relative to the seafloor, and subsequently used in the design of an altitude control system. In [54], it is shown that DVL systems are able to interact with net pens, and can thus be used by a ROV to calculate distance and velocity relative to a net pen. These findings will be further explored in the thesis.

3.3 Control Systems

The objective of the control system is to determine the actuation forces necessary for achieving some control objective. Typical control objectives for marine vehicles are set point regulation, dynamic position, path following or trajectory tracking. The inputs to the control system can be the references, the estimations of vehicle states and estimations of environmental disturbances. The outputs of the control system are the forces applied to every actuator. This section will present a very brief introduction to marine motion control. For further reading on marine motion control in general, see [24]. For motion control of underwater robots, see [1].

3.3.1 PID Control

As in many types of systems, variations of PID control is widely used in marine motion control. Due to the PID structure's independence of the vehicle model, it often proves to be a simple, yet somewhat robust method of control. A main drawback of PID control is the time-consuming process of parameter tuning. Furthermore, PID do not directly address nonlinearities of the system, and, consequently, strong nonlinearities may have large impacts on the performance.

3.3.2 Feedback Linearization

Feedback linearization is a powerful control technique which aims to cancel out nonlinearities in order to bring the system in to a linear model. Then, familiar techniques such as pole placement algorithms can be employed. Feedback linearization require that the vehicle model is known and that the system is input-output linearizable (see [32]). Integrator backstepping is a popular variant of feedback linearization which can prove to be more robust by not canceling stabilizing terms.

When using feedback linearization, modeling errors can potentially be destabilizing, thus pointing out the importance of a correct model. As kinetic models for ROVs are typical hard to derive, the performance of feedback linearization controllers for ROVs can prove to be unsatisfying in practice.

3.3.3 Optimal Control Theory

For many applications in marine motion control, optimal control theory can be applied. Optimal control theory deals with finding a control input which minimizes a cost function, while simultaneously staying within specified constraints. Typically, this cost function is a function of control input and tracking errors. Control schemes such as the linear quadratic regulator (LQR) or model predictive control (MPC) are common.

3.3.4 Sliding Mode Control

Sliding mode control (SMC) is a control technique which have been successfully implemented in a wide range of applications, including underwater vehicles. It is recognized as a control method which is particularly robust to perturbed systems with matched disturbances and modeling uncertainties. The idea is to constraint the dynamics of the system to a manifold where the dynamics of the system is exponentially stable. By introducing a control law which will drive the system states to the manifold, the system states will thereafter ”slide” to the wanted equilibrium due to the stability on the manifold.

3.3.5 Adaptive Control

Adaptive control theory is another control theory which can be applied for underwater vehicles. The motivation behind adaptive control is to control processes where the parameters are assumed to be unknown. The idea is then to perform some online estimation of the process parameters based upon the tracking error. Furthermore, the control parameters will be adjusted according to the estimation of the process parameters. For further discussion on adaptive control, the reader is referred to [29] and [58].

3.3.6 Control Allocation

Control allocation is the task of distributing the generalized control forces $\boldsymbol{\tau}_c \in \mathbb{R}^n$ to the control inputs $\boldsymbol{u} \in \mathbb{R}^m$ such as propellers and rudders. Constraints such as rate and amplitude saturations make this an optimization problem. For further reading, see [24, 31].

Chapter 4

Literature Review

4.1 Sea State at Aquaculture Sites

Motivated by good water quality, as well as the lack of availability of sheltered sites, several aquaculture sites have relocated to more exposed areas in recent years. The harsh conditions at these sites, as well as the unique flow patterns in net pens, makes motion control challenging.

In [37], an estimate of wind wave loads on Norwegian aquaculture sites is presented. By combining historic wind data with maps used to calculate the length of water which a given wind has blown, the significant wave height H_s from the sites can be calculated. When considering a return period of 50 years, 38% of the sites experienced a significant wave height H_s larger than 1m, while H_s exceeds 2.5m for 1.4% of the sites. Sites from the county of Sør-Trøndelag experienced by far the most wind wave exposure. When considering a return period of 1 year, H_s exceeds 1m for 47% of these sites, an exposure characterized as ”Large exposure” by Norwegian Standard NS 9415 [46]. It should be noted that this method only consider wind waves, and swell waves are not included.

In [34], wave, wind and current loads were measured at two exposed aquaculture sites over several months. At a depth of 4 meters, the largest recorded current speed was 0.63 m/s, while the largest recorded significant wave height was 3.5 m, which is categorized as ’Extreme exposure’ by [46]. Furthermore, the fish themselves also influence the flow pattern in fish cages. Fish cages may hold more than 1000 tons of biomass. In [28], the current effects of fish swimming patterns in fish cages are studied. Experiments inside stocked fish cages show that the surface water converges towards the center of the cage, where it sinks and spreads out at the bottom of the biomass. Hence, assuming irrational current flow inside fish cages may be invalid.

Finally, as net pens are flexible structures, they are prone to deformations caused by currents and waves. There is extensive study on the interaction between fish cages, currents and waves, see for instance [35, 36, 43]. For current velocities over 0.6 ms^{-1}, a reduced net pen volume of 30 % has been reported [33].

4.2 Bathymetric SLAM and Altitude Estimation

Simultaneous localization and mapping (SLAM) is a common task in robotics, where the problem is to construct a map of an unknown environment, while simultaneous determine the agents position and orientation (POSE) relative to the map. Bathymetric SLAM is the task of mapping the seabed, as well as determining the POSE of the underwater vehicle relative to the seabed.

Bathymetric maps have proven to be a valuable resource for objectives such as seafloor monitoring, pipeline inspections or marine habitat monitoring. These maps can be constructed by using a multibeam depth profiler on underwater vehicles such as AUVs traveling close to the seafloor. However, the mapping efforts can be hindered by the navigation error in the localization estimate of the vehicle. The localization typically require a mothervessel, as well an underwater positioning system such as USBL. The method require a high precision on the position estimate, as well as maintaining the distance between the underwater vehicle and the mothervessel within the range of the positioning system.

With this is mind, an alternative is to use the map being built to improve the position estimations by performing SLAM. A common approach to SLAM is to identify landmarks whose position is known or can be calculated. However, the unstructured nature of the seabed environment makes it difficult to identify distinct landmarks. In [4], a bathymetric SLAM method without needing to explicitly identify landmarks is proposed, where a Rao-Blackwellized particle filter (RBPF) is used to track uncertainty in the vehicle states, with each particle maintaining a grid-based 2D depth map. In [55], a RBPF with grid-mapping for AUV using a forward-looking sonar is proposed. The suggested method enables SLAM in enclosed underwater environments without any types of landmarks, for example in aquaculture net pens.

In [2], a method for localization and mapping of flexible underwater structures, such as net pens and mooring lines, is proposed. The methodology is based upon a network of acoustic transmitters placed upon the structure. From the position of the transmitters, a point on the structure is estimated. All the point positions are interpolated and applied in the mapping software Octomap, to build a digital map representation of the whole structure.

In [11], a gradient-based altitude estimation and bottom-following control law is proposed. Here, echo-sonders has been placed on the fore and aft of a ROV. From these two measurements, the altitude of the vehicle relative to the bottom is estimated, as well as the slope of the seafloor. Furthermore, a PI-controller with feedforward from the slope of the seafloor is proposed for bottom-following.

In [19], a method for altitude control and terrain following by the use of DVL is proposed. Here, a DVL system is mounted on a ROV, pointing toward the seafloor. From the set of the four DVL beam vectors, the seabed is, at each timestep, approximated as a flat surface. Furthermore, using that the altitude rate relative to the approximated seafloor is coupled with the velocity of the vehicle, a Kalman filter is designed to estimate the altitude. Finally, the article proposes a guidance law for depth reference with a feedforward term based on the altitude rate of change.

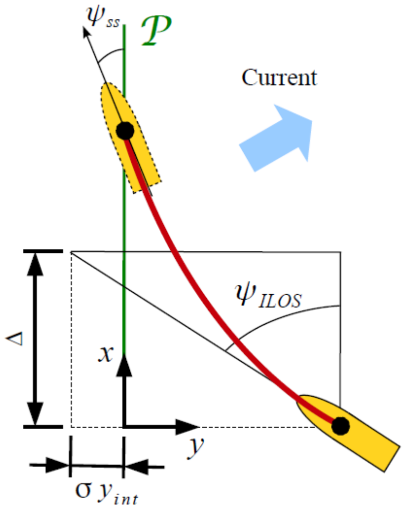

Figure 4.1: The integral line of sight guidance law. At steady state, a nonzero crab angle ψ_{ss} allows an underactuated vehicle counteract the currents. Picture taken from [12].

4.3 Path Following

4.3.1 Integral Line-Of-Sight Guidance

From the relationship given by $\chi = \psi + \beta$, it follows that (3.4) will only satisfy (3.3) in the case of zero slip-angle β. Therefore, environmental disturbances such as ocean currents propose a serious challenge for LOS guidance, and have to be dealt with. If β is know, then its effects can be canceled by feedforward action. If not, other approaches has to be considered.

In [6], it is shown how including integral action with LOS is able to tackle constant and irrotational currents. The paper suggests extending ψ_{LOS} according to

$$\begin{aligned} \psi_{\text{ILOS}} &= \arctan\left(\frac{-y_e - \sigma y_{\text{int}}}{\Delta}\right) \\ \dot{y}_{\text{int}} &= \frac{\Delta y_e}{(y_e + \sigma y_{\text{int}})^2 + \Delta^2} \end{aligned} \tag{4.1}$$

where σ is a design parameter. The integral action allows the ship to maintain a non-zero steady-state crab angle $\psi_{ss} \in [-\pi, \pi]^T$ in order to counter the effects of the currents by using its surge thrusters. Notice that the integral effect diminishes when the crosstrack error increases, thus reducing the risk of wind-up. Figure 4.1 provides a geometrical interpretation of the ILOS guidance law.

The control objective can by formulated as

$$\begin{aligned} \lim_{t\to\infty} y_e(t) &= 0 \\ \lim_{t\to\infty} \psi(t) &= \psi_{ss} \end{aligned} \tag{4.2}$$

In [13], it is proven that the ILOS guidance system in a closed loop system will make the crosstrack error dynamics uniformly globally asymptotically stable (UGAS) and uniformly locally exponentially stable (ULES) in the case of constant and irrotational currents for straight line path following. Particularly, it is shown that $[y_e, y_{\text{int}}]^T$ will converge to some equilibrium $[0, y_{\text{int}}^{\text{eq}}]^T$. In [14], it is shown how the ILOS law can be utilized by an underactuated surface vessel with saturated transverse actuators. By utilizing the transverse actuators, the steady-state crab angle ψ_{ss} can be reduced. In [15], it is shown how combining the ILOS guidance law with adaptive surge-yaw controllers can handle both kinematic and dynamic disturbances.

The ILOS guidance law can be extended to the 3D path following case according to

$$\begin{aligned}\theta_{\text{ILOS}} &= \tan^{-1}\left(\frac{z_e + \sigma_z z_{\text{int}}}{\Delta_z}\right)\\ \dot{z}_{\text{int}} &= \frac{\Delta_z z_e}{(z_e + \sigma_z z_{\text{int}})^2 + \Delta_z^2}\\ \psi_{\text{ILOS}} &= \tan^{-1}(\frac{-y_e - \sigma_y y_{\text{int}}}{\Delta_y})\\ \dot{y}_{\text{int}} &= \frac{\Delta_y y_e}{(y_e + \sigma_y y_{\text{int}})^2 + \Delta_y^2}\end{aligned} \tag{4.3}$$

where y_e, z_e represent the horizontal and vertical crosstrack errors respectively.

4.3.2 Path Following for Curved Paths

The LOS guidance law is still able to achieve its objectives for path following for general continuous paths, as shown in [26]. Here, a continuous path $\mathcal{C}(\theta)$ is described with with a path variable $\theta \geq 0$ so that the reference frame is centered in the point $[x_p(\theta), y_p(\theta)]$. The geometrical interpretation is shown in Figure 4.2. The path-tangential angle is then described by

$$\gamma_p(\theta) = \arctan(y_p^{'}(\theta), x_p^{'}(\theta)) \tag{4.4}$$

The dynamics of the crosstrack error can be described by

$$\dot{y}_e(\theta) = U \sin\left(\chi - \gamma_p(\theta)\right) \tag{4.5}$$

A LOS guidance law given by

$$\chi_d = \gamma_p(\theta) + \psi_{\text{LOS}} \tag{4.6}$$

is shown to lead to uniform semi-global exponential stability (USGES) properties for the crosstrack error y_e. In [42], the results from [26] are extended to include constant and irrotational currents.

An alternative approach is to chose the path-fixed reference frame as the Serret-Frenet frame [20, 24]. The Serret-Frenet reference frame $\{f\}$ is anchored in a continuous differentiable curve $\mathcal{C}$ with axes along the tangent, the normal and the binormal of $\mathcal{C}$. The curve can now be parameterized by the arc length s, as well as the deviation of position and orientation $[x_{b/f}, y_{b/f}, \psi_{bf}]^T$ between the vehicle and $\{f\}$. The first derivative of s is left as a design parameter.

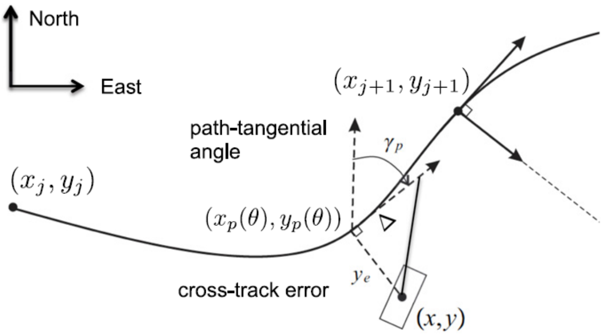

Figure 4.2: The LOS guidance geometry for curved paths. Picture is taken from [26].

In [41], the following update law and guidance law is proposed:

$$\begin{aligned}
\dot{s} &= \sqrt{U_{rd}^2 + v_r^2}\,\frac{\sqrt{\Delta^2 + x_{b/f}^2} + x_{b/f}}{\sqrt{\Delta^2 + x_{b/f}^2 + (y_{b/f} + g)^2}} + \hat{V}_x^f \\
\psi_d &= \psi_f - \arctan\left(\frac{v_r}{U_{rd}}\right) - \arctan\left(\frac{y_{b/f} + g}{\sqrt{\Delta^2 + (x_{b/f})^2}}\right)
\end{aligned} \tag{4.7}$$

where g is the solution to the second order equation

$$(\hat{V}_y^{f^2} - U_c^2)g^2 + 2\hat{V}_y^{f^2} y_{b/f} g + \hat{V}_y^{f^2}(\Delta^2 + x_{b/f}^2 + y_{b/f}^2) = 0, \tag{4.8}$$

and $[\hat{V}_x^f, \hat{V}_y^f]$ are estimates of the velocity of the current in $\{f\}$. It is shown that under certain relaxed conditions on the curve and the lookahead-distance, path following properties are achieved.

4.3.3 Line-Of-Sight Guidance for Fully-Actuated Vehicles

LOS was first developed as a solution to the underactuated path following control problem. The principles for LOS guidance for underactuated vehicles is as applicable for fully-actuated vehicles as for underactuated vehicles. However, as pointed out by [8] and [18], for fully-actuated vehicles, LOS guidance can instead output a desired velocity vector. By controlling the surge and sway velocity, the ROV heading angle is decoupled from the desired course angle, and path following can be achieved independently of the heading. The course angle can thus be controlled using a LOS algorithm, while the heading angle can then be controlled to follow some auxiliary objective. For ROV inspection tasks, this can be advantageous, as the camera-view, which is aligned with the ROV heading, can be directed towards the objects of interest instead of being dictated by the path.

4.4 Higher-Order Sliding Mode Control

Since modeling inaccuracies may have strong impact on highly nonlinear systems, they should be addressed by the control system. Sliding mode is generally recognized as a control method which is robust to unmodeled disturbances. The early work on sliding mode control stems from the former Soviet Union, while work in the eighties and nineties made it more common, see for instance [58].

In general, the idea is to limit the dynamics of the system to a manifold, where the dynamics of the system is exponentially stable. Let $s = f(x, t)$ define the sliding variable. When $s = 0$, the system dynamics is on the sliding manifold. The challenge is then to design a control law which drives the system dynamics to $s = 0$. This control law will typically be on the form $u(t) = K\ \mathrm{sgn}(s) + v$, where K is some constant, and v could be some other control input dependent on the system dynamics.

The point of the signum function, is that it will be a stabilizing term which will dominate bounded disturbances. Although this function indeed has a stabilizing effect, it exists some practical challenges when implementing sliding mode controller. One price to pay for robustness, is that the signum function will typically lead to high input activity. Another major challenge is a phenomena known as *chattering*, which is connected with the imperfect implementation of the switching of the signum function. For the signum function to be ideal, the sign will have to change instantaneously when crossing 0. However, in practical implementation, delay and measurement noise makes the instantaneous switching impossible to implement. Therefore, the sliding mode control law with signum function will lead rapid oscillation with finite frequency and amplitude known as chattering.

One way to avoid this problem is to replace the signum function with a function which is continuous around the origin, such as $\tanh(s/\phi)$ or a high-slope saturation function given by

$$\mathrm{sat(s/}\phi) \triangleq \begin{cases} \mathrm{sgn(s)}, & |s/\phi| > 1 \\ s/\phi & \text{otherwise} \end{cases} \tag{4.9}$$

where ϕ is a small, positive constant known as the boundary layer thickness. When replacing the signum function with a continuous replacement, the control law does not necessarily drive the dynamics to $s = 0$ (see [32]). For many systems, one can only ensure that the dynamics converges to the boundary layer, ie. $|s| \leq \phi$. To achieve stability inside the boundary layer, careful design of the control law may be required.

Another attempt at dealing with chattering, is higher-order SMC. In general, higher-order SMC removes the restriction that the control input u has to appear in the first derivative of the sliding surface s. The switching control is confined to the higher derivatives of the system input, so that the latter is continuous and chattering is avoided while still being able to use the unmodified signum function. For a general survey of second-order sliding control laws, see [5].

In [39], the super-twisting algorithm (STA), a second order sliding mode control law, was proposed as

$$\begin{aligned} u_{\mathrm{STA}} =& -k_1|s|^{1/2}\mathrm{sgn}(s) + v \\ \dot{v} =& -k_2\mathrm{sgn}(s) \end{aligned} \tag{4.10}$$

where k_i are design parameters. Compared to many other 2nd order versions of SMC, STA has the strength that it is also applicable to systems where the input appears in the first derivative of s. In [56], a version of STA with adaptive gains were proposed, with a more general adaptive law given in [57].

In [7], an application of STA with adaptive gains for trajectory tracking for an Articulated Intervention-AUV (AIAUV) is presented. A higher-order sliding mode observer for state estimation is designed, where the estimation error, under certain relaxed assumptions, will converge to zero. Furthermore, a feedback linearizing control law is designed which will drive the dynamics of the sliding surface to

$$\dot{s} = u_{\text{STA}}, \tag{4.11}$$

which will lead to closed-loop stability.

4.5 Differential games and mixed H_2/H_∞ control

The aim of mixed H_2/H_∞ control is to simultaneously ensure robustness to disturbances and optimal control. The former is subject to optimal control, where the objective is to optimize a given object function which minimizes the energy of a control variable. The latter is subject to noise attenuation, and is equivalent to the worst-case problem.

While it is well known the H_∞ problem can be formulated as a two-player, zero-sum differential game, the mixed H_2/H_∞ problem can be formulated as a nonzero-sum differential game. In [44], a Nash-game approach to solve the mixed H_2/H_∞ problem is proposed on a input-affine, nonlinear, single integrator system. By solving a set of algrebraic Riccati equations (ARE), an approximated solution to the problem is presented. In [62], the theory of [44] is extended to double integrator input-affine, nonlinear systems and applied on an AIAUV, rejecting disturbances introduced by modeling errors.

4.6 Learning Model Predictive Control For Iterative Tasks

Often many tasks where control is desired has a repetitive nature. Therefore, there has been extensive studies on repetitive control. In Iterative Learning Control (ILC), each trial of the task is labeled an iteration, and the control system strives to learn from previous iterations. The system starts from the same initial condition at each iteration, and the control objective is to track a given reference, rejecting periodic disturbances.

Early research on combining ILC with MPC has been conducted in [38], where the authors uses a proposed control technique called Batch MPC (BMPC) to a control linear time-varying MIMO model of a batch processes. This technique, as well as other early examples on Learning MPC (LMPC), assumes that the reference signal does not change from iteration to iteration.

In [52], it is studied how nonlinear MPC with iterative learning can be used to control iterative tasks for nonlinear systems where the reference signals is not known in advance, and may change from iteration to iteration. A safe-set is defined, which is a collection of states trajectories associated with successful iterations. A cost function is presented, where one of the constrained is that the final state on the receding horizon is in the safe-set. At each successful iteration, the safe-set is expanded. Under the assumption that the starting safe-set is nonempty, recursively feasibility and stability is proven, as well as non-increasing cost function at each iteration.

In [9], the proposed theory is demonstrated in an experiment with an autonomous racing car. In this scenario, the terminal condition of one iteration, is the same as the initial condition in the next iteration. The objective is to minimize the lap time, while staying within the track. From experiments, it is demonstrated that the lap-time decreases from the first lap and converges towards a steady-state lap-time. In [10], an adaptive LMPC strategy is proposed. Here, adaptive control methodology is combined with learning MPC, such that, with every iteration, model uncertainty is learned to produce more accurate state trajectories.

Part III

Method

Chapter 5

Overview and Control Objective

This part of the thesis will propose a control strategy which have the aim of making the ROV autonomously traverse the net pen. First, it will be shown how a DVL installed on the frontal side of the ROV can be used to approximate the shape of a local region of the net pen, see Fig. 5.2. Secondly, a guidance law is presented which will guide the ROV along the approximated net pen. Finally, a set of control laws is suggested with the aim of ensuring closed-loop stability.

Figure 5.1 gives an overview of signal flow of the GNC system. From approximated net pen, the desired heading ψ_d and the distance $d_{b/\text{net}}$ of the ROV relative to the approximated net pen is calculated. The guidance systems then calculates the desired surge and sway velocity u_d, v_d and the control system calculates the generalized control forces $\boldsymbol{\tau}_c$.

The overall objective is two-fold and can be presented by two independent control objectives.

5.1 Objectives for Net Pen Approximation

Let $\boldsymbol{p}^n_{b/\text{net}}$ be the vector from the CO to the closest point on the net pen, and $\boldsymbol{p}^n_{\text{projection}}$ its projection onto the north-east plane. Furthermore, let $d^*_{b/\text{net}} \triangleq ||\boldsymbol{p}^n_{\text{net}}||_2$ be the minimal distance from the CO to the net pen. Finally, let ψ^* be the angle between $\boldsymbol{p}^n_{\text{projection}}$ and the north-axis. The geometrical interpretation is shown in Figure 5.3.

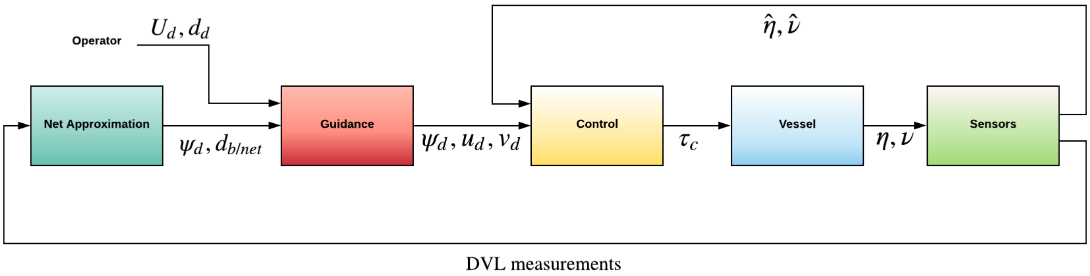

Figure 5.1: Overview of the guidance, navigation and control system.

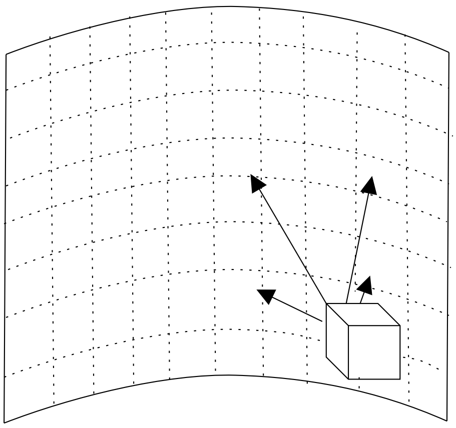

Figure 5.2: ROV with a DVL traversing a net pen.

The objectives for the net pen approximation can then be formalized as

$$d^*_{b/\text{net}} - d_{b/\text{net}} = 0 \tag{5.1}$$

$$\psi^* - \psi_d = 0 \tag{5.2}$$

where $d_{b/\text{net}}$ is an estimate of $d^*_{b/\text{net}}$ and ψ_d is an estimate of ψ^*. Furthermore, define the crosstrack error $y^*_e \triangleq d^*_{b/\text{net}} - d_d$ and approximated crosstrack error $y_e \triangleq d_{b/\text{net}} - d_d$, where $d_d > 0$ is the constant desired distance to the net. The angle ψ_d will be the desired heading transferred as a reference signal to the motion controller, while the guidance law will calculate references signals for velocity control with the aim of minimizing the approximated crosstrack error y_e.

5.2 Objectives for Motion Control

The objectives for the motion controller is to follow the net pen at a constant distance d_d with the ROV heading normal to the net pen and with a constant speed. This can be formalized as

$$\lim_{t\to\infty} y_e(t) = 0 \tag{5.3}$$

$$\lim_{t\to\infty} (\big(\psi(t) - \psi_d(t)\big) = 0 \tag{5.4}$$

$$\lim_{t\to\infty} U(t) - U_d = 0 \tag{5.5}$$

where $U \triangleq \sqrt{u^2 + v^2}$ the ROV speed and $U_d > 0$ the desired speed.

5.3 Outline

This part of the thesis is organized as followed:

- In Chapter 6, a method for approximating the geometry of a local region of a net pen from DVL measurements is proposed. Furthermore, it will be shown how one can calculate the ROV position and orientation relative to the approximated net pen structure.

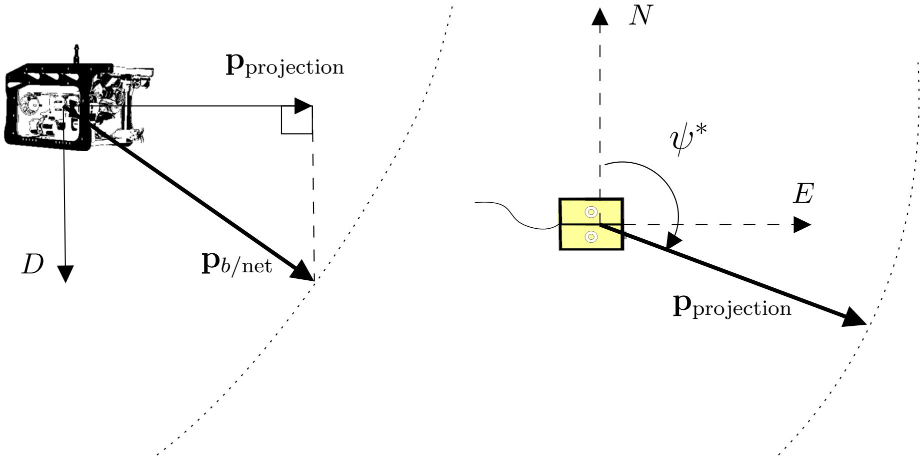

(a) Vertical projection. (b) Horizontal projection.

Figure 5.3: ROV position relative to the net pen, where $\boldsymbol{p}_{b/\text{net}}$ is the vector from the CO to the nearest point on the net pen, $\boldsymbol{p}_{\text{projection}}$ its projection onto the north-east plane and ψ^* is the angle from x^n to $\boldsymbol{p}_{\text{projection}}$.

- Chapter 7 proposes the guidance law.
- Chapter 8 proposes control laws designed to control the vessel states.

Chapter 6

Net Pen Geometry Approximation from DVL Measurements

This chapter shows how one can use a DVL system to approximate the geometry a local region of the net pen as a plane. Furthermore it will be shown how to calculate the distance $d_{b/net}$ of the CO relative to the approximated plane, and the desired angle ψ_d as explained in Sec. 5.1.

6.1 DVL Beams Representation

Consider a 4 beam DVL system mounted on the frontal side of a ROV pointing forward. Let $\{d\}$ denote the the reference frame fixed with the the DVL systems, with the x^d axis pointing straight out. The DVL jth beam is shown in Fig. 6.1, and is represented by the vector

$$\boldsymbol{r}_j^d = \begin{bmatrix} x_j^d \\ y_j^d \\ z_j^d \end{bmatrix} = a_j^d \begin{bmatrix} 1 \\ \tan(\gamma_j)\cos(\beta_j) \\ \tan(\gamma_j)\sin(\beta_j) \end{bmatrix} \tag{6.1}$$

where a_j^d is the horizontal component of $\boldsymbol{r}_j^d$, γ_j the rotation about the DVL y^d axis and β_j the rotation about the z^d axis. The angles β_j, γ_j are constant and known, while a_j^d is measured.

6.2 Net Pen Approximation

To approximate a plane, three points are needed. Therefore, one can approximate the net's surface as a plane from three DVL beams. Furthermore, from a set of four returning DVL beams, one can use a best fitting method between the points to best approximate a plane.

Let the plane equation $f(x, y, z) = -x + by + cz + d = 0$ be an approximation of the net pen surface, represented in $\{d\}$. Using least-squares, one can derive this approximation from a set of four DVL beams by minimizing the object function

$$\sum_{J=1}^{4} [a_j^d - (by_j^d + cz_j^d + d)]^2 \tag{6.2}$$

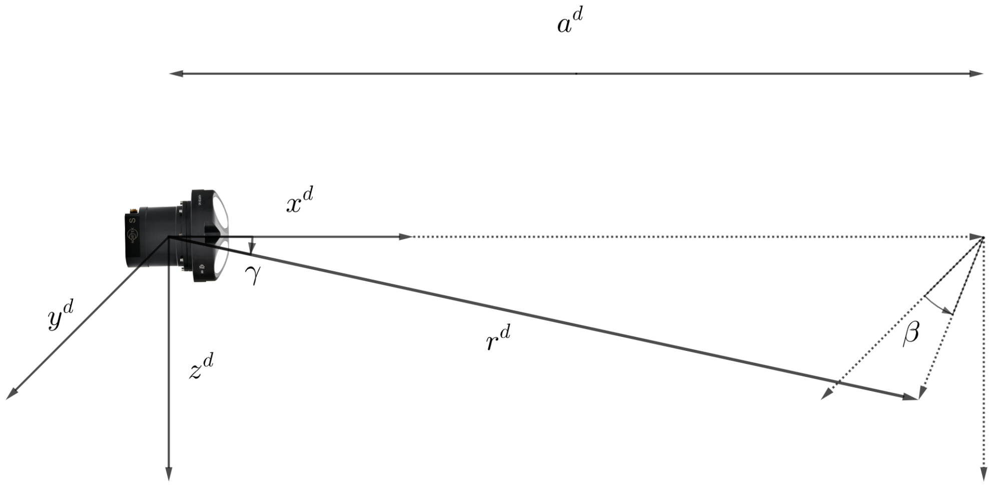

Figure 6.1: The DVL beam vector components.

The system

$$\boldsymbol{Ax} = \begin{bmatrix} y_1^d & z_1^d & 1 \\ y_2^d & z_2^d & 1 \\ y_3^d & z_3^d & 1 \\ y_4^d & z_4^d & 1 \end{bmatrix} \begin{bmatrix} b \\ c \\ d \end{bmatrix} = \begin{bmatrix} a_1^d \\ a_2^d \\ a_3^d \\ a_4^d \end{bmatrix} = \boldsymbol{b} \tag{6.3}$$

is found by solving $\boldsymbol{A^T Ax} = \boldsymbol{A^T b}$.

Furthermore, the normal vector to the plane in the $\{d\}$ reference frame is given by

$$\boldsymbol{n}^d = \begin{bmatrix} -1 & b & c \end{bmatrix}^T \tag{6.4}$$

6.3 Calculation of the Desired Heading

In order for the ROV heading to be pointed directly towards the net pen approximation, the ROV will have to be aligned with the horizontal projection of the normal vector $\boldsymbol{n}^d$.

Let $\boldsymbol{n}^n$ be the normal vector $\boldsymbol{n}^d$ rotated to $\{n\}$. Furthermore, let the vector $\boldsymbol{Z}^n = [0, 0, 1]^T$ denote the normal vector to the horizontal north-east plane. The projection of $\boldsymbol{n}^n$ onto the north-east plane is then given as

$$\boldsymbol{n}^n_{\text{projection}} = \begin{bmatrix} x^n_{\text{projection}} \\ y^n_{\text{projection}} \\ 0 \end{bmatrix} = -\boldsymbol{Z}^n \times \boldsymbol{n}^n \times \boldsymbol{Z}^n \tag{6.5}$$

The negative sign in equation (6.5) makes $\boldsymbol{n}^n_{\text{projection}}$ point in the direction from the ROV towards the approximated plane, see figure 6.2.

The angle ψ_d between x^n and $\boldsymbol{n}^n_{\text{projection}}$, ie. the desired heading angle, is then given by

$$\psi_d \triangleq \text{atan2}(y^n_{\text{projection}}, x^n_{\text{projection}}) \tag{6.6}$$

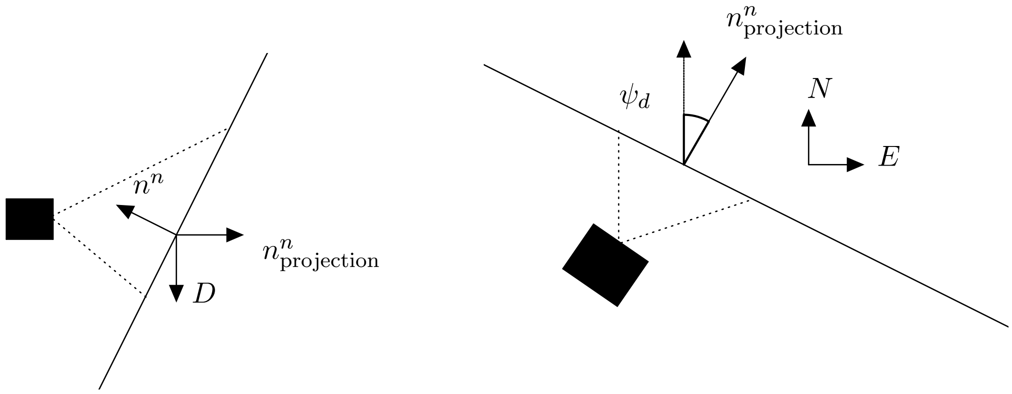

(a) Vertical plane projection (b) Horizontal plane projection

Figure 6.2: Relationship between $\boldsymbol{n}^n, \boldsymbol{n}^n_{\text{projection}}$ and ψ_d.

6.4 ROV Distance Relative to the Approximated Net Pen

The shortest distance $d_{b/\text{net}}$ between the CO and the plane can be calculated from the inner-product between $\boldsymbol{n}^d$ and the vector from the CO to the point where the x^d intersects the plane.

Let the vector from the CO to the DVL in $\{d\}$ be defined as

$$\boldsymbol{p}^d_{\text{dvl/b}} \triangleq \begin{bmatrix} x^d_{\text{dvl/b}} \\ y^d_{\text{dvl/b}} \\ z^d_{\text{dvl/b}} \end{bmatrix} \tag{6.7}$$

Furthermore, the unit normal vector to the plane is given by

$$\boldsymbol{n}^d_{\text{unit}} = \frac{\boldsymbol{n}^d}{||\boldsymbol{n}^d||_2} = \frac{1}{\sqrt{1+b^2+c^2}} \begin{bmatrix} -1 \\ b \\ c \end{bmatrix} \tag{6.8}$$

Revisiting the equation for the approximated plane, the equation can be rewritten to

$$f(x,y,z) = -(x-x_0) + b(y-y_0) + c(z-z_0), \tag{6.9}$$

where $\boldsymbol{p}^d_0 = [x^d_0, y^d_0, z^d_0]^T$ is the point where x^d intersects the plane and $d = x_0 - by_0 - cz_0$. The vector from $\boldsymbol{p}^d_0$ to the CO is then given by

$$\boldsymbol{v}^d = -\begin{bmatrix} x^d_{\text{dvl/b}} + x^d_0 \\ y^d_{\text{dvl/b}} + y^d_0 \\ z^d_{\text{dvl/b}} + z^d_0 \end{bmatrix} \tag{6.10}$$

Finally, the distance between the approximated net pen and the CO is given by

$$\begin{aligned} d_{b/\text{net}} &\triangleq \left|(\boldsymbol{v}^d)^T \boldsymbol{n}^d_{\text{unit}}\right| \\ &= \frac{\left|x^d_{\text{dvl/b}} - by^d_{\text{dvl/b}} - cz^d_{\text{dvl/b}} + d\right|}{\sqrt{1+b^2+c^2}} \end{aligned} \tag{6.11}$$

6.5 Prediction of Approaching Corners

Consider a traditional circular fish cage, see Figure 6.3. Due to mooring, a horizontal projection of the fish cage will rarely be shaped like a smooth circle. Instead, there will most likely exists sharp edges at the mooring points. Furthermore, environmental loads can also greatly affect the shape of net pens, effectively deforming the net.

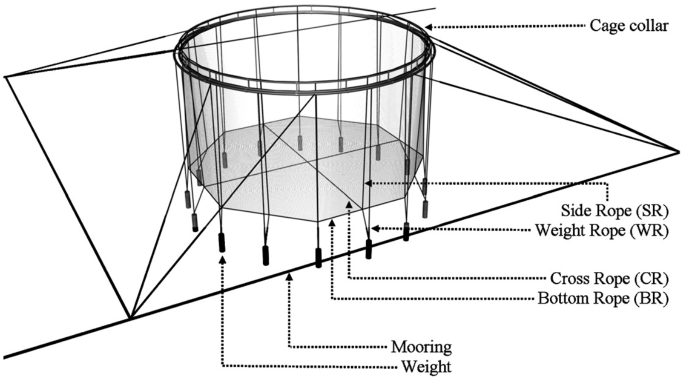

Figure 6.3: Traditional circular fish cage. Picture from [43].

As the DVL system only points towards a local area of the net pen surface, the approximated plane gives little indication of what lies ahead of the ROV. A consequence might be that the ROV will react too late to these sharp edges in the net pen. In response to this, a method for predicting future turns in the net pen is presented.

As stated, the four DVL beams may be used to approximate a plane. However, for a roll/pitch stable ROV moving in sway, two of the DVL beams will project onto the net *ahead* of the ROV, while the two other will project onto the net behind the ROV. Thus, two of the DVL beams yields more information about the future of the net pen surface relative to the others.

Let the DVL beams $\boldsymbol{r}^d_{1,2}$ point ahead of the ROV, and $\boldsymbol{r}^d_{3,4}$ point behind. Define the systems

$$\begin{aligned} \boldsymbol{A_1 x_1} &= \begin{bmatrix} y^d_1 & z^d_1 & 1 \\ y^d_2 & z^d_2 & 1 \\ y^d_3 & z^d_3 & 1 \end{bmatrix} \begin{bmatrix} b_1 \\ c_1 \\ d_1 \end{bmatrix} = \begin{bmatrix} a^d_1 \\ a^d_2 \\ a^d_3 \end{bmatrix} = \boldsymbol{b}_1 \\ \boldsymbol{A_2 x_2} &= \begin{bmatrix} y^d_1 & z^d_1 & 1 \\ y^d_2 & z^d_2 & 1 \\ y^d_4 & z^d_4 & 1 \end{bmatrix} \begin{bmatrix} b_2 \\ c_2 \\ d_2 \end{bmatrix} = \begin{bmatrix} a^d_1 \\ a^d_2 \\ a^d_4 \end{bmatrix} = \boldsymbol{b}_2 \end{aligned} \tag{6.12}$$

which gathers the beam configurations $\{1,2,3\}, \{1,2,4\}$ respectively. Furthermore, define the vector

$$\boldsymbol{x}_f \triangleq \frac{1}{2}\left(\boldsymbol{x}_1 + \boldsymbol{x}_2\right), \tag{6.13}$$

the average of $\boldsymbol{x}_1$ and $\boldsymbol{x}_2$. This vector describes a plane which is weighted with respect to the DVL beams pointing ahead, and should better capture the "future" net pen shape. Following the same procedure as before, one can use this vector to calculate an angle ψ_f, which predicts the future net normal angle. This will be utilized by the guidance system to make the ROV more reactive to turns.

6.6 An Alternative Approach: Generating a Desired Curved Path Relative to the Net Pen

This section will present a method for generating a desired curved path from a approximation of the net pen. The method will approximate a set of three flat planes. Furthermore, a waypoint relative to each plane is calculated. From these three waypoints, it is possible to generate a continuous path, which will be the desired path for the vessel to follow.

6.6.1 Past, Present and Future Plane Approximations

Using the same procedure as in section 6.5, it is possible to calculate three planes which approximates the past, present and future shape of the net pen.

Again, let the DVL beams $\boldsymbol{r}^d_{1,2}$ point ahead of the ROV, and $\boldsymbol{r}^d_{3,4}$ point behind. Now, also calculate a plane described by the vector $\boldsymbol{x}_p$, which is calculated from the beam configurations $\{1,3,4\},\{2,3,4\}$. Like the plane described by $\boldsymbol{x}_f$ approximates the future net shape, the plane described by $\boldsymbol{x}_p$ approximates the past net shape.

6.6.2 Waypoint Generation

Consider the waypoints $\boldsymbol{p}^n_0, \boldsymbol{p}^n_1, \boldsymbol{p}^n_2$ associated with the planes described by the vectors $\boldsymbol{x}_p, \boldsymbol{x}, \boldsymbol{x}_f$ respectively.

Let the plane normal vector projection in $\{n\}$ be given by

$$\boldsymbol{n}^n_{\text{projection,i}} = -\boldsymbol{Z}^n \times \boldsymbol{n}^n_i \times \boldsymbol{Z}^n \tag{6.14}$$

where $\boldsymbol{Z}^n = [0,0,1]^T$ in $\{n\}$ and $i \in \{\text{past,current,future}\}$.

Furthermore, let the tangent vectors to the planes, positive in starboard direction, be given by

$$\boldsymbol{t}^n_{\text{i}} = Z^n \times \boldsymbol{n}^n_{\text{projection,i}} \tag{6.15}$$

Finally, let d_i denote the distance from the CO of the ROV to the approximated plane, d_d the desired distance to the net and $y_{e,i} = d_i - d_d$ the distance error.

Then the three waypoints can be calculated according to

$$\begin{aligned} \boldsymbol{p}^n_0 &= y_{e,\text{past}} \boldsymbol{n}^n_{\text{projecction,past}} - \Lambda \boldsymbol{t}^n_{\text{past}} \\ \boldsymbol{p}^n_1 &= y_{e,\text{current}} \boldsymbol{n}^n_{\text{projection,current}} \\ \boldsymbol{p}^n_2 &= y_{e,\text{future}} \boldsymbol{n}^n_{\text{projection,future}} + \Lambda \boldsymbol{t}^n_{\text{future}} \end{aligned} \tag{6.16}$$

where Λ is a positive constant called the ”along-track gain”. The along-track gain Λ can be seen as a design parameter. A lower Λ will move the waypoints closer to each other, thus potentially creating a sharper bend to the curve. This can make the ROV more reactive to turns. Increasing Λ will have the opposite effect.

For net following in the port direction, (6.15) should be multiplied with -1.

6.6.3 Curve Generation From Waypoints

A method for interpolating a cubic spline from a set of waypoints is described in [24] by considering the cubic polynomials

$$\begin{aligned} x_p(\theta) &= a_3\theta^3 + a_2\theta^2 + a_1\theta + a_0 \\ y_p(\theta) &= b_3\theta^3 + b_2\theta^2 + b_1\theta + b_0 \end{aligned} \tag{6.17}$$

where $(x_p(\theta), y_p(\theta))$ is the position of a particle along the path, and $\theta \geq 0$ is the path variable. At waypoint $\boldsymbol{p}_j^n$, we have $\theta = j$, with $j \in \{0, 1, 2\}$. The cubic polynomials will satisfy $x_p(\theta), y_p(\theta) \in \mathcal{C}^2$, ie. the path is twice differentiable[1].

6.6.4 Net Normal Angle and Crosstrack Error

The path-tangential angle is given by

$$\gamma_p(\theta) = \text{atan2}(y_p^{'}(\theta), x_p^{'}(\theta)) \tag{6.18}$$

Furthermore, at position $\{x_p(\theta), y_p(\theta)\}$ the normal line is given by

$$y - y_p(\theta) = -\frac{1}{\tan(\gamma_p(\theta))}(x - x_p(\theta)) \tag{6.19}$$

and the crosstrack error is given by

$$y_e(\theta) = -(x - x_p(\theta))\sin(\gamma_p(\theta)) + (y - y_p(\theta))\cos(\gamma_p(\theta)) \tag{6.20}$$

where $[x, y]^T$ is the position of the vessel in $\{n\}$ [26].

For an open curve, there exists a unique solution for the minimal crosstrack error $y_e(\theta^*)$, which is found by solving the nonlinear optimization problem

$$\theta^* \triangleq \arg\min_{\theta \geq 0} \left\{ \frac{U(t)}{x_p^{'}(\theta)^2 + y_p^{'}(\theta)^2} \right\} \tag{6.21}$$

subject to

$$y - y_p(\theta) = -\frac{1}{\tan(\gamma_p(\theta))}(x - x_p(\theta))$$

The desired heading is then given by

$$\psi_d = \gamma_p(\theta^*) \pm \frac{\pi}{2}, \tag{6.22}$$

positive for path following in the port direction, negative for path following in the starboard direction.

It is worth noting that the derivatives of ψ_d can be calculated algebraically with this approach. The derivative values can then be used in a heading controller.

---

[1] At the boundaries $\boldsymbol{p}_0^n, \boldsymbol{p}_2^n$, it is possible this will not hold, see [24].

Chapter 7

Guidance System

This chapter proposes a guidance law, which will calculate reference values that will satisfy the control objective in Equations (5.3),(5.5) if successfully tracked. The guidance law is inspired by the LOS guidance law. However, the guidance law utilizes that a ROV is actuated in 4DOF. Thus, the ROV can maintain a fixed heading relative to the path, and instead minimize the crosstrack error by crabbing. This can be done indirectly by controlling the surge velocity u and sway velocity v.

If a guidance law is to achieve path following properties, the reference signals have to be properly tracked by the control system. When analysing the stability properties of the crosstrack error, it is therefore common to analyze a cascaded system where the dynamics of the crosstrack error is perturbed by the tracking error of the vehicle states. This chapter only concerns the guidance laws, and it is therefore assumed that control laws are already designed to ensure that vehicle states are successfully tracked. Chapter 8 will discuss the design of control laws for the vehicle states.

7.1 Guidance Law

This section proposes the guidance law which generates the desired surge and sway velocities u_d, v_d.

Let the desired heading ψ_d be rotated a desired angle $\alpha \in [-\pi, \pi]$ about the path-tangential angle γ_p:

$$\psi_d \triangleq \gamma_p + \alpha \tag{7.1}$$

Then the desired velocity in surge and sway is given by

$$\begin{aligned} u_d &= U_d \cos\left(-\tilde{\psi} - \alpha - \arctan\left(\frac{y_e}{\Delta}\right)\right) \\ v_d &= U_d \sin\left(-\tilde{\psi} - \alpha - \arctan\left(\frac{y_e}{\Delta}\right)\right) \end{aligned} \tag{7.2}$$

where $U_d > 0$ is the desired vehicle speed and $\tilde{\psi} \triangleq \psi - \psi_d$ is the yaw tracking error. Notice that (7.2) also defines $U_d \triangleq \sqrt{u_d^2 + v_d^2}$.

For the specific case of net pen inspection, the desired heading is normal to the path. This yields $\alpha = \pi/2$ when the ROV is directed towards the port direction along the net pen, while net pen following in the starboard direction yields $\alpha = -\pi/2$. However, the guidance law is not limited to these cases, and α can be chosen freely.

Consider the vector of velocity tracking errors $\boldsymbol{\xi} \triangleq [\tilde{u}, \tilde{v}]^T$, with $\tilde{u} \triangleq u - u_d, \tilde{v} \triangleq v - v_d$. Furthermore, consider the case where a set of control laws have been designed which ensures that $\boldsymbol{\xi}$ converges asymptotically to the origin when $t \to \infty$. We are now ready to introduce Theorem 1, which states the stability properties of $y_e = 0$.

Theorem 1. *If $\boldsymbol{\xi}$ is bounded and converges asymptotically to the origin as $t \to \infty$, then the guidance law (7.2) will ensure that y_e converges asymptotically to zero as $t \to \infty$. Furthermore, if $\boldsymbol{\xi} = \mathbf{0}$ is a uniformly globally exponentially stable (UGES) equilibrium point, then $y_e = 0$ will by uniformly semi-globally exponentially stable (USGES) and uniformly globally asymptotically stable (UGAS).*

Proof. The dynamic of the crosstrack error is given by [26]

$$\begin{aligned} \dot{y}_e =& -\dot{x}\sin(\gamma_p) + \dot{y}\cos(\gamma_p) \\ =& -\big(u\cos(\psi) - v\sin(\psi)\big)\sin(\gamma_p) \\ &+ \big(u\sin(\psi) + v\cos(\psi)\big)\cos(\gamma_p) \\ =& u\left(\sin(\psi)\cos(\gamma_p) - \cos(\psi)\sin(\gamma_p)\right) \\ &+ v\left(\sin(\psi)\sin(\gamma_p) + \cos(\psi)\cos(\gamma_p)\right) \\ =& (\tilde{u} + u_d)\sin(\psi - \gamma_p) + (\tilde{v} + v_d)\cos(\psi - \gamma_p) \end{aligned} \tag{7.3}$$

This can be written as

$$\begin{aligned} \dot{y}_e =& U_d \sin\left(\psi - \gamma_p + \arctan\left(\frac{v_d}{u_d}\right)\right) \\ &+ \tilde{u}\sin(\psi - \gamma_p) + \tilde{v}\cos(\psi - \gamma_p) \end{aligned} \tag{7.4}$$

Inserting the definition of the desired heading (7.1) into (7.4) and choosing the guidance law according to (7.2) yields

$$\begin{aligned} \dot{y}_e =& U_d \sin\left(\tilde{\psi} + \alpha + \arctan\left(\frac{v_d}{u_d}\right)\right) \\ &+ \tilde{u}\sin(\tilde{\psi} + \alpha) + \tilde{v}\cos(\tilde{\psi} + \alpha) \\ =& U_d \sin\left(-\arctan\left(\frac{y_e}{\Delta}\right)\right) + \tilde{u}\sin(\tilde{\psi} + \alpha) + \tilde{v}\cos(\tilde{\psi} + \alpha) \\ =& -\frac{U_d}{\sqrt{\Delta^2 + y_e^2}} y_e + \tilde{u}\sin(\tilde{\psi} + \alpha) + \tilde{v}\cos(\tilde{\psi} + \alpha) \end{aligned} \tag{7.5}$$

which can be written as

$$\dot{y}_e = f_1(t, y_e) + \boldsymbol{g}(t, \tilde{\psi})\boldsymbol{\xi} \tag{7.6}$$

where

$$f_1(t, y_e) \triangleq -\frac{U_d}{\sqrt{\Delta^2 + y_e^2}} y_e \tag{7.7}$$

$$\boldsymbol{g}(t,\tilde{\psi}) \triangleq \begin{bmatrix} \sin(\tilde{\psi}+\alpha) \\ \cos(\tilde{\psi}+\alpha) \end{bmatrix}^T \tag{7.8}$$

This can be seen as a cascaded system where the nominal system

$$\dot{y}_e = f_1(t, y_e) \tag{7.9}$$

is perturbed by the error dynamics through the term $\boldsymbol{g}(t,\tilde{\psi})\boldsymbol{\xi}$.

Lemma 1. The origin of the nominal system (7.9) is uniformly globally asymptotically stable (UGAS) and uniformly semi-globally exponentially stable (USGES).

Proof. The proof is given in [26]. □

It now remains the analyze the interconnected system (7.6). Since $\boldsymbol{\xi}$ is bounded, it is trivial to see that the perpetuating term $\boldsymbol{g}(t,\tilde{\psi})\boldsymbol{\xi}$ is bounded. Then, since $\boldsymbol{\xi}$ is a vanishing perturbation, ie. $\boldsymbol{\xi} \to \mathbf{0}$ asymptotically as $t \to \infty$, the crosstrack error y_e converges asymptotically to zero [59]. Furthermore, if $\boldsymbol{\xi} = \mathbf{0}$ is UGES, then $y_e = 0$ is USGES and UGAS by Proposition 2.3 in [40]. □

Notice that Theorem 1 is valid for both straight and continuously curved paths, and for disturbances as long as they are within the tracking capabilities of the velocity controllers. This include disturbances in the form of slowly-varying induced wave forces or (potentially non-constant, rotational) currents. Furthermore, tracking of u_d, v_d implies tracking of U_d as $\sqrt{u_d^2 + v_d^2} = U_d$.

Guidance Law with Relative Velocities and Integral Action

For path following with desired heading normal to the path and with only the relative velocity $[u_r, v_r]^T$ available as measurements, the guidance law can be extended to include integral action according to

$$\begin{aligned} u_{rd} &= U_{rd}\cos\left(-\tilde{\psi} \pm \frac{\pi}{2} - \arctan\left(\frac{y_e + \sigma y_{\text{int}}}{\Delta}\right)\right) \\ v_{rd} &= U_{rd}\sin\left(-\tilde{\psi} \pm \frac{\pi}{2} - \arctan\left(\frac{y_e + \sigma y_{\text{int}}}{\Delta}\right)\right) \\ \dot{y}_{\text{int}} &= \frac{\Delta y_e}{\Delta^2 + (y_e + \sigma y_{\text{int}})^2} \end{aligned} \tag{7.10}$$

where σ is a positive constant and $U_{rd} > 0$ is the desired speed. The sign in front of $\pi/2$ should be positive for starboard path following, negative for port path following. The stability properties of the guidance law (7.10) is given in Theorem 2.

Theorem 2. *If $\boldsymbol{\xi} = \mathbf{0}$ is an uniformly globally asymptotically stable (UGAS) equilibrium point, then the guidance law (7.10) yields uniformly globally asymptotically stable (UGAS) and uniform local exponential stability (ULES) properties for the crosstrack-error in the case of straight line path-following in the presence of a constant, irrotational current.*

A proof for Theorem 2 is given in Appendix A.

For a static net pen, the DVL measures absolute velocities u, v, w. Therefore, the guidance law utilized in simulations is given by (7.2).

7.2 Crosstrack Error with Feedforward

The crosstrack error is given as

$$y_e(t) = d_{b/net}(t) - d_d \tag{7.11}$$

where d_d is the desired distance to the net.

However, when calculating the crosstrack error, it is possible to also include the approximated future net pen normal angle ψ_f in order to make to ROV more reactive to sharp turns.

Let the modified crosstrack error be given by

$$y_e(t) = d_{b/net}(t) - d_d + \rho \sin\big(\psi_d(t) - \psi_f(t)\big) \tag{7.12}$$

where $\rho > 0$ is a design parameter. The sinus term will mimic a feed forward term. From Figure 7.1, one can see how the sinus term relates to the look-ahead distance. If the net turns inwards, the sinus term will make the look-ahead distance shorter, thus making the ROV more reactive to turns. If the net turns outwards, the opposite will happen.

From Figure 7.1, it is also clear that the parameters ρ must be chosen according to

$$0 \leq \rho \leq \Delta \tag{7.13}$$

such that $|\rho \sin(\psi_d - \psi_f)| \leq \Delta$. This ensures that the lookahead distance is still ahead of the ROV. Setting $\rho = 0$ will cancel the feedforward term in the crosstrack error.

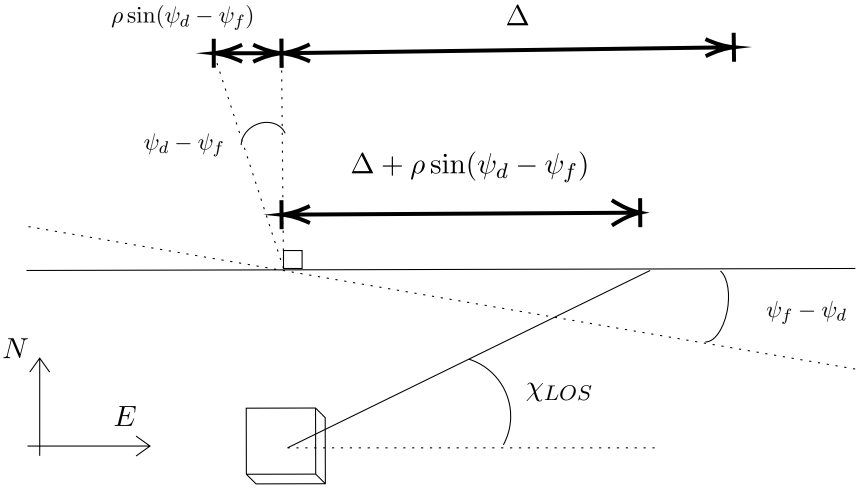

Figure 7.1: Geometric interpretation of the LOS guidance law with feed forward from approximated future plane.

7.3 Tracking Supervisor and Speed Reduction

It should be noted that if the ROV moves with a faster speed, it will be more likely to react too late to edges in the net pen. This is partly due to the fact that this can entail reference changes outside of the bandwidth of the speed controllers and, consequently, the

ROV is incapable of following the desired course angle. Hence, over- or undershoots in crosstrack error might increase. To counter this, a method which monitors the tracking error and calculates a speed reduction function is proposed. The method is inspired by the work in [18].

Consider the tracking error vector $\boldsymbol{e} = [y_e, \tilde{u}, \tilde{v}]$. Let the weighted tracking error be given by $e = \sqrt{\boldsymbol{e^T Q e}}$, where $\boldsymbol{Q} \in \mathbb{R}^3$ is a diagonal weighting matrix with elements $q_i \geq 0$.

The speed reduction function $\Gamma \in [0, 1]$ can now be calculated as

$$\Gamma = \begin{cases} 1, & e < e_{\text{tol}} \\ \frac{1}{e_{\text{max}} - e_{\text{tol}}}(e_{\text{max}} - e), & e_{tol} \leq e \leq e_{\text{max}} \\ 0, & e > e_{\text{max}} \end{cases} \tag{7.14}$$

where $e_{\text{tol}} > 0$ and $e_{\text{max}} > e_{\text{tol}}$ are the tolerance error and maximum error respectively.

This speed function can now be utilized by the guidance system by letting the input to the guidance system be the product of U_d and Γ, see Figure 7.2. The desired speed of the vehicle will be lower if the tracking error is big, with the aim of making the control system more robust to turns and corners.

The speed reduction formula can also be considered a very simple collision avoidance algorithm. By setting e_{max} in a way such that $e < e_{\text{max}}$ implies that the ROV is within a specific safe distance $d_{\text{safe}} = d_d - d_{\text{min}}$ from the net, the commanded speed U_d will be zero if the ROV is closer than d_{safe}.

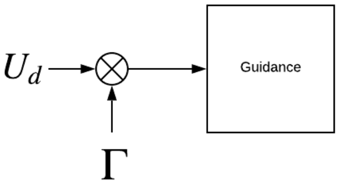

Figure 7.2: Signal flow with speed reduction function.

Chapter 8

Control System

This chapter proposes different state controllers used during simulations and trials. The controlled states are heading ψ, depth z and velocities u, v.

8.1 PID Controllers

In practical experiments and some of the simulations, variations of PID control is used. This is partly because of the simplicity and familiarity of the control designs, but also because of their independence of the vessel model.

Heading Control

The heading control law is given by

$$\tau_r = -k_p\tilde{\psi} - k_i \int_0^t \tilde{\psi}(\tau)d\tau - k_d\dot{\tilde{\psi}} + \ddot{\psi}_d \tag{8.1}$$

where $k_p, k_i, k_d > 0$ are design parameters. This is recognized as PID control.

Depth Control

The depth control law is given by

$$\tau_w = -k_p\tilde{z} - k_i \int_0^t \tilde{z}(\tau)d\tau \tag{8.2}$$

where $k_p, k_i > 0$. This is a PI controller.

Velocity Control

The velocity control laws are given by

$$\begin{aligned} \tau_u &= -k_{p_u}\tilde{u} - k_{i_u} \int_0^t \tilde{u}(\tau)d\tau + \dot{u}_d \\ \tau_v &= -k_{p_v}\tilde{v} - k_{i_v} \int_0^t \tilde{v}(\tau)d\tau + \dot{v}_d \end{aligned} \tag{8.3}$$

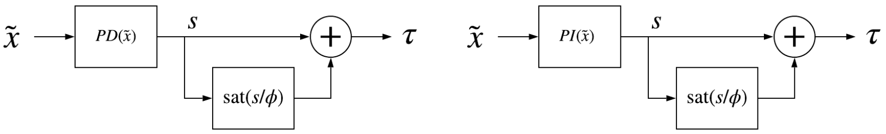

(a) Block diagram of 1st order sliding mode plus PD control.

(b) Block diagram of 1st order sliding mode plus PI control.

Figure 8.1: Block diagram of 1st order sliding mode controllers.

where $k_{p_u}, k_{p_v}, k_{i_u}, k_{i_v}$ are positive control parameters. This is PI control.

8.2 First-order Sliding Mode Controllers

A set of first-order sliding mode controllers have also been designed for this thesis, and used in parts of the simulations. The heading and depth controllers follow the suggestion in [1]. When inspecting the control law, it is clear that these controllers could be viewed as PD-controllers plus PD-controllers followed by a saturation function, see Figure 8.1a.

For velocity control, measurements and references for $[\tilde{x}, \tilde{y}]^T$ are unavailable. Instead, integral action have been added to the sliding variable. The velocity control laws could be interpreted as a PI-controller plus a PI-controller followed by a saturation-function, see Figure 8.1b.

As the practical implementation of the suggested control laws utilizes the continuous high-slope saturation function as a replacement for the ideal signum function, one can only ensure that the sliding variable will converge to the boundary layer. However, the integral action in velocity control will ensure the velocity tracking errors converges to their origins inside of the boundary layer. This will be demonstrated in simulations.

Heading Control

Let the sliding surface be given by

$$s_\psi = -\lambda_\psi \tilde{\psi} - \tilde{r} \tag{8.4}$$

where $\lambda_\psi > 0$. Then let the heading control law be given by

$$\tau_r = k_\psi s_\psi + k_{s_\psi} \text{sat}(s_\psi / \phi_\psi) \tag{8.5}$$

where $k_\psi, k_{s_\psi} > 0$ and $\phi_\psi > 0$ is the boundary layer thickness.

Depth Control

Let the sliding surface be given by

$$s_z = -\lambda_z \tilde{z} - \tilde{w} \tag{8.6}$$

where $\lambda_z > 0$. Then let the heading control law be given by

$$\tau_w = k_z s_z + k_{s_z} \text{sat}(s_z / \phi_z) + \hat{g}_z \tag{8.7}$$

where $k_z, k_{s_z} > 0$ are constant gains, $\phi_z > 0$ the boundary layer thickness and $\hat{g}_z$ is an estimation of restoring forces in the z-axis.

Velocity Control with Integral Action

For velocity control with integral action, let the sliding surfaces be given by

$$\begin{aligned} s_u &= -\lambda_u \int_0^t \tilde{u}(\tau)d\tau - \tilde{u}(t) \\ s_v &= -\lambda_v \int_0^t \tilde{v}(\tau)d\tau - \tilde{v}(t) \end{aligned} \tag{8.8}$$

with the control laws given by

$$\begin{aligned} \tau_u &= k_u s_u + k_{s_u} \text{sat}(s_u/\phi_u) \\ \tau_v &= k_v s_v + k_{s_v} \text{sat}(s_v/\phi_v) \end{aligned} \tag{8.9}$$

Here $k_u, k_v, k_{s_u}, k_{s_v}, \lambda_u, \lambda_v$ are positive constants and $\phi_u > 0, \phi_v > 0$ are the thickness of the boundary layers.

8.2.1 Stability Analysis

The control laws presented in (8.5)-(8.9) can be analyzed when the continuous saturation function $\text{sat}(s/\phi)$ is replaced by the ideal signum function $\text{sgn}(s)$.

Consider the 4DOF maneuvering model given by

$$\begin{aligned} \dot{\boldsymbol{\eta}} &= \boldsymbol{J}_\psi(\psi)\boldsymbol{\nu} \\ \boldsymbol{M}\dot{\boldsymbol{\nu}} &= -\boldsymbol{D}\boldsymbol{\nu} - \boldsymbol{C}(\boldsymbol{\nu})\boldsymbol{\nu} - \boldsymbol{g} + \boldsymbol{\Phi}\boldsymbol{\theta} + \boldsymbol{\tau} \end{aligned} \tag{8.10}$$

where it is assumed for simplicity that the damping is linear and the motion in roll and pitch can be neglected. Furthermore, let the inertia matrix, added mass matrix and damping matrix be given by

$$\boldsymbol{M} = \begin{bmatrix} m_{11} & 0 & 0 & 0 \\ 0 & m_{22} & 0 & 0 \\ 0 & 0 & m_{33} & 0 \\ 0 & 0 & 0 & m_{44} \end{bmatrix}, \boldsymbol{M}_A = \begin{bmatrix} m_{11}^A & 0 & 0 & 0 \\ 0 & m_{22}^A & 0 & 0 \\ 0 & 0 & m_{33}^A & 0 \\ 0 & 0 & 0 & m_{44}^A \end{bmatrix} \tag{8.11}$$

$$\boldsymbol{D} = \begin{bmatrix} d_{11} & 0 & 0 & 0 \\ 0 & d_{22} & 0 & 0 \\ 0 & 0 & d_{33} & 0 \\ 0 & 0 & 0 & d_{44} \end{bmatrix} \tag{8.12}$$

It is further assumed that the velocity $\boldsymbol{\nu}$ of the vehicle is bounded. This is a mild assumption, as the ROV is a mechanical system.

Assume the vehicle is under the influence of a constant, irrotational current with velocity vector $\boldsymbol{V}_c = [V_x, V_y, 0, 0]^T$ in $\{n\}$. The time derivative of the current speed in the body-fixed coordinate frame is

$$\dot{\boldsymbol{\nu}}_c = \frac{d}{dt}(\boldsymbol{J}_\psi^T(\psi)\boldsymbol{V}_c) = [rv_c, -ru_c, 0, 0]^T \tag{8.13}$$

Furthermore, let the vector $\boldsymbol{\theta} \triangleq [V_x, V_y, V_x V_y, V_x^2, V_y^2]^T$ and matrix $\boldsymbol{\Phi}$ gather the current induced forces, where

$$\boldsymbol{\Phi} = \begin{bmatrix} \boldsymbol{\phi}_u(\psi, r)^T & \boldsymbol{\phi}_v(\psi, r)^T & \mathbf{0}_{1x4} & \boldsymbol{\phi}_r(u, v, \psi)^T \end{bmatrix}^T \tag{8.14}$$

with

$$\boldsymbol{\phi}_u(\psi, r) = \begin{bmatrix} \frac{d_{11}}{m_{11}} \cos\psi - \frac{m_{11}^A - m_{22}^A}{m_{11}} r \sin\psi \\ \frac{d_{11}}{m_{11}} \sin\psi + \frac{m_{11}^A - m_{22}^A}{m_{11}} r \cos\psi \\ 0 \\ 0 \\ 0 \end{bmatrix} \tag{8.15}$$

$$\boldsymbol{\phi}_u(\psi, r) = \begin{bmatrix} -\frac{d_{22}}{m_{22}} \sin\psi - \frac{m_{11}^A - m_{22}^A}{m_{22}} r \cos\psi \\ \frac{d_{22}}{m_{22}} \cos\psi - \frac{m_{11}^A - m_{22}^A}{m_{22}} r \sin\psi \\ 0 \\ 0 \\ 0 \end{bmatrix} \tag{8.16}$$

and

$$\boldsymbol{\phi}_r(u, v, \psi) = \frac{m_{11}^A - m_{22}^A}{m_{33}} \begin{bmatrix} u \sin\psi - v \cos\psi \\ -u \cos\psi - v \sin\psi \\ -\cos\psi \sin\psi \\ \cos\psi \sin\psi \\ 1 - 2\sin^2\psi \end{bmatrix} \tag{8.17}$$

Define the vectors

$$\begin{aligned} \boldsymbol{x}_1 &= \begin{bmatrix} \int_0^t \tilde{u}(t) d\tau & \int_0^t \tilde{v}(t) d\tau & \tilde{z} & \tilde{\psi} \end{bmatrix}^T \\ \boldsymbol{x}_2 &= \begin{bmatrix} \tilde{u} & \tilde{v} & \dot{\tilde{z}} & \dot{\tilde{\psi}} \end{bmatrix}^T \end{aligned} \tag{8.18}$$

and the sliding manifold

$$\boldsymbol{s} = -\boldsymbol{\Lambda} \boldsymbol{x}_1 - \boldsymbol{x}_2 \tag{8.19}$$

with $\boldsymbol{\Lambda} = \boldsymbol{\Lambda}^T > 0$. Furthermore, let $\boldsymbol{K}_d, \boldsymbol{K}_s$ be positive definite matrices of control gains and $\text{sgn}(\boldsymbol{x})$ be the vector function whose i-th component is

$$\text{sgn}(\boldsymbol{x})_i = \begin{cases} 1 & x_i > 0 \\ 0 & x_1 = 0 \\ -1 & x_i < 0 \end{cases} \tag{8.20}$$

Let the control law be given as

$$\boldsymbol{\tau} = \boldsymbol{K}_d \boldsymbol{s} + \boldsymbol{K}_s \text{sgn}(\boldsymbol{s}) + \hat{\boldsymbol{g}} \tag{8.21}$$

where $\hat{\boldsymbol{g}}$ is an estimate of the restoring forces vector $\boldsymbol{g}$.

Finally, define the vector of tracking errors $\boldsymbol{\zeta} = [\tilde{u}, \tilde{v}, \tilde{z}, \tilde{\psi}]^T$

Theorem 3. *Consider a underwater vehicle, whose dynamics is described by (8.10). The control law (8.21) ensures that the tracking errors $\boldsymbol{\zeta} = \mathbf{0}$ is a uniformly globally exponentially stable (UGES) equilibrium point.*

Proof. Consider the radially unbounded, positive definite Lyapunov function candidate $V_1 = 1/2\boldsymbol{s}^T\boldsymbol{M}\boldsymbol{s}$. The time derivative is

$$\begin{aligned}
\dot{V}_1 &= \boldsymbol{s}^T\boldsymbol{M}\dot{\boldsymbol{s}} = \boldsymbol{s}^T\boldsymbol{M}(-\boldsymbol{\Lambda}\boldsymbol{x}_2 - \dot{\boldsymbol{\nu}} + \dot{\boldsymbol{\nu}}_d) \\
&= \boldsymbol{s}^T(-\boldsymbol{M}\boldsymbol{\Lambda}\boldsymbol{x}_2 + \boldsymbol{D}\boldsymbol{\nu} + \boldsymbol{C}(\boldsymbol{\nu})\boldsymbol{\nu} + \boldsymbol{g} - \boldsymbol{\Phi}\boldsymbol{\theta} - \boldsymbol{\tau} + \boldsymbol{M}\dot{\boldsymbol{\nu}}_d) \\
&= -\boldsymbol{s}^T\boldsymbol{K}_d\boldsymbol{s} - \boldsymbol{K}_s||\boldsymbol{s}|| + \boldsymbol{s}^T\underbrace{(-\boldsymbol{M}\boldsymbol{\Lambda}\boldsymbol{x}_2 + \boldsymbol{D}\boldsymbol{\nu} + \boldsymbol{C}(\boldsymbol{\nu})\boldsymbol{\nu} + \tilde{\boldsymbol{g}} - \boldsymbol{\Phi}\boldsymbol{\theta} + \boldsymbol{M}\dot{\boldsymbol{\nu}}_d)}_{\boldsymbol{y}} \qquad (8.22) \\
&\leq -\lambda_{\min}(\boldsymbol{K}_d)||\boldsymbol{s}||^2 - \lambda_{\min}(\boldsymbol{K}_s)||\boldsymbol{s}|| + ||\boldsymbol{s}||\ ||\boldsymbol{y}||
\end{aligned}$$

The time derivative (8.22) becomes negative definite by choosing

$$\lambda_{\min}(\boldsymbol{K}_s) \geq ||\boldsymbol{y}|| \qquad (8.23)$$

To be able to chose this, $\boldsymbol{y}$ has to be bounded. Since the veloicty $\boldsymbol{\nu}$ is bounded, $\boldsymbol{D}\boldsymbol{\nu}, \boldsymbol{C}(\boldsymbol{\nu})\boldsymbol{\nu}, \boldsymbol{\Phi}\boldsymbol{\theta}$ will be bounded by definition. Furthermore, $\tilde{\boldsymbol{g}}$ is bounded, as $\hat{\boldsymbol{g}}$ is constant. The reference signals $\boldsymbol{\nu}_d, \dot{\boldsymbol{\nu}}_d$ can be bounded by design. Finally, this implies the boundedness of $\boldsymbol{x}_2$ be definition.

By Theorem 4.10 in [32], the origin of the sliding manifold $\boldsymbol{s}$ is therefore UGES.

Furthermore, consider the positive definite, radially unbounded Lyapunov function candidate $V_2 = 1/2||\boldsymbol{x}_1||^2$. The time derivative of V_2 on $\boldsymbol{s} = 0$ is

$$\dot{V}_2 = \boldsymbol{x}_1^T\dot{\boldsymbol{x}}_1 = \boldsymbol{x}_1^T\boldsymbol{x}_2 = -\boldsymbol{x}_1^T\boldsymbol{\Lambda}\boldsymbol{x}_1 < 0, \qquad (8.24)$$

which suggest that the origin of $\boldsymbol{x}_1$ on $\boldsymbol{s} = 0$ is UGES by Theorem 4.10 in [32]. When $s = 0$ and $\boldsymbol{x}_1 = \boldsymbol{0}$, then we also have $\boldsymbol{x}_2 = \boldsymbol{0}$ by definition. Consequently, $\boldsymbol{\zeta} = \boldsymbol{0}$ is UGES.

□

Remark 3. Theorem 3 is only valid with the ideal signum function. For the high-slope saturation function, this stability analysis is only able to conclude that $||\boldsymbol{s}|| < \theta$, where $\theta > 0$ is the boundary thickness. Stability within the boundary layer will be studied in simulations.

8.3 Super-Twisting Algorithm with Adaptive Gains

Finally, following the theory from [56], a set of super-twisting algorithm (STA) sliding mode controllers with adaptive gains is proposed.

The control law is given by

$$\begin{aligned}
\tau &= -\alpha|s|^{1/2}\text{sgn}(s) + v \\
\dot{v} &= -\beta\text{sgn}(s)
\end{aligned} \qquad (8.25)$$

Here, α, β are adaptive gains and s the sliding surface. The adaptive law are given by

$$\dot{\alpha} = \begin{cases} \omega\sqrt{\frac{\gamma}{2}}, & |s| > \alpha_m \\ 0, & |s| \leq \alpha_m \end{cases} \qquad (8.26)$$

$$\beta = 2\varepsilon\alpha + \lambda + 4\varepsilon^2 \qquad (8.27)$$

where $\varepsilon.\lambda, \omega, \gamma$ are arbitrary positive constants.

The sliding variables are given by

$$\begin{aligned} s_\psi &= \tilde{\psi} + \dot{\tilde{\psi}} \\ s_z &= \tilde{z} + \dot{\tilde{z}} \\ s_u &= \tilde{u} \\ s_v &= \tilde{v} \end{aligned} \tag{8.28}$$

Clearly, s_u, s_v are not true sliding surfaces, as they are simply the tracking errors. This is because the errors in position and acceleration are unavailable for feedback. The control task is therefore to control the tracking errors directly. This may be problematic with respect to robustness or implementation, and will be further analyzed through simulations.

Part IV

Results

Chapter 9

ROV Model and Simulation Setup

This chapter will present a model for Argus Mini, the 6DOF ROV used in simulations and experiments. Furthermore it will introduce tools and setups used during simulations.

9.1 ROV Model

The dimensions of the ROV are $[0.9\text{m}, 0.65\text{m}, 0.5\text{m}]^T$. It is assumed that the vehicle is symmetric in port/starboard, fore/aft and top/bottom, and that the CO is placed in the CG.

The rigid body mass of the model is given as

$$\boldsymbol{M}_{RB} = \begin{bmatrix} 90 & 0 & 0 & 0 & 0 & 0 \\ 0 & 90 & 0 & 0 & 0 & 0 \\ 0 & 0 & 90 & 0 & 0 & 0 \\ 0 & 0 & 0 & 10 & 0 & 0 \\ 0 & 0 & 0 & 0 & 15 & 0 \\ 0 & 0 & 0 & 0 & 0 & 13 \end{bmatrix} \tag{9.1}$$

while the zero-frequency added mass matrix is given by

$$\boldsymbol{M}_{A} = \begin{bmatrix} 54 & 0 & 0 & 0 & 0 & 0 \\ 0 & 72 & 0 & 0 & 0 & 0 \\ 0 & 0 & 360 & 0 & 0 & 0 \\ 0 & 0 & 0 & 11 & 0 & 0 \\ 0 & 0 & 0 & 0 & 43.5 & 0 \\ 0 & 0 & 0 & 0 & 0 & 5.2 \end{bmatrix} \tag{9.2}$$

and the mass matrix is given by $\boldsymbol{M} = \boldsymbol{M}_{RB} + \boldsymbol{M}_A$.

The Coriolis and centripetal matrix can then be calculated to

$$\boldsymbol{C}(\boldsymbol{\nu}_r) = \begin{bmatrix} 0 & 0 & 0 & 0 & 450w_r & -162v_r \\ 0 & 0 & 0 & -450w_r & 0 & 144u_r \\ 0 & 0 & 0 & 162v_r & -144u_r & 0 \\ 0 & 450w_r & -162v_r & 0 & 18.2r & -66.5q \\ -450w_r & 0 & 144u_r & -18.2r & 0 & 21p \\ 162v_r & -144u_r & 0 & 66.5q & -21p & 0 \end{bmatrix} \tag{9.3}$$

Figure 9.1: Argus Mini (courtesy of Argus Remote Systems AS).

The damping matrix $\boldsymbol{D}(\boldsymbol{\nu_r})$ is split into a linear part $\boldsymbol{D}$ and a nonlinear part $\boldsymbol{D}_n(\boldsymbol{\nu_r})$. The linear damping matrix is given as

$$\boldsymbol{D} = \begin{bmatrix} 250 & 0 & 0 & 0 & 0 & 0 \\ 0 & 200 & 0 & 0 & 0 & 0 \\ 0 & 0 & 175 & 0 & 0 & 0 \\ 0 & 0 & 0 & 20 & 0 & 0 \\ 0 & 0 & 0 & 0 & 20 & 0 \\ 0 & 0 & 0 & 0 & 0 & 15 \end{bmatrix} \tag{9.4}$$

while its nonlinear counterpart is given by

$$\boldsymbol{D}_n(\boldsymbol{\nu_r}) = \begin{bmatrix} 350|u_r| & 0 & 0 & 0 & 0 & 0 \\ 0 & 350|v_r| & 0 & 0 & 0 & 0 \\ 0 & 0 & 400|w_r| & 0 & 0 & 0 \\ 0 & 0 & 0 & 100|p| & 0 & 0 \\ 0 & 0 & 0 & 0 & 100|q| & 0 \\ 0 & 0 & 0 & 0 & 0 & 75|r| \end{bmatrix} \tag{9.5}$$

The damping matrix is given by $\boldsymbol{D}(\boldsymbol{\nu_r}) = \boldsymbol{D} + \boldsymbol{D}_n(\boldsymbol{\nu}_r)$.

Furthermore, the CB is located at $\boldsymbol{o}_b^b = [0, 0, -0.18]^T$, so that the distance between the centre of gravity and centre of buoyancy is given by the vector $\overline{BG} = [\overline{BG}_x, \overline{BG}_y, \overline{BG}_z] = [0, 0, 0.18]^T$.

The weight of the submerged body is given by $W = g{*}m$, where g is the gravity acceleration and $m = 90$kg is the mass of the vehicle. The ratio between the weight and the buoyancy forces B is given as $W/B = 0.99$. Thus the restoring forces are given by

$$\boldsymbol{g}(\boldsymbol{\eta}) = \begin{bmatrix} (W-B)\sin(\theta) \\ -(W-B)\cos(\theta)\sin(\phi) \\ -(W-B)\cos(\theta)\cos(\phi) \\ \overline{BG}_z\cos(\theta)\sin(\phi) \\ \overline{BG}_z\sin(\theta) \\ 0 \end{bmatrix} \approx \begin{bmatrix} -0.91\sin(\theta) \\ 0.91\cos(\theta)\sin(\phi) \\ 0.91\cos(\theta)\cos(\phi) \\ 0.18\cos(\theta)\sin(\phi) \\ 0.18\sin(\theta) \\ 0 \end{bmatrix} \tag{9.6}$$

9.1.1 Sensors

The Argus Mini is equipped with 5 kind of sensors: A HD camera, a fluxgate compass, a depth sensor, a gyro and a Nortek DVL 1000 model. The ROV contains no sensors for direct measurement of position or acceleration.

The DVL system is attached on the frontal side of the ROV and pointing in the x^b direction. The DVL system consists of 4 beams which is rotated according to figure 6.1 with angles $[\beta_1, \beta_2, \beta_3, \beta_4]^T = [45°, 135°, 225°, 315°]^T$ and $\gamma_i = 25°$ for $i \in \{1, 2, 3, 4\}$. The position of the DVL system with respect to the CO of the ROV is given by $\boldsymbol{p}^b_{dvl/b} = [0.37, -0.2, 0.2]^T$.

9.1.2 Thrusters

The ROV has got 6 actuators. Figure 9.2 shows the thruster configuration. 4 of the thrusters works in the horizontal plane and is rotated ±35° around x^b. The remaining two thrusters work in heave and is directed in the z^b direction. The thruster allocation matrix $\boldsymbol{B}$ and thruster vector $\boldsymbol{f}$ is given by Eq. (9.7) and (9.8).

$$\boldsymbol{B} = \begin{bmatrix} \cos(35°) & \cos(-35°) & \cos(-35°) & \cos(35°) & 0 & 0 \\ \sin(35°) & \sin(-35°) & \sin(-35°) & \sin(35°) & 0 & 0 \\ 0 & 0 & 0 & 0 & 1 & 1 \\ 0 & 0 & 0 & 0 & 0 & 0 \\ 0 & 0 & 0 & 0 & 0.216 & -0.216 \\ 0.216\cos(35°) + 0.202\sin(35°) & -0.216\cos(-35°) - 0.202\sin(-35°) & 0.265\cos(-35°) + 0.195\sin(-35°) & -0.265\cos(35°) - 0.195\sin(35°) & 0 & 0 \end{bmatrix} \tag{9.7}$$

$$\boldsymbol{f} = \begin{bmatrix} f_1 & f_2 & f_3 & f_4 & f_5 & f_6 \end{bmatrix}^T \tag{9.8}$$

The measured force of a single thruster relative to the normalized commanded input is shown as points in Figure 9.3, while the solid line is a least-square fit to a quadratic function. This shows that each thruster is able to provide a force of roughly 100 N in each direction. Furthermore, to saturate the first derivative of the thruster force, a rate slew limiter was implemented according to (9.9).

$$y_k = \begin{cases} 1.5(t_k - t_{k-1}) + y_{k-1}, & \frac{u_k - y_{k-1}}{t_k - t_{k-1}} \geq 1.5 \\ -1.5(t_k - t_{k-1}) + y_{k-1}, & \frac{u_k - y_{k-1}}{t_k - t_{k-1}} \leq -1.5 \\ u_k, & \text{else} \end{cases} \tag{9.9}$$

Here t_k is the time at step k, while u_k, y_k are the commanded input and output at step k.

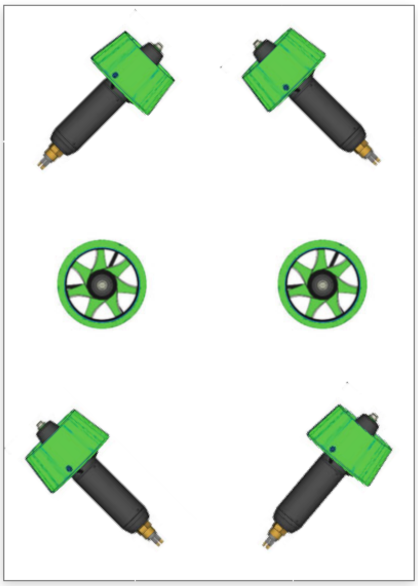

Figure 9.2: Thruster configuration of Argus Mini.

9.2 Environmental Disturbances

In several simulations, the system has been simulated with both waves and currents. The current is constant and irrotational. The waves are generated according to the Airy theory, using the JONSWAP wave spectra. The current speed, significant wave height, wave mean period, as well as directions of the current and wave are stated at each simulation.

As wave loads decreases exponentially with depth [22], the following wave dynamics are introduced

$$\begin{aligned} \boldsymbol{\eta}_{w_d} &= \boldsymbol{\eta}_{w_0} e^{-kz} \\ \boldsymbol{y} &= \boldsymbol{\eta} + \boldsymbol{\eta}_{w_d} \end{aligned} \tag{9.10}$$

where $\boldsymbol{\eta}_{w_0}$ is the wave-frequency motion of the ROV at depth 0, $\boldsymbol{\eta}_{w_d}$ is the wave-frequency motion at depth d, $k = \frac{\omega_0^2}{g} = \frac{2\pi}{\lambda}$ is the wave number, z is the depth, $\boldsymbol{\eta}$ is the ROV low-frequency motion and $\boldsymbol{y}$ is the total motion.

9.3 FhSim

All simulations in the thesis are conducted in FhSim, a SINTEF developed simulation platform for marine systens. This section will provide a very brief introduction of FhSim. For a more rigerous explanation, see [50, 61].

As most time-dependent marine-systems are described by (often nonlinear) ordinary differential equations (ODEs), FhSim is designed especially for solving nonlinear ODEs. FhSim is implemented in C++, and FhSim therefore supports object-oriented programming.

Objects in FhSim are implemented as SimObjects, which may be considered the building blocks of FhSim. Each SimObject is associated with a set of ODEs and at each timesteps,

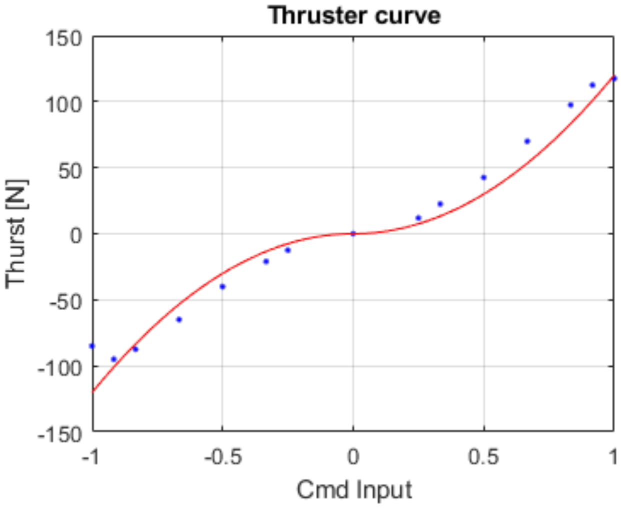

Figure 9.3: Applied force of a single thruster as a function of the normalized commanded input. Fitted to a quadratic model.

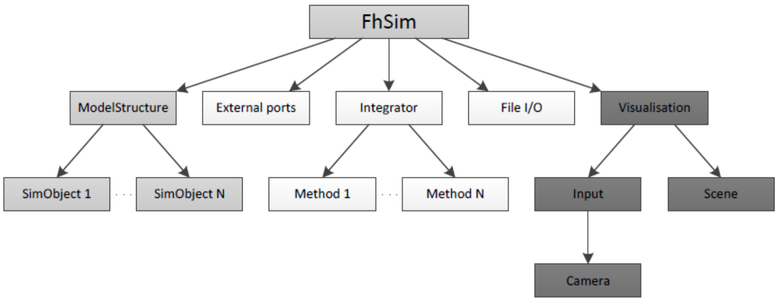

Figure 9.4: Overview of FhSim architecture.

each SimObject transfer its state derivatives to an integrator. At the end of each timestep, the integrator performs an integration of the states based upon a method chosen by the user.

The SimObjects are connected through I/O ports, and the signal flow between the SimObjects are set up in a XML document. Lastly, FhSim can communicate with external devices through a set of external ports. FhSim is therefore not restricted to simulations only, but can be used in realtime hardware applications. Figure 9.4 shows an overview of the architecture of FhSim.

Numerous SimObjects have already been developed unrelated to this thesis, and through the signal flow structure of FhSim, a portion of these SimObjects were widely used during simulations. Among these SimObjects were a 6DOF ROV model, an environmental model, a static net cage structure and a SimObject describing the DVL beams.

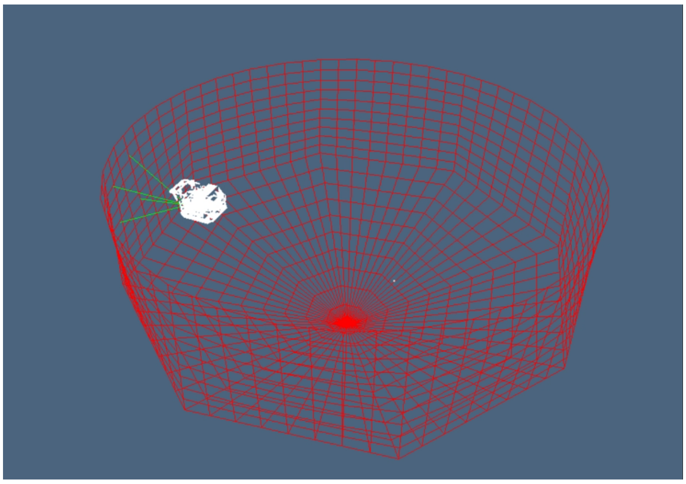

Figure 9.5: Visualization of ROV traversing a net pen in FhSim.

9.3.1 GUI and Visualization

A central element to FhSim is its ability to visualize simulations of systems. For many applications, this can be a helpful tool, and was actively used during the work in this thesis. Figure 9.5 shows an example of the visualization capabilities of FhSim.

Furthermore, a GUI application has been developed which enables the ROV to be controlled by a Xbox remote control, see Figure 9.6. The Xbox controller can be used both in simulations and with the ROV in practical applications, which have been useful in both cases.

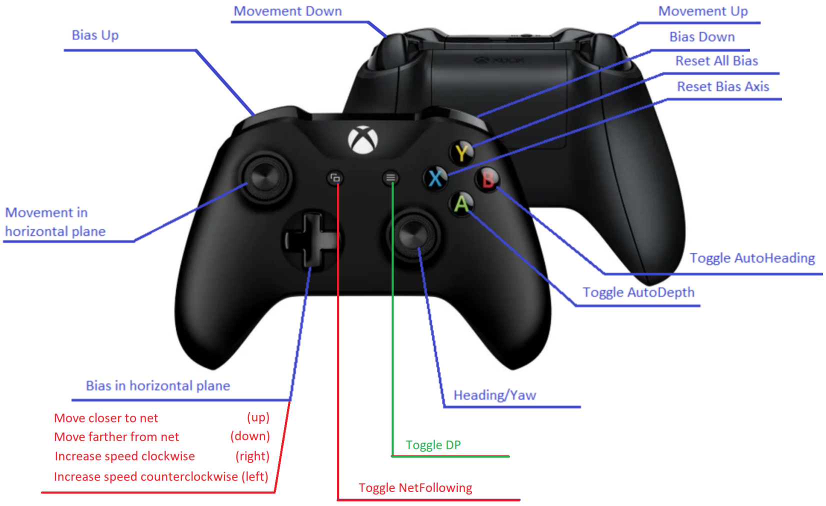

Figure 9.6: Xbox Controller with mapping of buttons

Chapter 10

Simulation Results

This chapter will present and discuss the results from simulations verifying the net approximation methods, guidance laws and control laws given in Part III.

10.1 Net Approximation

Figure 10.1 shows net pen approximation results from simulations. During the simulations, the net pen geometry was approximated as a flat plane with no feedforward ($\rho = 0$), a flat plane with feed forward ($\rho = 1$) and as a curved plane ($\Lambda = 0.25$). The desired distance d_d to the net pen was 3m.

As shown in Figure 10.1a, the estimated crosstrack error is precise. The blue line represent the true crosstrack error between the net pen and the ROV, while the red line represent the estimated crosstrack error when estimated as a flat plane with $\rho = 0$. At the start of the simulations, the ROV is far from the net, while it is moving closer during simulations. As seen in Figure 10.1b, the estimation error is larger when the ROV is further away from the net. When the ROV has converged to the desired distance, the estimation error is less than 7 cm.

Simulations also show that there is small differences between the different estimation methods, as shown in Figure 10.1c. The blue line represent the difference between the crosstrack estimations with $\rho = 0$ and $\rho = 1$, while the red line represent the different between the estimation with $\rho = 0$ and the curved plane estimation. The crosstrack error estimation differences is in the range of millimeters.

The main reason for the small difference of estimations can be seen in Figure 10.1d, which shows the differences between the estimated net pen heading ψ_d and the estimated future net pen heading ψ_f. The differences are minimal. The consequence is that the feed forward element in (7.12) has little impact. For the curved path method proposed in Section 6.6, the three waypoints will approximately be on the same straight line, and the estimated plane will be the same flat plane as the other estimations. It is clear that for the different approximations methods to be distinct, considerations has to be made when calculating ψ_f and ψ_p, eg. developing new methods for weighing the DVL beams.

While the different methods yielded less differences than wanted, the net pen geometry approximation in general does a very satisfying job. For the remainder of the simulations,

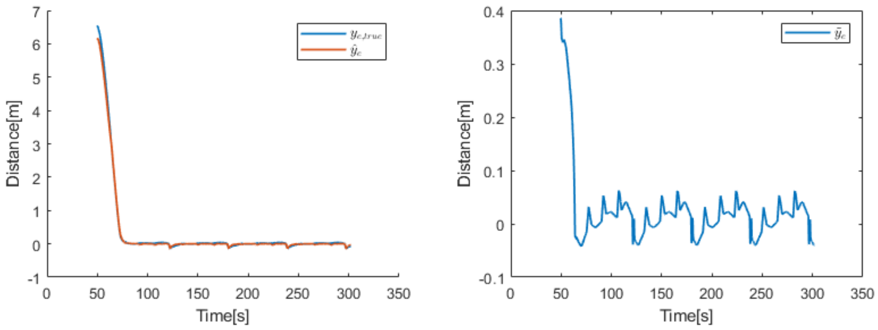

(a) True and estimated crosstrack error (b) Crosstrack estimation error

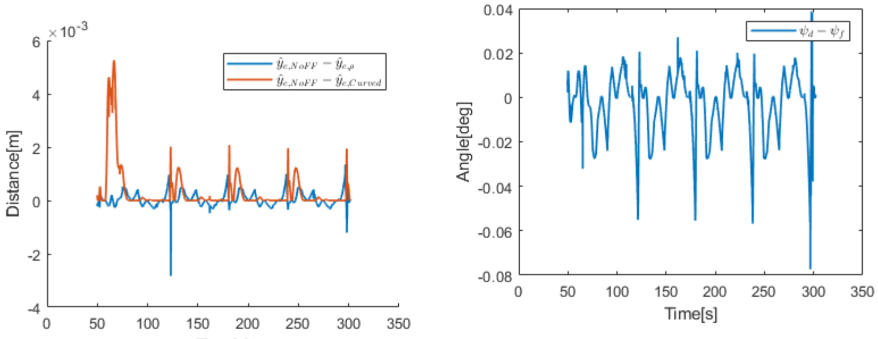

(c) Differences in estimations of crosstrack

(d) Difference between estimated net heading and estimated net future heading

Figure 10.1: Net pen geometry approximation

the net pen is approximated as a flat plane with no feedforward ($\rho = 0$).

10.2 Guidance Law

This section will present simulations verifying the guidance law (7.2). In the first set of simulations, the ROV is commanded to travel along the x^n axis with desired heading $\psi_d = -\pi/2$. In the second set of simulations, the goal is for the ROV to follow a predetermined path generated from waypoints $\boldsymbol{p}_0 = [0,0]^T, \boldsymbol{p}_1 = [25,-25]^T, \boldsymbol{p}_2 = [50,0]^T$. The third set of simulations demonstrates the performance with the speed reduction formula.

During these simulations, the controls for tracking of vehicle states were the 1st order sliding mode controllers given in Section 8.2. Further discussion on the control laws and their parameter tunings is given in Section 10.3.

10.2.1 Path Following

Straight line path following without environmental disturbances

Figure 10.2 shows the performance of the guidance law (7.2) for straight path following without environmental disturbances. As the figures shows, the performance of the guidance law is satisfying. The crosstrack error is minimized, while still maintaining a fixed heading normal to the path.

Straight line path following with ocean current

Figure 10.3 shows simulation of straight line path following in the presence of a constant, irrotational current. The current velocity vector in $\{n\}$ is given by $[V_x, V_y, V_z]^T = [0, 0.35 \text{ m/s}, 0]^T$. As seen, the ROV successfully manages to follow the path. By applying thruster forces τ_u in surge, the current is successfully countered, as seen in Figure 10.3d.

Straight line path following with waves and current

As Figure 10.4 shows, the guidance law is also robust to time-varying disturbances, as long as they aren't faster than what the velocity controllers can handle. During this simulation, the system was simulated with a constant, irrotational current with $[V_x, V_y, V_z]^T = [0, 0.35 \text{ m/s}, 0]^T$, as well as waves with long wave-lengths. The waves are generated with significant wave height $H_s = 1$m, mean wave period $T_p = 16$s and direction $\beta_w = \pi/2$. The wave frequency is left unfiltered. The simulations were conducted at a depth of 2m.

As seen in Figure 10.4d, the waves lead to an oscillatory motion at the thrusters. Still, Figure 10.4b shows that the velocity controllers are almost able to track the references. Finally, Figure 10.4a shows that the crosstrack error successfully converges to the origin.

Curved line path following

The guidance law also works for curved paths, as seen in Figure 10.5. Figure 10.5 shows the case with a constant, irrotational current with $[V_x, V_y, V_z]^T = [0, 0.35 \text{ m/s}, 0]^T$. Again, by applying thruster forces with opposite direction to the current, the crosstrack error is minimized while still maintaining a fixed heading.

10.2.2 Speed Reduction Function

An example of the effect of the speed reduction formula is seen in Figure 10.6. Here, the plots is showing the ROV trying to follow the net at a corner. Because of the sharp turn, the ROV is unable to follow the desired crosstrack distance. The speed reduction then kicks in and the desired speed U_d is lowered. The desired speed is $U_d = 0.3$ m/s, $e_{tol} = 0.05, e_{max} = 1$ and $\boldsymbol{Q} = \boldsymbol{I}_{3x3}$

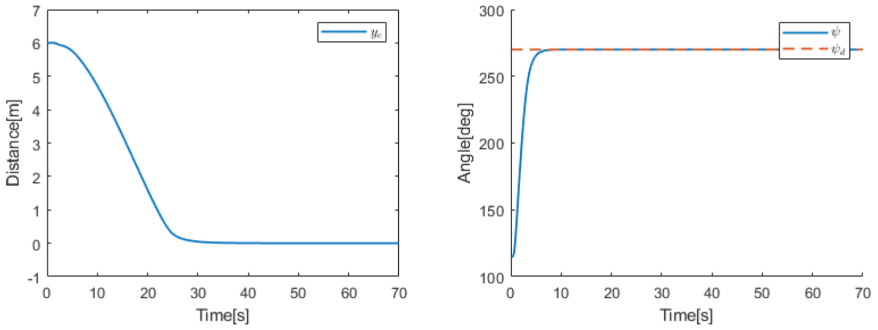

(a) Crosstrack error (b) Heading tracking

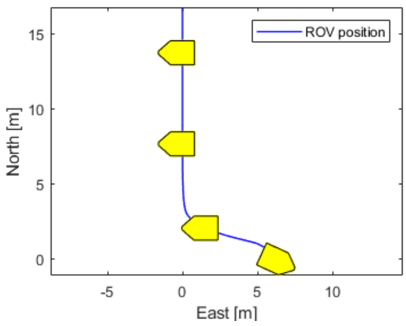

(c) Position of ROV in north-east plane.

Figure 10.2: Straight line path following without environmental disturbances

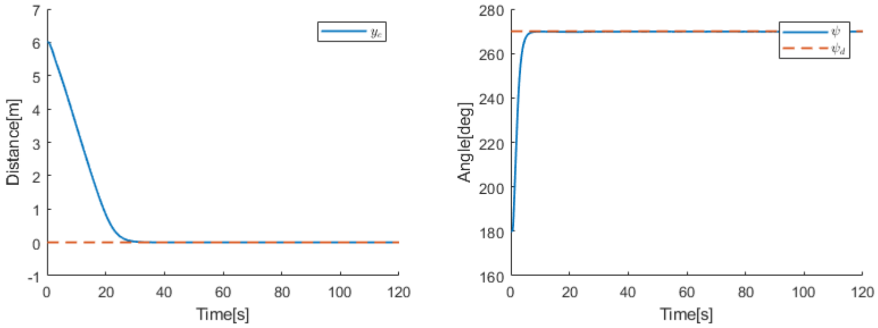

(a) Crosstrack error (b) Heading tracking

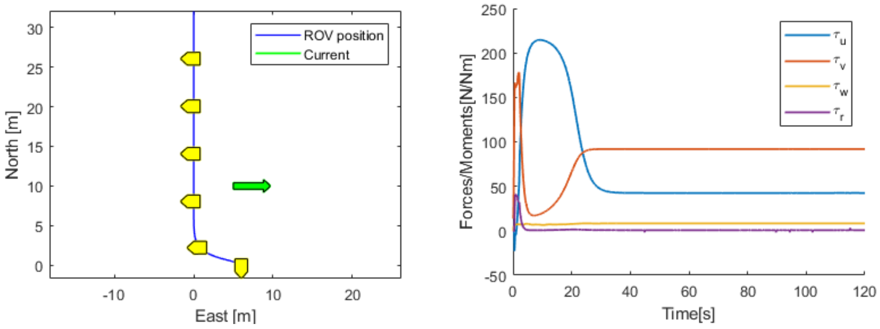

(c) Position of ROV in north-east plane. (d) Thruster forces and moments.

Figure 10.3: Straight line path following with constant, irrotational current

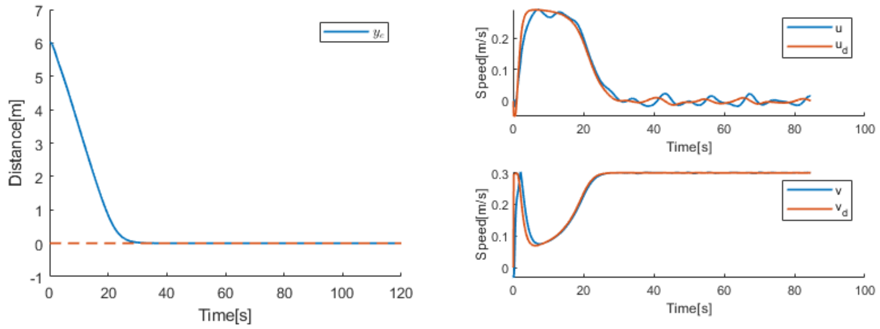

(a) Crosstrack error (b) Velocity tracking

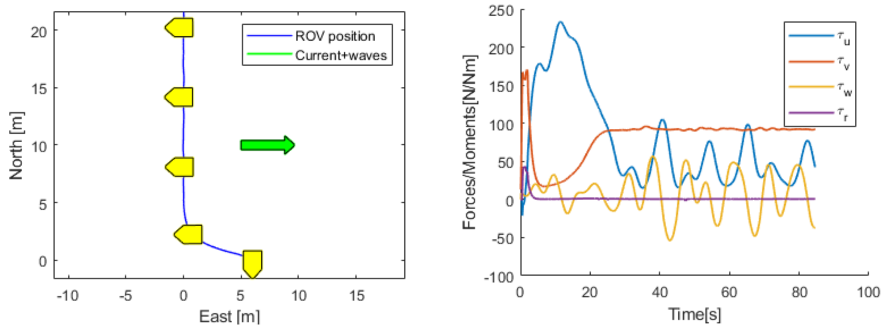

(c) Position of ROV in north-east plane. (d) Thruster forces and moments.

Figure 10.4: Straight line path following with constant, irrotational current and waves.

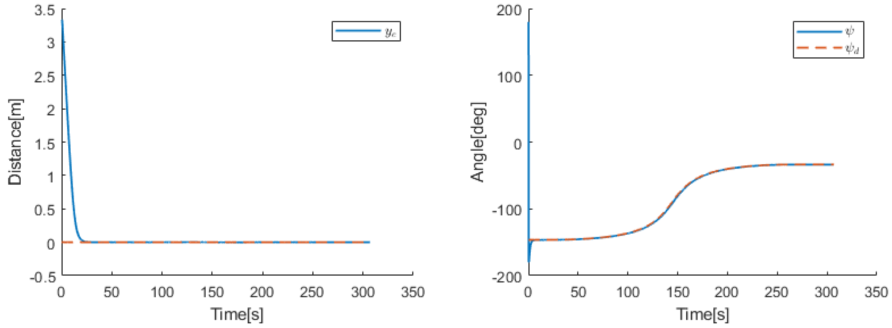

(a) Crosstrack error (b) Heading tracking

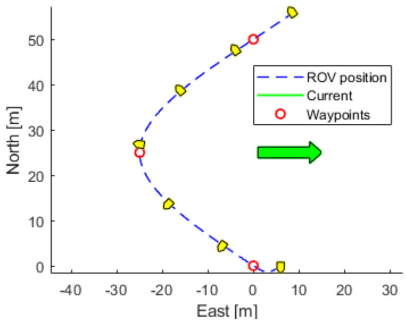

(c) Position of ROV in north-east plane.

Figure 10.5: Curved line path following with constant, irrotational current.

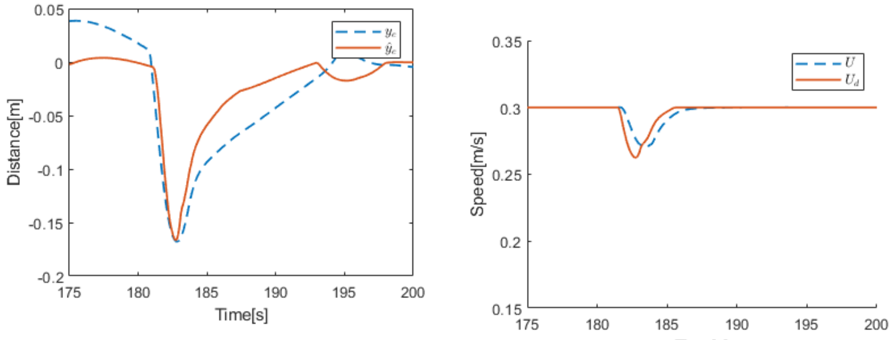

(a) True (stippled) and estimated crosstrack error.

(b) Desired and actual (stippled) speed.

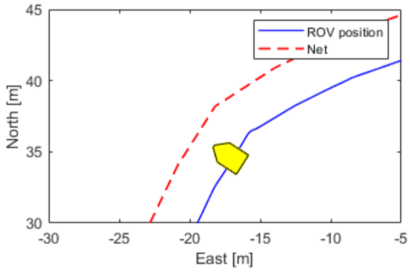

(c) Position of ROV in north-east plane.

Figure 10.6: Net following with speed reduction.

	k_p	k_i	k_d
Heading	15	0.5	0.1
Depth	50	0.2	
Surge	500	120	
Sway	500	120	

(a) Design parameters of PID controllers.

	λ	k_s	k_d	ϕ
Heading	1	50	10	0.5
Depth	3	10	30	0.5
Surge	0.5	500	5	1
Sway	0.5	400	3	1

(b) Design parameters of 1st order SMC controllers.

	λ	ε	γ	ω	α_m
Heading	0.5	0.0001	1	8	0.05
Depth	0.5	0.0001	1	8	0.05
Surge	10	0.0001	1	8	0.15
Sway	10	0.0001	1	8	0.15

(c) Design parameters of adaptive STA controllers.

Table 10.3.1: Control law design parameters.

10.3 Control Laws

This section will present and discuss results from simulations of the presented control laws. During simulations with waves as reference signals, the reference signals are given by

$$\begin{aligned} z_d(t) &= 2\sin(0.01t)\text{m} + 6\text{m} \\ \psi_d(t) &= \frac{\pi}{2}\sin(0.025t)\text{rad} \\ u_d(t) &= 0.2\sin(0.01t)\text{m/s} \\ v_d(t) &= 0.2\sin(0.01t)\text{m/s} \end{aligned} \tag{10.1}$$

The controller gains are stated in Table 10.3.1. These were found through design and testing with the aim of fast convergence with little overshoots.

10.3.1 PID Control

In general, the response of the PID controllers are good. Figures 10.7 and 10.8 shows the response and applied thruster forces and moments during a step in the reference. We can see that all the controllers reach their references. However, we also observe slightly unwanted behavior, such as overshoots in the heading and depth controllers. In general, all controllers are also prone to integral wind-up, which happens at the depth controller during saturation, which is seen in Figure 10.8b. Furthermore, the PID controllers are not particularly fast, which can be seen in Figure 10.9.

10.3.2 1st Order Sliding Mode Control

The response of the 1st order sliding mode controllers are very satisfying, as seen in Figure 10.10-10.12. Among the improvements compared to the PID controllers are no overshoot in heading control and a much faster settling time at heading, surge and sway. Furthermore, one can see in Figure 10.12 that the controllers are faster, almost being able to perfectly track the sinusoidal signals.

Because that the signum function is replaced by the saturation function to avoid chattering, the sliding variables s_u, s_v for surge and sway does not converge to the sliding surface when inside of the boundary layer, as seen in Figure 10.13. However, thanks to the PI controller, the tracking error will still converge to its origin, as seen in Figure 10.10. With $\lambda_u = \lambda_v = 0$, ie. no integral action, this was not the case.

A weakness to the depth 1st order sliding mode control controller is its dependency on the estimated restoring forces in heave $\hat{g}_z$. For an imperfect estimation, the controller will indeed experience a bias in tracking error, as seen in Figure 10.14. During this simulation, the sliding mode controller is simulated with $\hat{g}_z$ corresponding to a ROV mass of 85kg, as opposed to the simulation model of 90kg. One can argue that the restoring forces vector $\boldsymbol{g}(\boldsymbol{\eta})$ can easily be estimated, as it is possible measure the mass W and water displacement ∇ of the ROV, as well as having measurements of θ, ϕ. However, simulations shows that only a small estimation error can have significant impact. Furthermore, a model free control law will be more flexible to use across different vehicles and operations.

10.3.3 Adaptive Super-Twisting Algorithm

Finally, the performance of the adaptive STA is tested. In general, the response of the control law is very satisfying as seen of the step response in Figure 10.15. Compared to the two other control laws, the depth controller has less overshoot, as well as having a shorter settling time. The velocity controllers doesn't converge as fast compared to 1st order sliding mode control. This is partly to due with the gain being adaptive, as it takes time to reach good tuning, which can be seen in Figure 10.17. The slow convergence may also be the consequence of the modified sliding variables s_u, s_v. However, when the sliding surface is reached, the controllers does a better job at keeping the sliding variables to the sliding surface, and consequently is able to follow faster references, as shown in Figure 10.18.

The good tracking performance comes at a price, namely a high input activity as shown in Figure 10.16. This is due to the constant activity of "forcing" the sliding variable to the sliding surface. Particularly, the thruster moments τ_r in yaw are highly active. In practice, this may be problematic for control, and may lead to wear and tear on the actuators. In general, lowering α will also lower the amplitude of the input activity. This can be done indirectly for example by increasing λ or α_m.

Another aspect of adaptive STA which may be problematic is that the adaptive law is positive semi-definite, ie. $\dot{\alpha} \geq 0 \forall t$. Hence, it can only increase. For operations were the reference signal may experience rapid changes, such as steps, this may lead to a too large adaptive gain, as seen in Figure 10.19. Here, the heading control is applied a pulse at the reference. The adaptive gain will be ever-increasing, eventually leading to instability. For net following, this may be the case for heading control, as the net heading can indeed experience steps at mooring points.

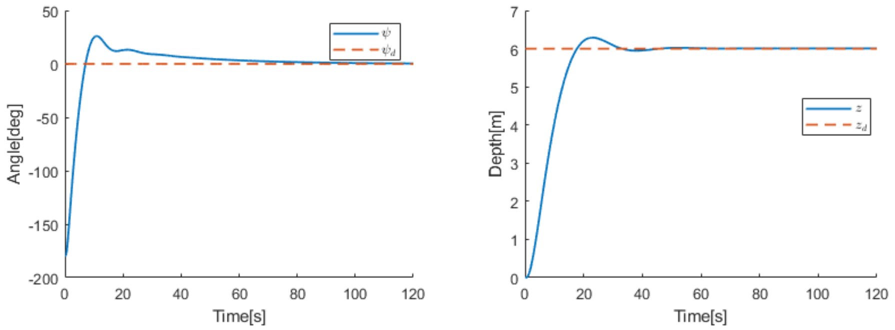

(a) Step response of heading PID controller.

(b) Step response of depth PI controller.

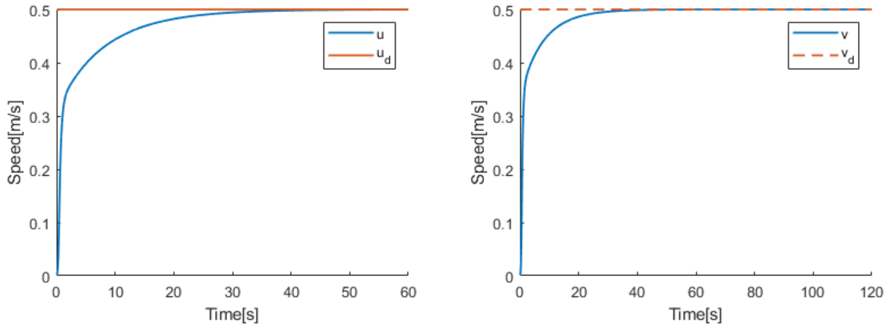

(c) Step response of surge PI controller.

(d) Step response of sway PI controller.

Figure 10.7: Step response of PID controllers.

10.3.4 Final Remarks on Tuning

The control gains in Table 10.3.1 are tuned using simulations. However, in practice alterations may be required. Particularly, several of the gains are large, especially for the velocity controllers. They are designed so in order to achieve sufficiently fast response. This works well with precise and frequent measurements. Noisy measurements may be problematic, and it may be needed to lower certain control parameters in order to achieve stability.

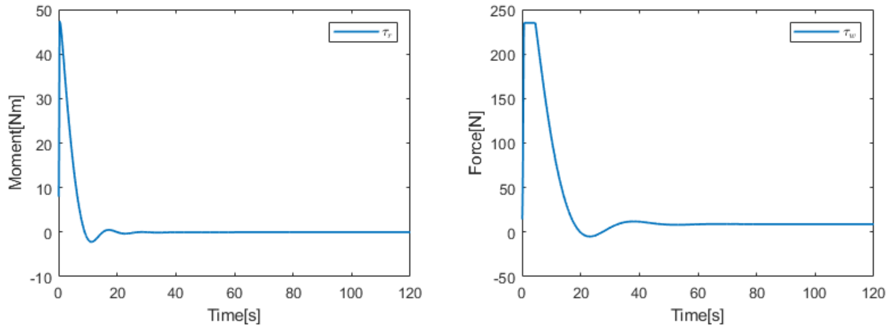

(a) Thruster moments in yaw. (b) Thruster forces in heave.

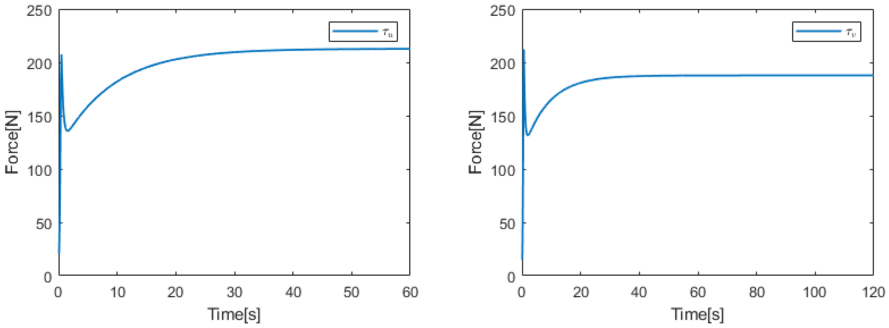

(c) Thruster forces in surge. (d) Thruster forces in sway.

Figure 10.8: Thruster forces and moments during step response with PID control.

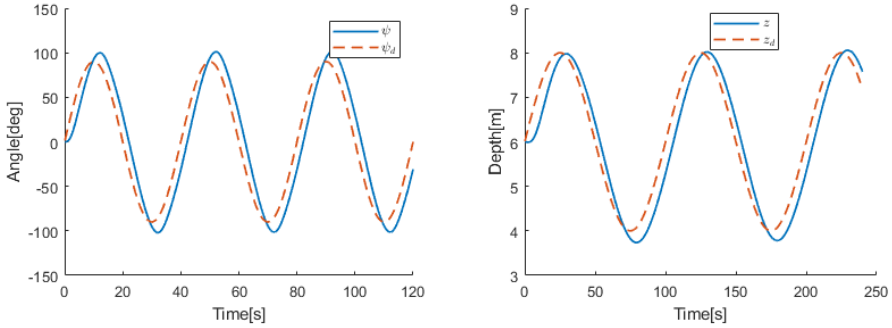

(a) Response of heading PID controller. (b) Response of depth PI controller.

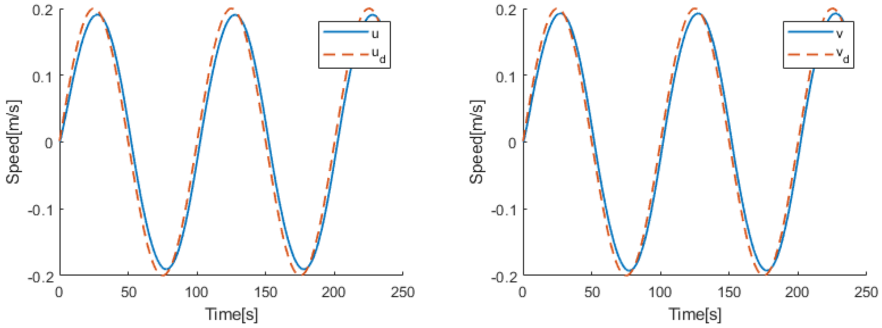

(c) Response of surge PI controller. (d) Response of sway PI controller.

Figure 10.9: Response of PID controllers with sinusoidal reference signal

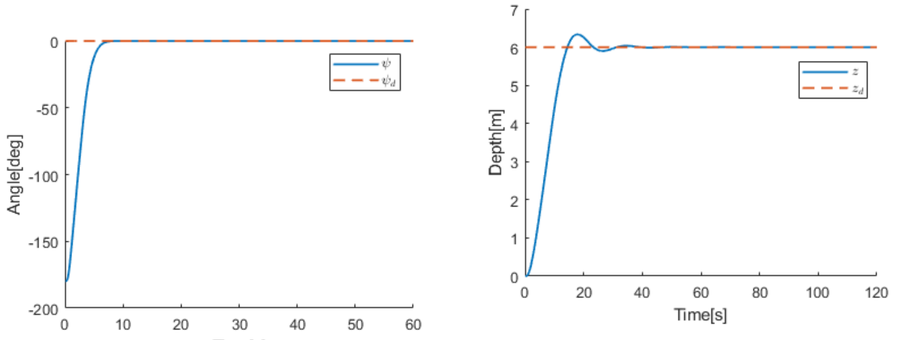

(a) Step response in heading.

(b) Step response in depth with perfect model.

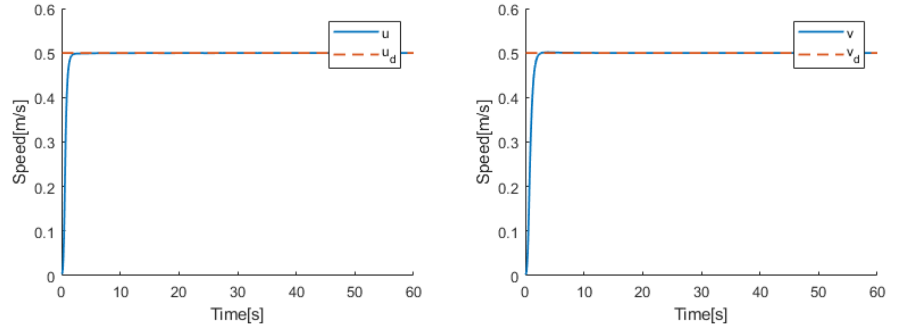

(c) Step response in surge.

(d) Step response in sway.

Figure 10.10: Step response with 1st order SMC.

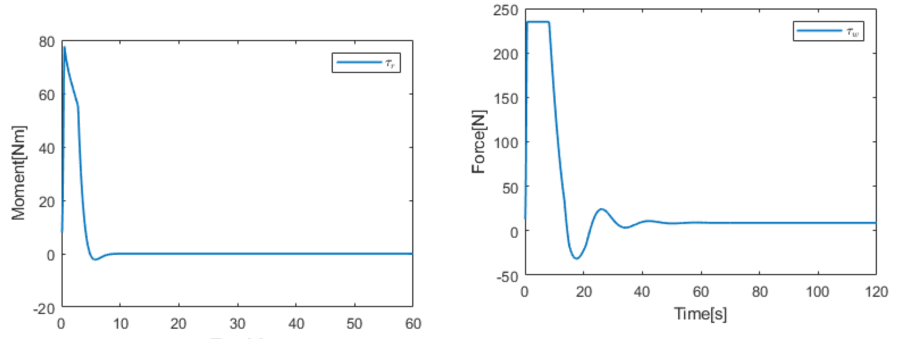

(a) Thruster moments in yaw.

(b) Thruster forces in heave with perfect model.

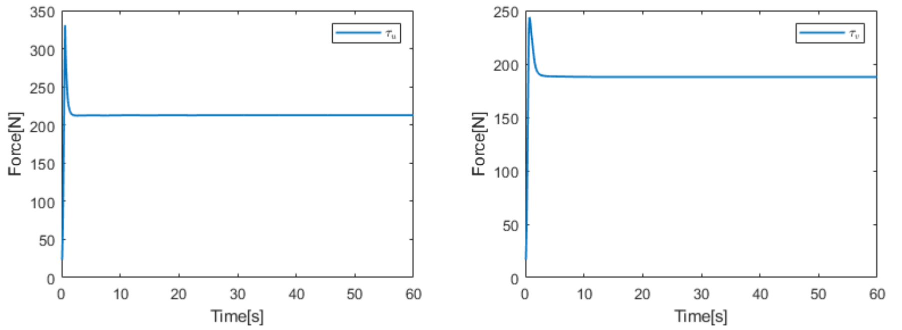

(c) Thruster forces in surge.

(d) Thruster forces in sway.

Figure 10.11: Thruster forces and moments during step response with 1st order SMC.

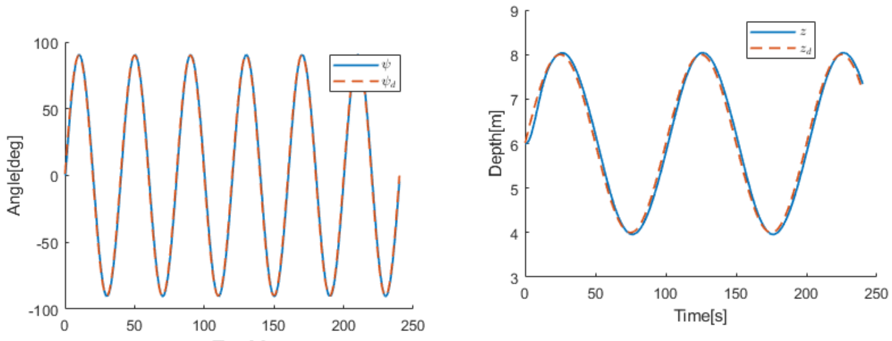

(a) Response in heading.

(b) Response in depth with perfect model.

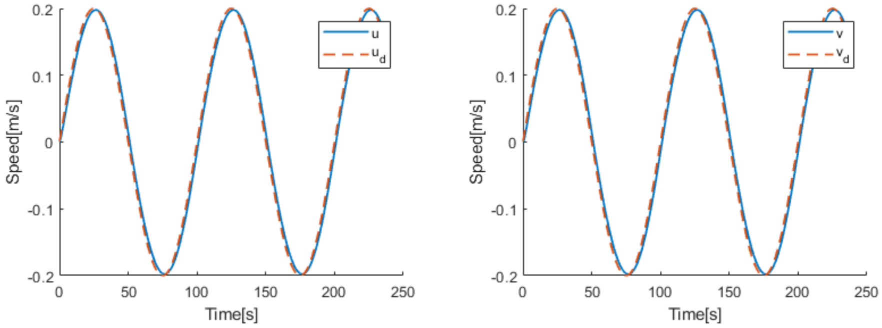

(c) Response in surge.

(d) Response in sway.

Figure 10.12: Response of 1st order SMC with sinusoidal reference signal.

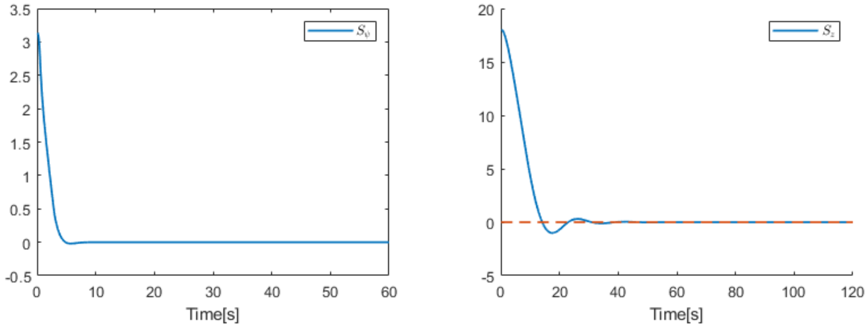

(a) Sliding variable in heading.

(b) Sliding variable in depth.

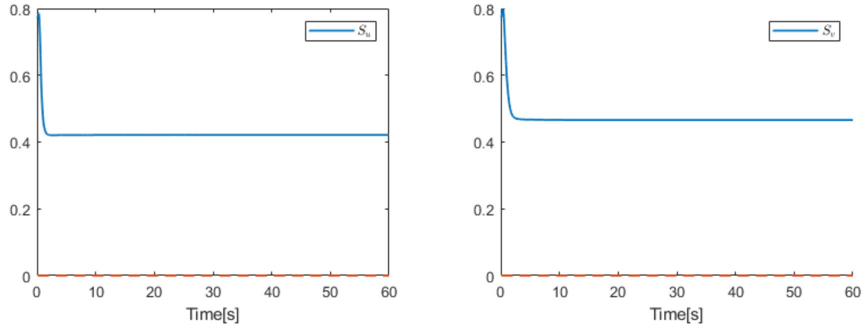

(c) Sliding variable in surge.

(d) Sliding variable in sway.

Figure 10.13: Sliding variables in 1st order SMC with step in reference. Notice the steady-state error in surge/sway.

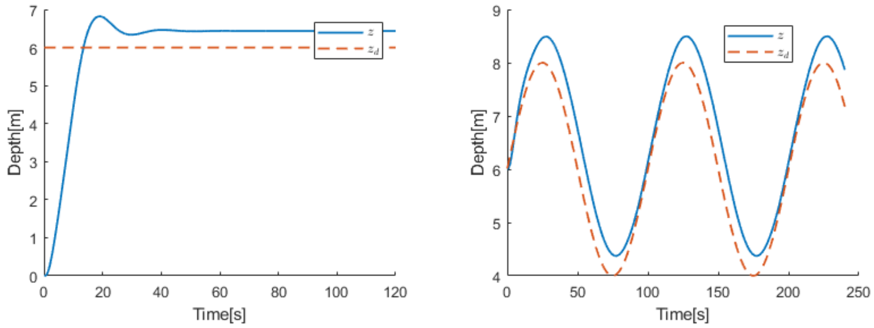

(a) Step response. (b) Response to sinusoidal wave.

Figure 10.14: 1st order sliding mode depth control with modeling error.

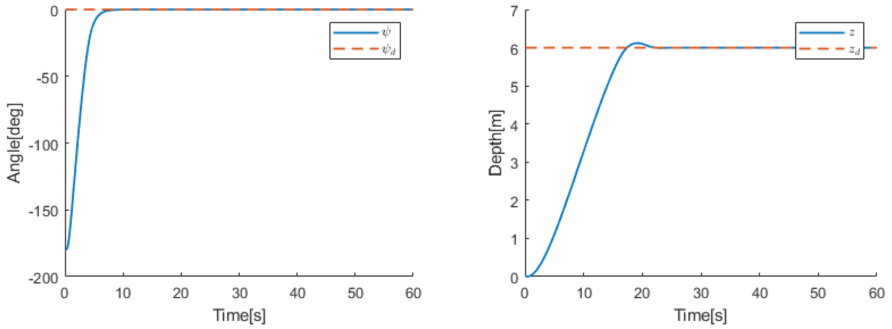

(a) Step response in heading. (b) Step response in depth.

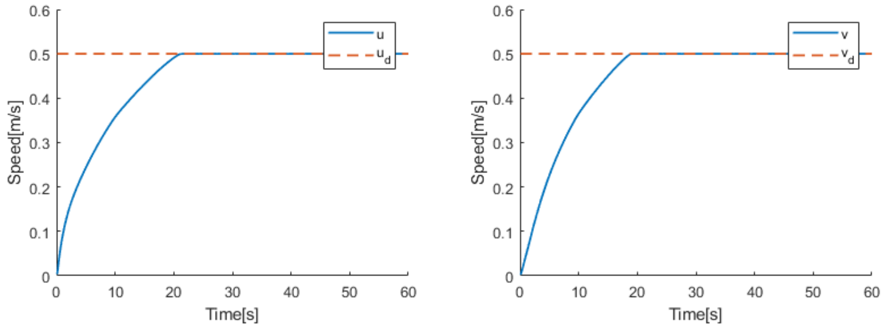

(c) Step response in surge. (d) Step response in sway.

Figure 10.15: Step response with adaptive STA.

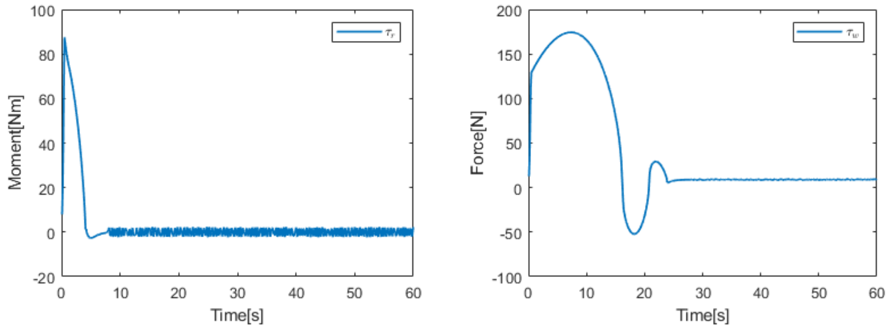

(a) Thruster moments in yaw.
(b) Thruster forces in heave.

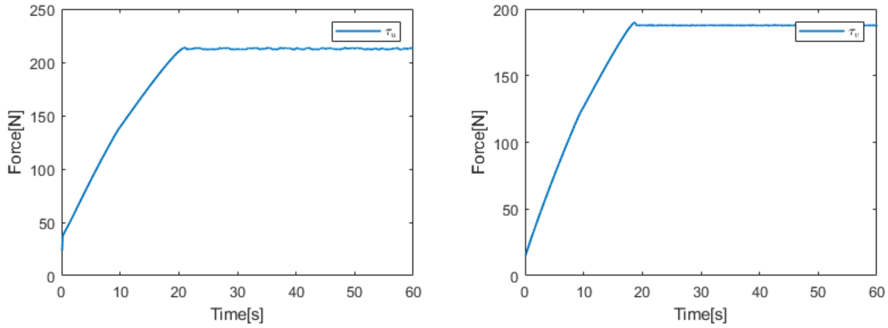

(c) Thruster forces in surge.
(d) Thruster forces in sway.

Figure 10.16: Thruster forces and moments during step response with adaptive STA.

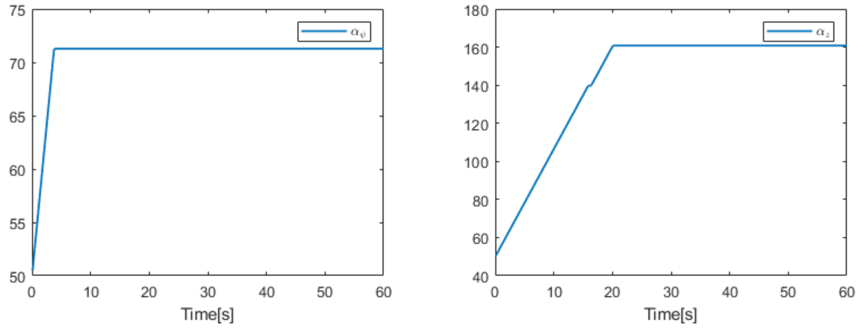

(a) Adaptive gain in yaw.
(b) Adaptive gain in heave.

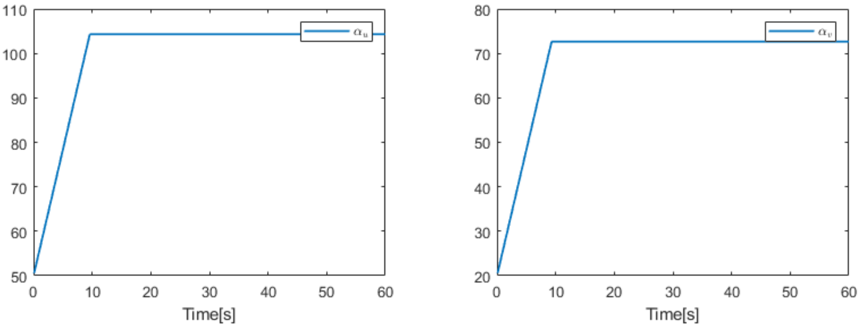

(c) Adaptive gain in surge.
(d) Adaptive gain in sway.

Figure 10.17: Adaptive gain during adaptive STA with step in reference.

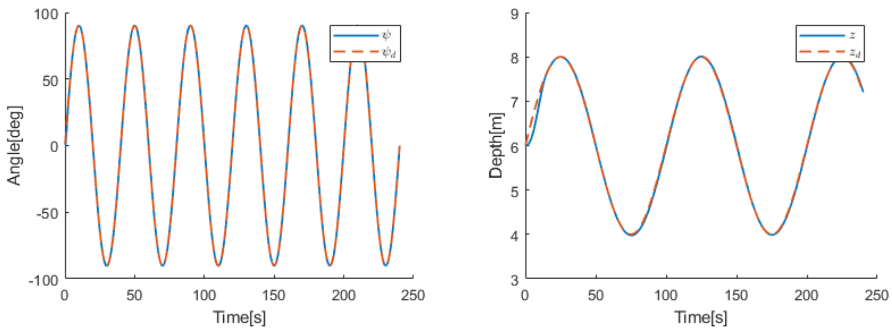

(a) Response in heading. (b) Response in depth.

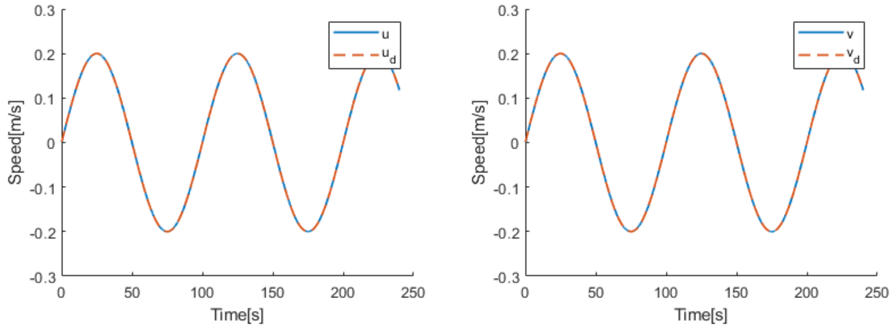

(c) Response in surge. (d) Response in sway.

Figure 10.18: Response of adaptive STA with sinusoidal reference signals.

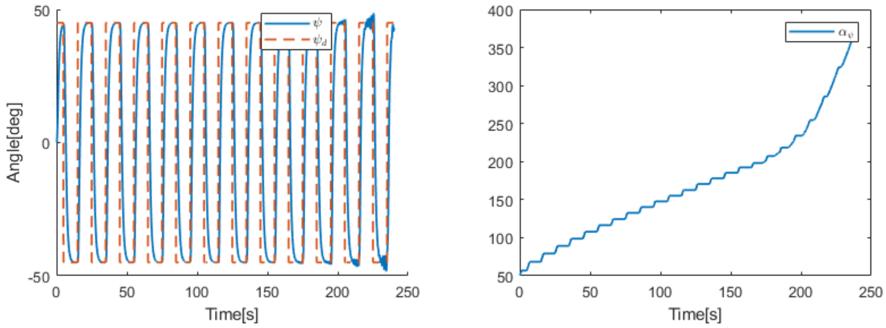

(a) Reference tracking. (b) Adaptive gain.

Figure 10.19: Adaptive STA heading control pulse response.

10.4 Net Following

Lastly, the complete GNC system is simulated trying to follow a static net pen structure. During the simulations, the surge, sway and depth controllers are chosen as adaptive gain STA, while the heading controller is the 1st order SMC. All parameters are chosen according to Table 10.3.1. The desired distance d_d to the net is 3m, while the desired speed is $U_d = 0.35\text{m/s}$.

No Environmental Disturbances

Figure 10.20 shows the simulation results from net following without environmental loads. As seen, the ROV successfully is able to follow the net pen. At the mooring points, the reference values experiences a step, which leads to a slightly worse response. However, the approximated crosstrack error stays within 0.2m.

Environmental Disturbances

Figure 10.21 shows simulation results from net pen following with environmental loads. A constant and irrotational current with velocity vector $[V_x, V_y, V_z]^T = [0, 0.35 \text{ m/s}, 0]^T$ is applied, as well as low-frequency waves with significant wave height $H_s = 1\text{m}$, direction $\beta_w = \pi/2$ and period $T_p = 16\text{s}$. The waves are left unfiltered. The desired depth during the simulations is $z_d = 6\text{m}$.

The waves leads to a more active use of the thrusters, as seen in Figure 10.21d. One can also observe how the induced wave forces varies with direction and frequency. Still, the GNC system performs fairly well, the biggest crosstrack error is 0.43m.

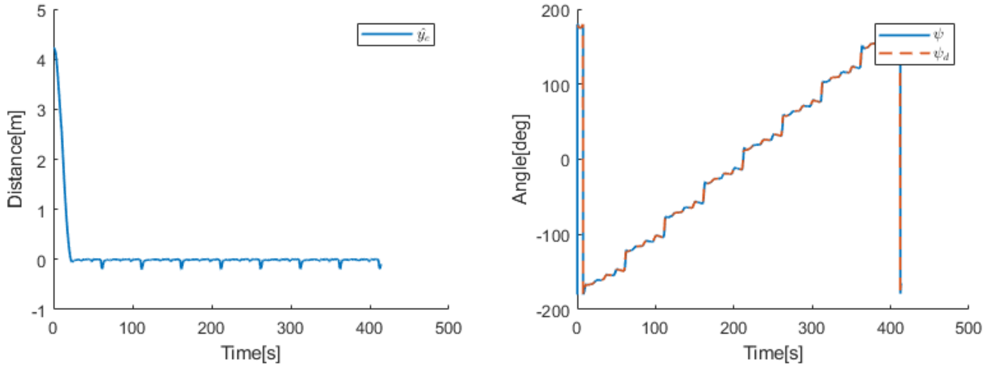

(a) Approximated crosstrack error. (b) Heading tracking.

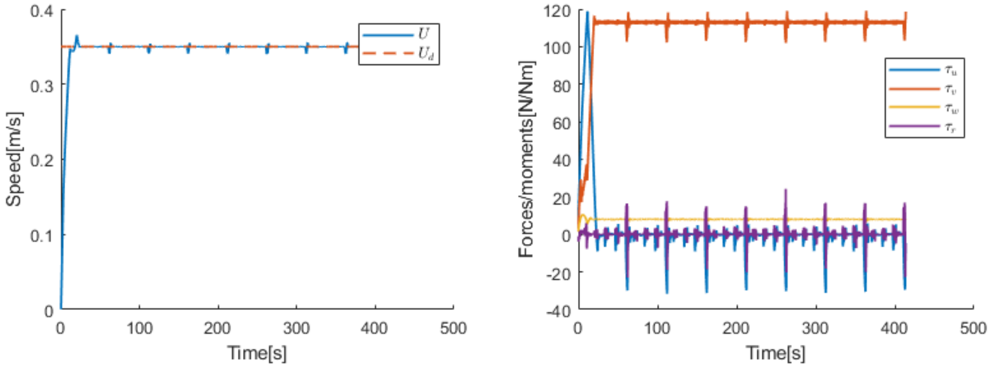

(c) Speed tracking. (d) Thruster forces and moments.

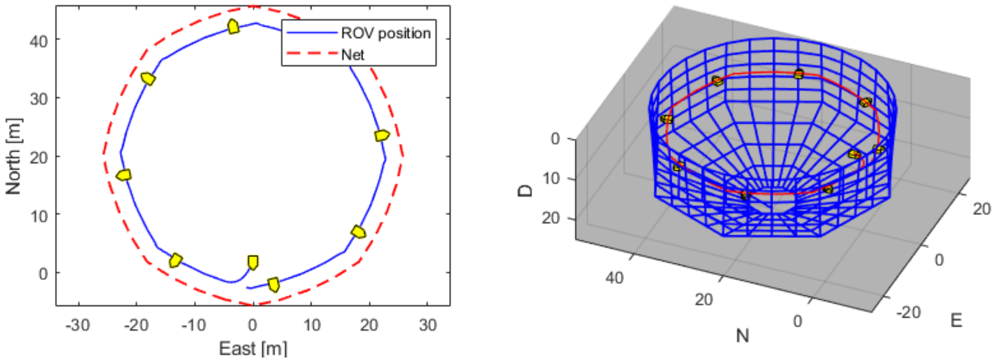

(e) ROV position in north-east plane. (f) ROV position in 3D plane.

Figure 10.20: Net following without environmental disturbances.

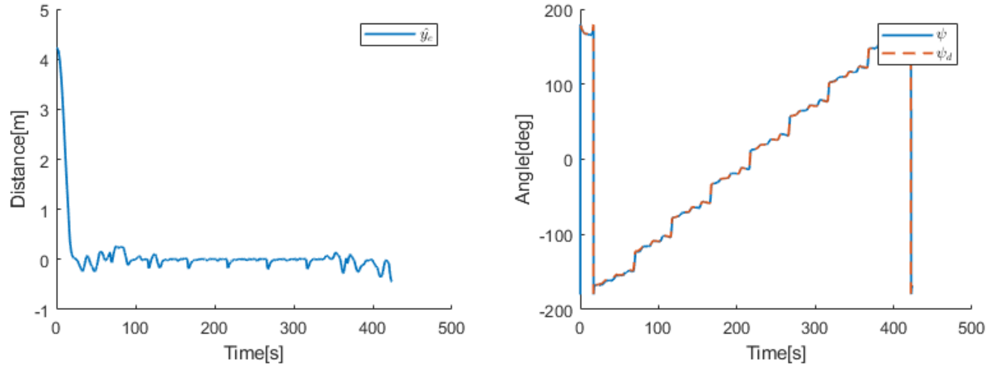

(a) Approximated crosstrack error. (b) Heading tracking.

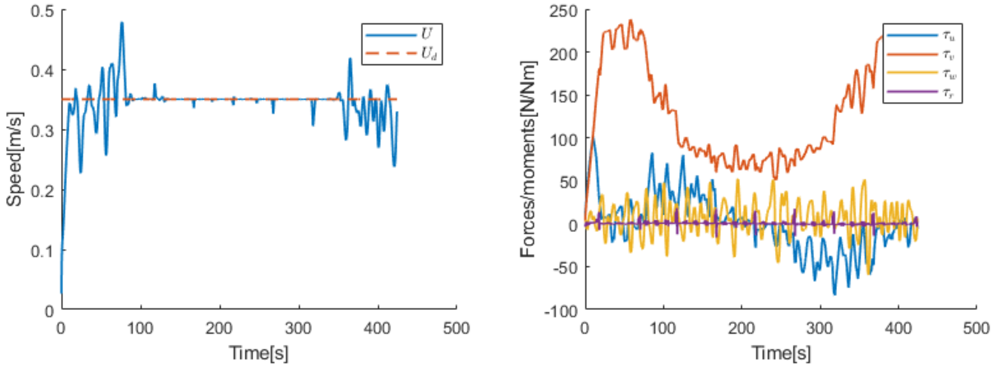

(c) Speed tracking. (d) Thruster forces and moments.

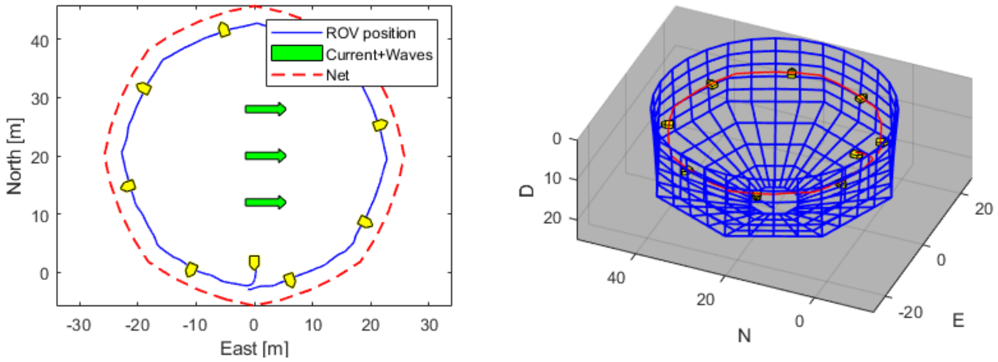

(e) ROV position in north-east plane. (f) ROV position in 3D plane.

Figure 10.21: Net following with environmental disturbances.

Chapter 11

Experimental Results

To verify the presented methods, several practical experiments were undertaken, both at a basin near the Ocean Basin Laboratory at Tyholt, Trondheim and at SINTEF ACE Rataran, a full-scale aquaculture laboratory at Frøya, Norway.

11.1 Basin Tests

The first experiments were undertaken at Tyholt during September, 2019. The experiments took place at a small water basin next to the Oceanic Basin. The dimension of the water basin was of approximately 4mx8m, with an obtuse angle at one wall, see Figure 11.2. This corner is similar to corners one might experience at net pen mooring points, and thus was an ideal platform for testing. The tank had a depth of 4m. The DVL was attached to the ROV as shown in Figure 11.1.

The aim of the initial tests was to verify that the net approximation and guidance law were working, as well as tuning control parameters. The tests were done without the presence of environmental disturbances such as waves and currents. The control system was given by the PID control laws in Section 8.1, and, after several trials, the control parameters and references were set according to Table 11.1.1. The trials were done without the speed reduction formula activated.

In general, the performance during the wall following trials was a success. Figure 11.3 shows the performance of the net following method when interacting with the basin wall. As seen in Figures 11.3f,11.3g, the DVL measurements were steady and looked accurate when compared to visual observations.

It can be observed in Figure 11.3a that the crosstrack error successfully is minimized. However, at the corner, the magnitude of the crosstrack error increases. The main reason for this can be seen in Figures 11.3c,11.3d. Particularly, the sway controller doesn't manage to follow the rapid change in reference. This leads to an increase in crosstrack error magnitude, which can be explained from Equation (7.6). The result can also be observed in Figure 11.3e, where one can see that the ROV is not able to follow the desired course $\chi_d = \psi_d + \text{atan2}(v_d, u_d)$ as the control system is not fast enough. However, despite the sharp corner, the ROV manages to stay approximately 1.3m meters from the wall at the minimum, before again minimizing the crosstrack error.

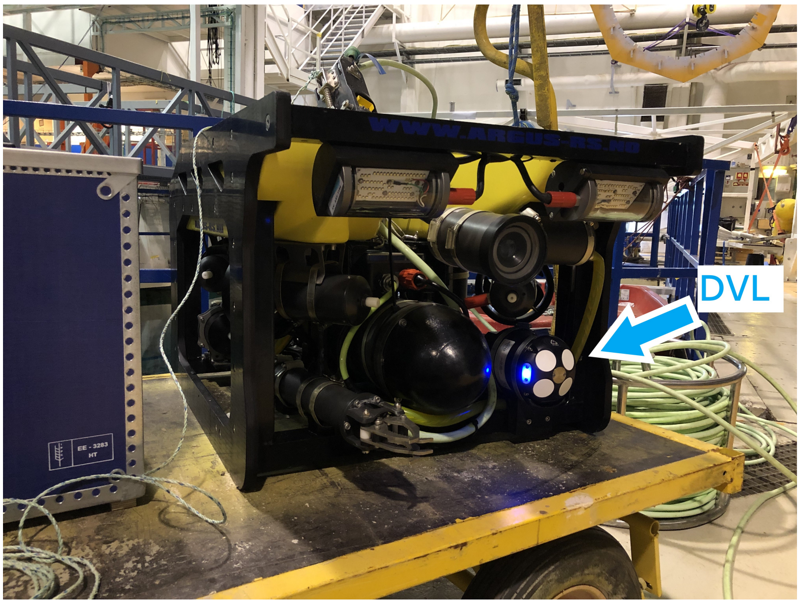

Figure 11.1: ROV with DVL attached.

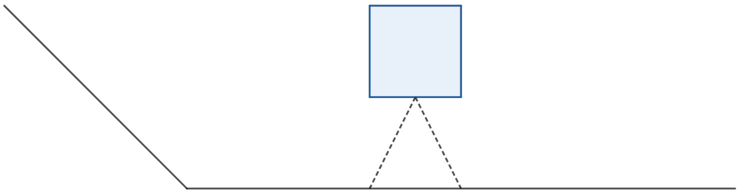

Figure 11.2: Shape of water basin. Horizontal projection.

In general, the velocity controllers performs decently, apart from not being reactive enough at the corner. One reason for the sway controller not being reactive enough might be because the integral state has grown large prior to the corner, and because the integral gain is so large, the integral term will dominate the proportional term. In hindsight, a lower integral gain might lead to better results. From Figure 11.3b, it is seen that the PID heading controller is underdamped, which is consistent with the simulation results from Section 10.3.

From Figure 11.3h, it is seen that there is little differences between the approximated "present wall heading" ψ_d, the predicted future heading ψ_f. This confirms that there are little differences between the different net approximation methods. As seen in Figure 11.3f, the forward pointing DVL-beams $\boldsymbol{r}^d_{1,4}$ detects the basin corner prior to the beams $\boldsymbol{r}^d_{2,3}$. From Figure 11.3a, the response of the crosstrack error looks similar to the response of the forward pointing beams $\boldsymbol{r}^d_{1,4}$ at the corner. From this, it seems like the approximation method does detect the corner in time, and may suggests that the feedforward in crosstrack error is unnecessary.

	K_p	K_i	K_d
Heading	15	0	0.1
Surge	500	120	
Sway	500	120	

(a) PID Gains.

	ρ	σ	d_d	U_d
Guidance Law	1	0	2m	0.2m/s

(b) Guidance law parameters.

Table 11.1.1: Parameters and references during basing trial.

11.2 Full-scale Test at SINTEF ACE Aquaculture Laboratory

At the 31th of October and 14th of November, full-scale experiments took place at SINTEF ACE location Rataran. Rataran is a coastal fish farming site at Frøya in Trøndelag, Norway. The site lies behind a series of small island which provide shelter from swell waves. The observed wave height at the 31th October was estimated to be 0.25m, while the current speed was 0.25 ms^{-1}. At the 14th of November, the current speed was 0.5 ms^{-1}, while there were close to no waves.

The experiments took place in an empty net cage with no fish. As these was still initial tests, this was chosen in order to limit the scope of the experiments. One of the main focuses of the tests was to verify interaction between the DVL and the net, as well as finding ideal settings for the DVL.

The control system was given by the PID controllers. The speed reduction function was unactivated during the trials. The measured states was fed unfiltered back to the control system.

DVL Settings

The DVL model was Nortek DVL 1000 (1 MHz). All settings is chosen according to factory settings unless specified.

To find the ideal settings for the DVL, a set of experiments were undertaken. At various depth, the ROV was driven towards and away from the net, with the DVL pointing approximately normal to the net surface. It was found that DVL successfully interacted with the net. The outside of the net pen was covered with a lice skirt down to a depth of approximately 6m. It was observed that the DVL system interacted with the net pen, not the lice skirt. As the ROV operated inside the net pen, this is what was hoped for.

It was found that the settings that gave the best response was a power level of -2db, which is the maximum setting, as well as a range of 6m. The measurements at this setting was steady, contrary to jumps in measured distance or loss of pings. Visual inspections of the ROV distance to the net, showed that the measurements was consistent with observations. A lower power level or higher range gave more jumps in measurements. The blanking distance, ie. the range from which within DVL pings are ignored, was set to 0.02m. This may be a parameter which should be increased if fish are present.

	K_p	K_i	K_d
Depth	100	1	
Heading	15	0.1	1
Surge	200	5	
Sway	200	5	

(a) PID gains.

	ρ	σ	d_d	U_d
Guidance Law	1	0	2m	0.2m/s

(b) Guidance law parameters.

Table 11.2.1: Parameters and references during SINTEF ACE trials.

Net Pen Following

During net pen following trials, it was clear that the measured distance of travel for the DVL beams was mostly steady, consistent and accurate when compared to visual observations, as seen in Figure 11.4g. However, jumps in measured distance or loss of pings could occasionally be seen.

As seen in Figure 11.4h, the DVL measured velocity in $\{b\}$ was more affected by noise compared to the basin trials. This could be expected, as the net has a lower target strength compared to the basin wall, as well as the ROV operating in the presence of waves. The measurement noise proved to problematic for the velocity controllers. Therefore, the controller gains were lowered, which gave better results. The controller parameters are given by Table 11.2.1.

The results from trials can be seen in Figure 11.4. The trials were a success. During this trial, the ROV traveled about a fourth of the net pen. From visual observations, the distance to the net pen was steady and the ROV heading was approximately normal to the net pen surface. This can be verified by the data seen in Figures 11.4a and 11.4b.

As seen in Figures 11.4d,11.4e, the velocity controllers doesn't reach their references in time, as the integral gain is low. The consequence is that the ROV course doesn't quite reach the desired course, and the approximated crosstrack error shows the ROV being a bit too close to the net. This could be explained from the surge velocity, which have a near steady-state error of 0.05 m/s. It can also be observed that the heading and depth controllers does a satisfying job in tracking their reference values.

Through the HD camera attached to the front of the ROV, the net could be observed during the trials. The images were clear and steady, and the state of the net could easily be observed. This points to the net pen following method being capable of being utilized for net pen inspection tasks.

The regular jumps or losses of DVL measurements give jumps in reference values. However, as the jumps and losses only lasts for very short moments, and the control system not being fast enough to follow the reference jumps, they did not result in any observable loss of performance.

The net pen following algorithm was also tested with integral gain in the guidance law, which can be seen in Figure 11.5. Here, the integral gain was set to $\sigma = 0.05$. The results from trials with integral gain lead to a more oscillatory response in crosstrack-error. From this, one can conclude that if one are to use integral action, the gain σ should be of a small value compared to Δ.

On the 14th of November, a new set of trials were undertaken. The primary goal of this trial was to test a new GUI application. During this trials, the net pen following algorithm was again tested. As previously, the tests took place in an empty net. This time, the NED position of the ROV was logged by the use of a USBL system.

Because of the nature of the GUI experiments, there were commanded changes in reference for both the desired speed, depth and direction during net pen following. The PID controllers were tuned as in Table 11.2.1, while the LOS guidance law was tuned according to $\Delta = 1, \rho = 1, \sigma = 0.05$.

Figure 11.6 shows the results from net pen following. The depth and heading controllers track the reference well. Again, we can see a slightly oscillatory response in crosstrack error due to the integral control. This time, however, it approaches a near steady-state around the origin. Again, the sway velocity controller doesn't reach its desired value in time.

Figure 11.6g shows the measured position in NED. It is clear that the USBL measurements are affected by noise. Still, one can observe the pattern for the traveled path. As the structure of the net pen is not measured or known, the ROV position relative to the net pen is not known. However, one can argue that the plotted ROV positional data is consistent with a typical net pen shape.

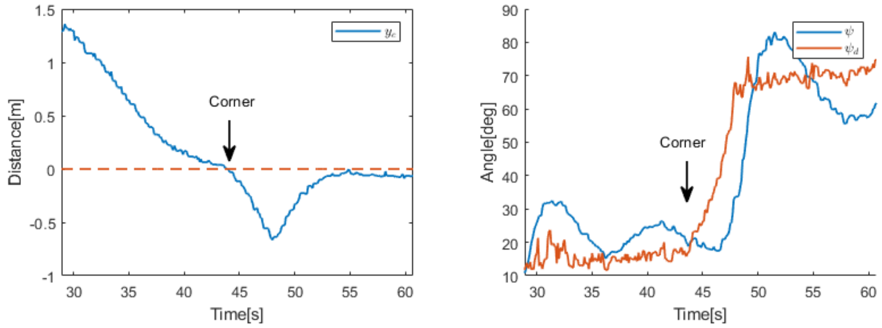

(a) Approximated crosstrack error. (b) Heading tracking.

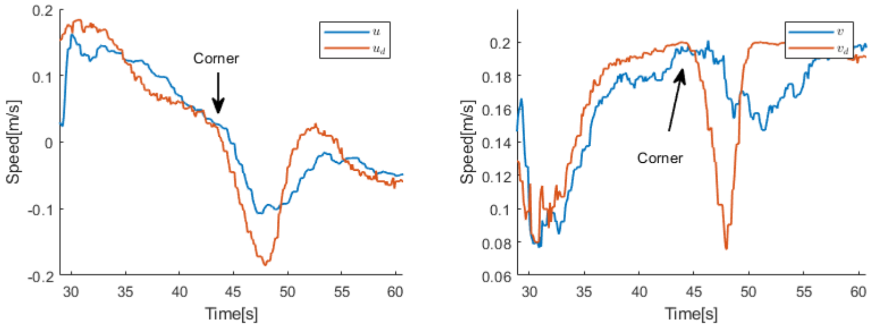

(c) Surge velocity tracking. (d) Sway velocity tracking.

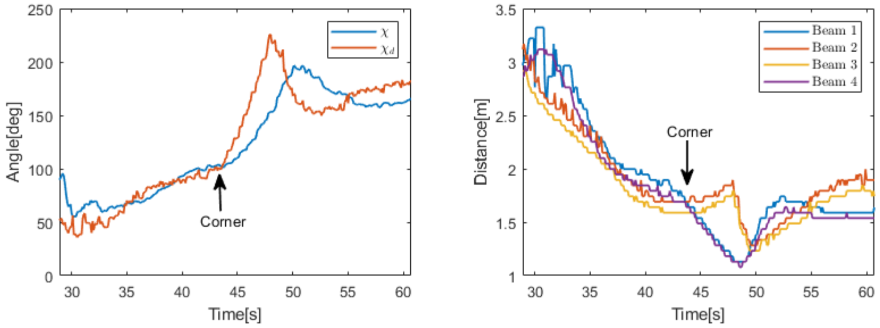

(e) Course tracking. (f) Measured DVL beams distances.

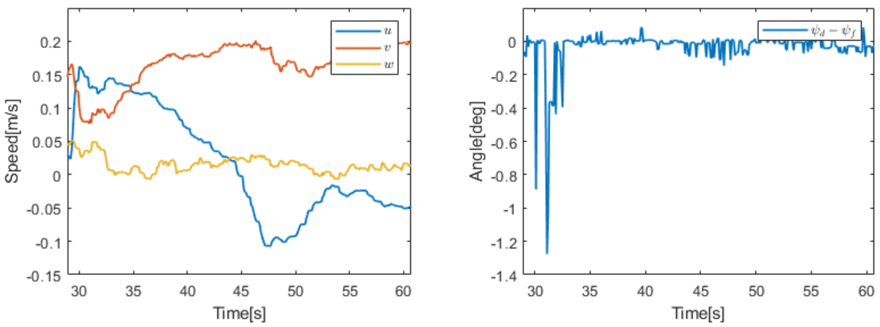

(g) DVL measured velocity in BODY. (h) Difference between ψ_d and ψ_f.

Figure 11.3: Basin wall following using DVL.

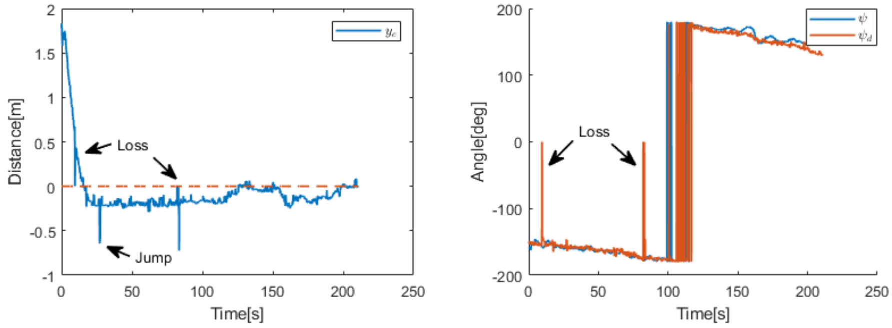

(a) Approximated crosstrack error. (b) Heading tracking.

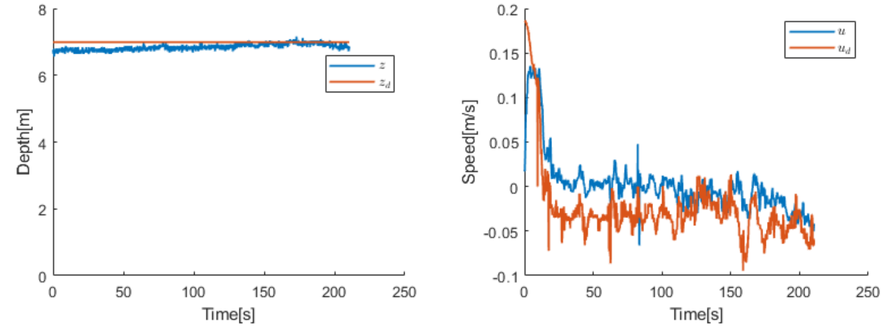

(c) Depth tracking. (d) Surge velocity tracking.

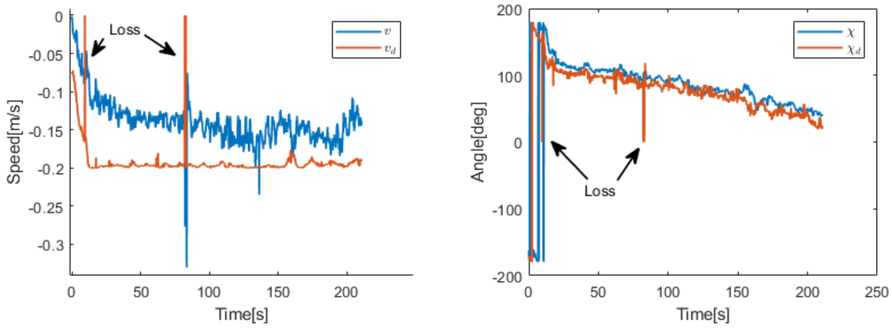

(e) Sway velocity tracking. (f) Course tracking.

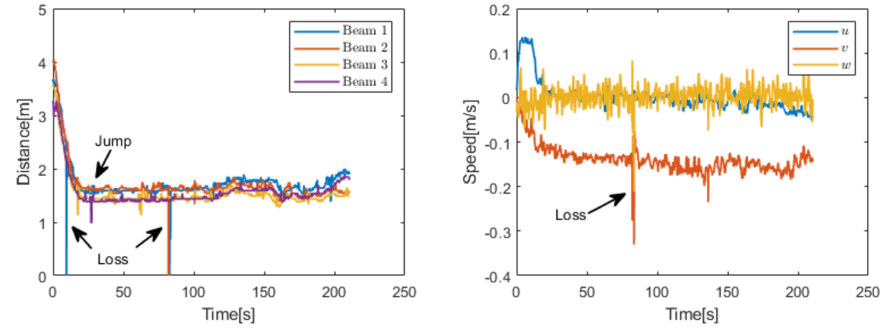

(g) Measured DVL beams distances. (h) DVL measured velocity in BODY.

Figure 11.4: Net pen Following at SINTEF ACE Rataran 31th Oct. 2019. "Loss" marks loss of DVL pings, "jump" marks jump in DVL measured distance.

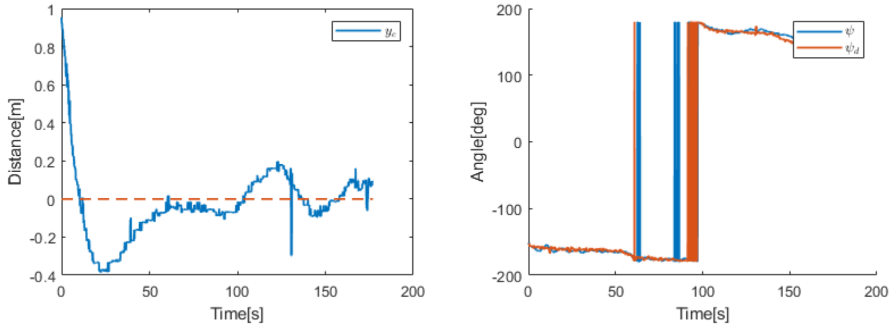

(a) Approximated crosstrack error.
(b) Heading tracking.

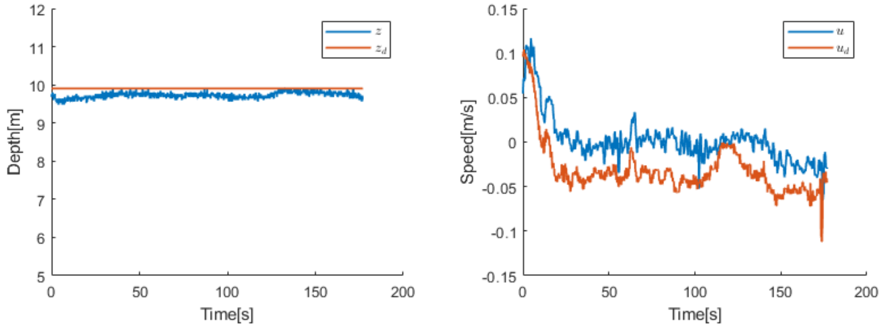

(c) Depth tracking.
(d) Surge velocity tracking.

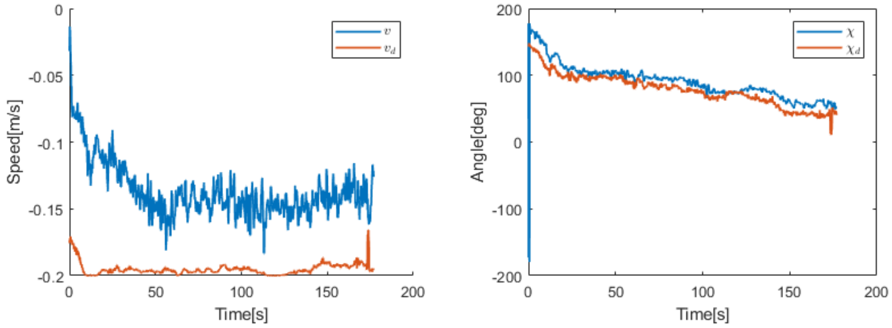

(e) Sway velocity tracking.
(f) Course tracking.

Figure 11.5: Net pen following at SINTEF ACE Rataran 31th Oct. 2019 with integral gain $\sigma = 0.05$.

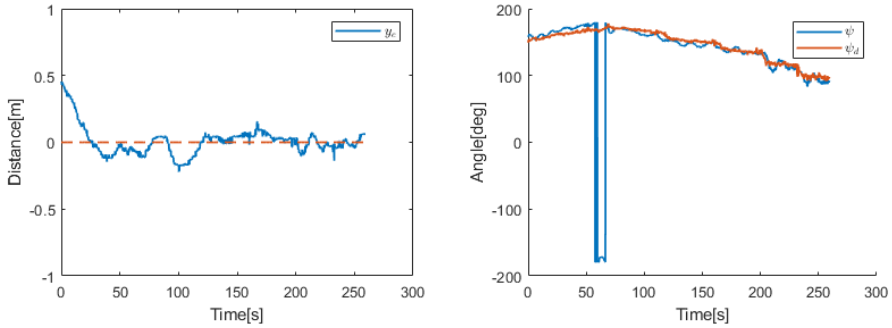

(a) Approximated crosstrack error. (b) Heading tracking.

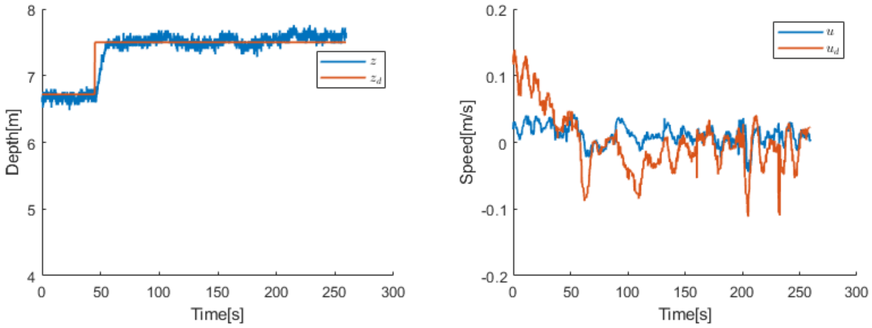

(c) Depth tracking. (d) Surge velocity tracking.

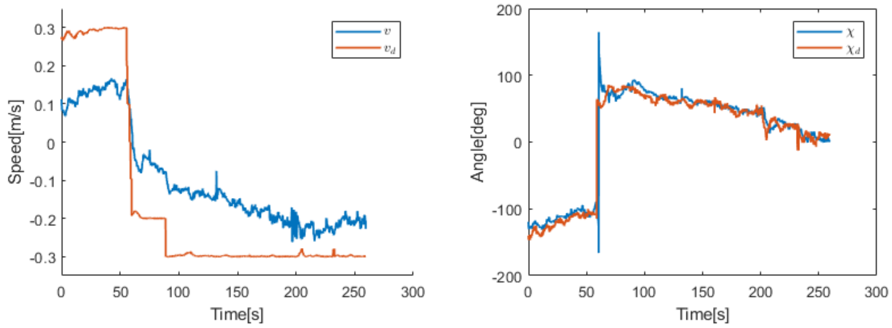

(e) Sway velocity tracking. (f) Course tracking.

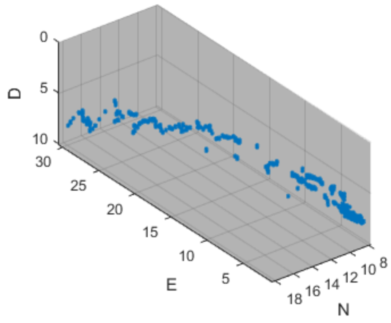

(g) Measured position in NED.

Figure 11.6: Net pen following at SINTEF ACE Rataran 14th Nov. 2019.

Part V

Discussion

Chapter 12

Discussion

In this chapter, the findings of the thesis will be discussed.

12.1 Performance of the Net Pen Geometry Approximation

An aquaculture net pen typically has a conic-like structure, with edges at mooring points. As the net geometry approximation methods are based upon approximating the net pen as a plane, the approximation can never capture the true form of the net. For a local area, the approximation will be more accurate, and, if the net pen structure in front of the ROV has a flat nature, the approximation method may be very precise. This is verified by the simulation results.

As the DVL beam angles are constant, the footprint of the DVL increases with the ROV distance to the net. The net pen geometry approximation will not capture the net pen structure roughness inside of the DVL footprint. Hence, a greater distance to the net decreases the performance of the approximation method. This is again verified by the simulation results, where one can observe that the estimation error of the crosstrack error decreases as the ROV moves closer to the net.

The performance of the approximation also depends on the level of net pen structure roughness inside of the DVL footprint. Consider Figure 12.1a. For a concave curve inside the DVL footprint, the proposed method will underestimate the distance to the net. This can be verified by the simulation results, and happens periodically during net pen following when the ROV traverses a gentle corner. For a convex curve inside the DVL footprint, the method will overestimate $d^*_{b/net}$.

Lastly, the ROV has no knowledge of the net pen structure outside the DVL footprint. As shown in Figure 12.1b, sharp corners or bends outside of the DVL footprint may decrease the performance. Here, the ROV will not ”see” the corner in time, and the true distance to the net pen will be lower than the estimation. This can also be observed from the simulations, where the crosstrack error is overestimated at the mooring points. This could potentially lead to collisions with the net for corners with acute angles or strong deformations of the net, and highlights a limitation of the net pen following system.

The two scenarios presented above, net pen structure roughness respectively inside and outside of the DVL footprint, also represent two dueling stands: For structure roughness

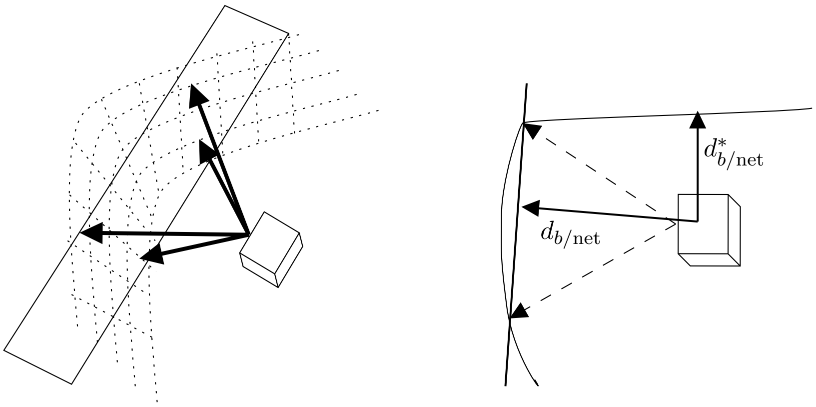

(a) Underestimation of $d^*_{b/\text{net}}$ at gentle, concave corner.

(b) Overestimation of $d^*_{b/\text{net}}$ at sharp corner.

Figure 12.1: Net pen geometry approximation from DVL beams.

inside the footprint, a lower distance the net pen will decrease estimation error. However, structure roughness outside the DVL footprint will be captured earlier by the DVL measurements if the distance to the net pen is larger. Furthermore, distance to the net pen also effects the quality of the camera images. From this, one can conclude that the desired distance to the net pen should be chosen wisely dependent on the operation.

While the approximation never will be perfect, it satisfies the needs of the net pen following system. Simulations shows that for net pen following with a distance of 3m to the net, the crosstrack estimation error is less than 7 cm. The performance in simulations and experiments shows that with this level of error, the net pen is traversed safely with a distance that is experienced as steady by the user.

While the error of between the true net pen normal angle and the approximated net pen normal angle ψ_d is not logged, visual inspections from simulations and experiments points to this being an accurate approximation. For instance, the desired heading in the basin trials in Figure 11.3b is near steady for the wall which is flat. Like the estimation $d_{b/\text{net}}$, the estimation error of ψ^* varies with the roughness of the net pen structure inside of DVL footprint.

Lastly, the approximation accuracy is limited by the number of DVL beams. For higher order approximations, the method requires more measurement points than provided by the DVL's 4 beams. This can for example be achieved with a multi-beam sonar. Another possibility is by windowing several DVL measurements as the ROV traverses the net, and store the measured points in a point cloud. This method requires position measurements of the ROV, which mean positioning measurement errors will enter the net pen geometry approximation. The method proposed by [55] capture elements from both these proposals, where a forward-looking sonar is combined with a Rao-Blackwellized particle filter to perform SLAM for an AUV relative to a net pen.

Prediction of Approaching Corners from Weighing of DVL Beams

By using the fact that two DVL beams point ahead of the ROV, the thesis proposes two methods which utilizes this. By weighing the DVL beams differently, one can approximate alternative planes. The motivation behind both methods is to use this information to predict approaching corners and bends in the net, and, from this knowledge, alter the approximated crosstrack error so that the ROV react faster to the approaching corners. However, simulation and experiments shows that the weighing of the DVL beams give too little differences for these methods to have any perceptible effect.

It is possible that one can extract more information from the DVL beams by using a different method for weighing of the beams. If this is achieved, further testing of the methods and tuning of the parameters ρ, Λ can be assumed. This is a subject for further research.

12.2 DVL Measurements

The proposed method require that DVL measurements interact with the net. Experiments in [54] confirm that this is the case, which is further established by the findings of this thesis.

Experiments shows that the measured traveled distance of the DVL beams are reliable and not particularly affected by measurement noise. However, experiments also shows that jumps in measured distance or loss of measurements from individual beams occurs from time to time. While this does affect the guidance law, it represented little decrease in performance for the ROV, as the changes in references appeared as burst that the control system was not able to follow. From this, one can conclude that the net pen following algorithm is robust to measurement losses as long as they are infrequent and that measurements are resumed shortly.

Experiments also shows that the parameter settings of the DVL affects the performance. A large power level gave a steady response with few measurement losses. Similarly, a range of 6m yielded a good response. If the ROV is to perform net pen following with a greater distance than 6m to the net, then the DVL range has to be increased, with the risk of increased measurement losses.

Another possible source for losses of DVL measurements are that the DVL beams is directed towards the sea surface without any target in the beam paths. This is a limitation for the net pen following algorithm, as the ROV has to be deep enough for all the DVL beams to be directed towards the net. Because of this reason, pitching from induced wave forces may also increase the number of measurement losses.

Experiments shows that the DVL is also able to measure the ROV velocity. While velocity measurement were smooth during the basin trial, they appeared affected by noise during the net pen trials, effectively decreasing the performance of the control system. This maybe explained by the lower target strength of the net. Other possibilities are that the noise is induced from the wave forces or from vibrations in the net.

The DVL signals are dependent on free acoustical beam paths. Salmon have an air-filled swim bladder that helps regulate their buoyancy. This organ can interfere with the transmission and reception of acoustic signals, and therefore fish swimming in the beam paths may present a serious obstacle for the net pen following algorithm. During the experiments in this thesis, the trials were conducted in empty net pens without biomass. In [54], it is seen that fish swimming in the beam paths reduced the ability to obtain reliable measurements. It is reported that it was difficult to obtain obstacle free paths at distances greater than 7m. At distances closer than 3m, the measured distance to the net seems more reliable. Experience shows that fish have a tendency of staying clear of ROVs with a few meters, which may explain the results from [54].

While the Nortek DVL 1000 model has an internal system for filtering of the DVL signals, it may be necessary to do further filtering in order to achieve more reliable measurements. Certainly, combining the velocity measurements with a state estimator such as a Kalman filter, should provide better measurements. This would also allow dead-reckoning. Another idea is to perform filtering of the approximated crosstrack error y_e or desired heading ψ_d, alternatively of the parameters of the approximated net pen surface $f(x, y, z)$ itself. A possibility is to assume that the crosstrack error dynamics is continuous and the net pen static, such that the dynamics of the crosstrack error is coupled with the vehicle states, which can be utilized by an observer. This should also allow dead-reckoning for the crosstrack error. This remains as a subject for further research.

12.3 Performance of the Guidance Law

The LOS guidance law is a familiar method with proven stability. This is again verified by the findings of this thesis. The thesis results also demonstrates how a fully-actuated vehicle can minimize the crosstrack error independently of the heading. Furthermore, it is demonstrated that perfect velocity tracking implies perfect course tracking, thus removing the need for integral action in the guidance law.

As the DVL measures velocity in 3 DOFs, it is possible to track the crab angle and course angle. Instead of using the heading angle to minimize the crosstrack error, it is possible to use the crab angle by controlling the surge and sway velocity. A proof is given which demonstrates that velocity tracking ensures path following properties for continuous paths. This is verified by simulations, where environmental disturbances are countered by applying thrust forces in the opposite direction to the disturbances.

While this approach have the potential of being very robust to environmental loads, it is dependent on good control of the surge and sway velocity. Poor velocity control implies poor control of the course angle. This can be seen in equation (7.6), and is further established in practical experiments. Errors in velocity control leads to a larger crosstrack error. However, the overall performance of the guidance law was good and even the worst-case performance was acceptable.

The performance with integral action is also tested. It is seen that integral action quickly leads to an oscillating response of the crosstrack error. However, from practical experiments it seems that steady-state crosstrack error from poor velocity control can successfully be eliminated with integral action. Finding a better tuning of the parameters σ and Δ may lead to a more damped response in the crosstrack error, and is a subject for further testing.

The theoretically analysis of the guidance law is dependent on a continuous path. During the experiments, as well as the net pen following simulations, this was not the case. Theorem 1 and 2 cannot be considered valid under these conditions. The consequence can be seen in the response, where the velocity controllers are not able to follow steps in the reference. However, as the performance still is acceptable, it is argued that the guidance law is able to tackle even these conditions, which suggests robustness.

Another parameter that it would be interesting to do further testing of, is the look-ahead distance Δ. During most of the trials, the parameter was set to 1. This yielded a good response. In general, this is a pretty low gain, which yields a reactive response of the ROV. Since the ROV has a short perpendicular length, as well as being very reactive in yaw, this works good. However, it might be possible to find a better tuning.

The performance of the speed reduction function is yet to be tested under practical experiments. It would be exciting to see if this leads to a better and more robust performance. The method is intuitive. However, as the method may lead to reference changes in velocity control, it is possible it may slightly decrease performance. This is also a subject of further testing.

Trials shows that the heading angle is independent of the crosstrack error. This is a result that can be used in a numerous of different ROV applications. Inspection tasks is a common usage of ROVs. For many applications, the operator is interested in the surroundings of the path, and being able to have the viewpoint normal to the path can be advantageous. Net pen inspection is just one example for an operation where this comes in handy, other examples may be inspections of pipelines, mooring lines or even more complex underwater structures.

12.4 Performance of the Proposed Control Laws

To be able to have fully autonomous ROV operations, it is imperative that the vessel states are properly controlled. For operations at exposed locations, this is a challenging task.

During practical experiments, variations of classical PID control was used. The performance of the controllers were good, although not perfect. In depth, the reference was steady, and the PI depth controller had a satisfying response. The PID heading controller performed well at the fish farm, but had slightly underdamped response during the basin trials. Lastly, the velocity controllers performed decently, but could definitely been better. At the basin trials, they weren't able to follow rapid changes in reference, while the fish farm trials had a steady-state error.

The main obstacle for the velocity controllers at the fish farm trials, was the measurement noise. The logical first step to achieve better control is to filter the velocity feedback. Then it is might be possible to find gains in heading and velocity which yields a better response. It should be noted that even though the heading and velocity wasn't perfectly controlled, the overall performance of the system was good, which suggests robustness.

Compared to the PID controllers, the response of the suggested 1st order SMC control laws, as well as the STA control law, was excellent during simulations. For the 1st order SMC, however, the depth control law requires a good estimate of the restoring forces vector $\boldsymbol{g}(\boldsymbol{\eta})$, else a bias is observed. This limits the flexibility of the control law. The velocity controllers had integral gain in the sliding variable. This results in a steady-state error for the sliding variable. Still, the tracking error converges to the origin.

The suggested STA control law is based upon the work in [39], [56] and [7]. In [56], a Lyapunov-based proof for the STA control law with adaptive gain is given, and in [7] a feedback linearizing control law brings the dynamics of a AIAUV to a form which is consistent with the stability analysis in [56], and consequently yields asymptotical stability. The sliding variables and dynamics of this thesis is not on the form of [56], and a stability analysis is yet to be developed. However, simulations shows excellent response in all 4 controlled DOFs.

As the STA control laws had adaptive gains, they required minimal tuning effort before good control was achieved during simulations. The adaptive gains quickly converged to values which yielded good response. However, the thesis findings also points to the positive semi-definiteness of the adaptive law as a potential problem. Large changes in reference leads to increasing gains, which can ultimately lead to high-gain instability. Potential solutions may be to use a fixed gain or utilize the more general adaptive law given by [57].

Because the nature of the proposed sliding mode controllers, they are very reactive and will often lead to a high input activity. They therefore require reliable measurements, and measurement noise may decrease the performance. Before practical experiments are undertaken, filtering of the velocity measurements would be wise.

12.5 Robustness to Environmental Loads

As stated, the environmental loads at exposed aquaculture sites may be challenging. Due to the severity of wind, waves and weather, aquaculture operations often cannot be conducted because of safety reasons. Autonomous operations that are able to handle the severe disturbances may expand the weather window, as well increase safety due to the possibility of unmanned operations.

The Argus Mini is a small and light weight ROV compared to most working class ROVs. With a size of less than half a cubic meter and a mass of 90kg, it is heavily influenced by external forces. However, as the ROV has a relatively small inertia, it is reactive to the applied thruster forces and moments, and it is possible to design control systems with a large bandwidth. A well designed control system should therefore be able to handle most time-varying disturbances if the magnitude of the disturbances are not too large. If the magnitude of the environmental loads grows too large, ROV operations becomes impossible.

Both currents and waves may deform a net cage. Therefore, the absolute position of the net pen is unknown. The net pen approximation method, however, only relies on the net pen position relative to the ROV. The proposed net pen approximation should therefore be robust to current-induced deformations. As previously stated, extreme deformations, with phenomenons such as acute angles, may be a limitation to the accuracy of the net pen approximation.

The guidance law is designed in such a way that it is capable of path following with environmental disturbances without the need for integral action. Hence, the GNC system should handle time-varying disturbances as long as they are within the bandwidth of the velocity controllers. This can include currents which vary in space and time, a phenomenon which can be observed in net pens.

Experiments show that the net pen following algorithm with PID performs well in the presence of environmental loads, in spite of measurement noise and imperfect tuning. With better state estimates and state controllers, the performance and robustness is expected to rise further.

From the trials and simulations, one can therefore conclude that the ROV is able to perform autonomous net pen inspections in the presence of time-varying disturbances. With extreme exposure, however, the magnitude of the loads is expected to become too great for the ROV to handle. In large or extreme exposure, the main obstacle for ROV operations may in fact be the launch-and-recovery operations. Today, these require manual operations and may be hazardous. Truly unmanned ROV operations with autonomous deployment and recovery may expand the weather window further.

Chapter 13

Conclusions

In this thesis, several topics have been investigated. The main task was to design and implement ROV control systems which enables autonomous inspection of aquaculture net pens. Autonomous operations in aquaculture could increase safety, increase the weather window and lower operational costs, and autonomous net pen inspection is a step towards this goal.

As the shape of the net pen is time-varying and influenced by environmental loads, its position will be unknown. A ROV guidance law is therefore not able to rely on geo-referenced position measurements. The thesis proposes to use a DVL system to measure the traveled distance of the DVL beams to the net pen. From four returning beams, it is possible to approximate the net pen surface as a plane, and furthermore calculate the ROV position and attitude relative to this plane.

Secondly, a guidance law is presented which guides the ROV to traverse the approximated net pen surface with a constant distance, speed and heading relative to the net pen. The guidance law is based upon the classical line-of-sight law, but utilizes that the ROV is actuated in 4 DOFs. The proposed law will minimize the crosstrack error independent of the ROV heading. This allows the camera viewpoint to be directed towards the path surrounding, which is beneficial in many types of inspection operations.

Finally, two different control laws for the ROV states was designed and tested. The first control law was a 1st order sliding mode controller. The control law yielded good results through simulations. However, the suggested control law is not model free, and performance was decreased with an imperfect model. The suggested velocity controllers has a integral term in the sliding variable. While the sliding variables did not converge to the origin, the integral term ensured that the tracking error converged to the origin.

The second law which was tested was a super-twisting algorithm with adaptive gain. Simulation results yielded excellent results. The tracking errors converged to the origin and was able to follow time-varying references. However, the adaptive law is positive semi-definite, which may be problematic in some type of operations. The adaptive gain will grow larger when the sliding variable is outside a region centered around the origin, and for example a set of steps in reference may lead to high-gain instability.

The proposed net pen approximation, guidance law and control laws have been tested in simulations. Simulations yields good results, and the ROV is able to autonomously traverse the net pen, also in the presence of time-varying disturbances.

Furthermore, practical experiments of the net pen following system has been tested at a water basin and a full-scale fish farm. The experiments supports the simulation results, and the ROV was able to safely traverse the net pen. The experiments showed that the DVL successfully interacted with the net, and the net pen approximation worked good. The net pen following was tested with PID controllers, whose performance was decent, but not perfect. A decrease in velocity control lead to a decrease in the performance of the guidance law, which was expected. Nevertheless, the overall performance was good and even during the worst-case performance, the ROV stayed within a safe distance from the net pen.

The experiments were conducted in an empty fish cage without the presence of biomass. As the salmon swim bladder may interact with the DVL measurements, net pen following in the presence of fish may be a potential problem and is the subject of further testing. Furthermore, the DVL measured velocity was affected by noise, and filtering is required in order to achieve better control.

13.1 Future Work

In practical experiments so far, the net pen following system has been tested without state estimators and wave filters. Instead, the measurements have been fed directly back to the control system. Therefore, measurement errors and noise are induced into the motion control system, and as expected decreases performance. To increase the performance, the control system should be expanded to include a state observer and possibly wave filters. The design of this is already underway, and testing is to be done in the next months.

The next step for experiments with the net pen following method, is to test the net pen approximation with biomass present. The method depends on reliable DVL measurements, and salmon may interfere with this. Hopefully, this can also be tested during the spring. If tests are successful, the author argues that the presented method is indeed capable of performing automated net pen inspection tasks.

While simulations and experiments show that the net pen approximation performs satisfyingly, it can only give information about a local area of the net pen. Other methods may produce a better approximation. One example is to use a multi-beam sonar, which would provide a higher-order approximation. Another example may be to window several DVL measurements and perform SLAM from the stored measurements. This requires geo-referenced positions, either by measurement or by estimation. Another area for improvement, is to have some method which foresees the approaching net pen structure. From this, it is possible to implement some feedforward action, which would make the net pen following system more robust to deformations in the net pen.

A natural next step for the proposed control laws is to perform an analysis of their stability properties. For the 1st order SMC control law, the stability inside the boundary layer is of interest, while the stability analysis of the STA law is yet to be developed. Furthermore, it would be exciting to see the performance of the control laws in practice, and compared to that of the PID laws.

The proposed guidance law works very well. However, due to the iterative nature of the net pen inspection task, it may be possible to perform some learning strategy instead. In [9], a racing car iteratively learns the best way to complete a race track. To follow this example, an idea is for the ROV to use optimization to iteratively learn the best way to traverse the net pen. This approach would most likely require estimates of the ROV position.

The net pen following algorithm is a step towards further autonomy in aquaculture. The camera images from the ROV during net pen following appear clear, and the net pen in front of the ROV is easy visible, see Figure 13.1. This suggests that it is possible to use computer vision to autonomously detect holes. Furthermore, this can easily be coupled with a reaction from the ROV, such as entering dynamic positioning if a hole is detected. Further challenges towards true autonomy and remote operations in aquaculture would be launch-and-recovery of the ROV, cooperation with other vehicles or ROV repair operations with the use of robotic manipulators.

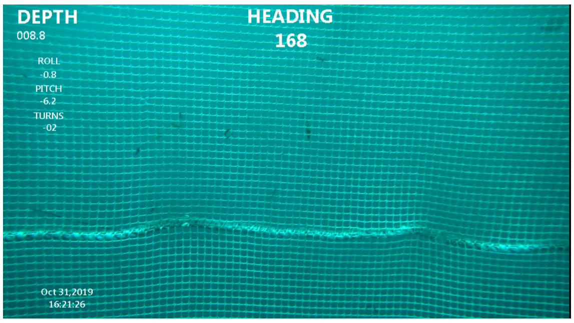

Figure 13.1: Images from ROV front camera during net pen following.

Appendices

Appendix A

Proof of Theorem 2

Vehicle model and assumptions

This proof is based upon the proof given in [13]. Consider a 3DOF maneuvering model under the influence of a constant and irrotational current with the kinematics in component form given by

$$\begin{aligned} \dot{x} =& u_r \cos(\psi) - v_r \sin(\psi) + V_x \\ \dot{y} =& u_r \sin(\psi) + v_r \cos(\psi) + V_y \\ \dot{\psi} =& r \end{aligned} \tag{A.1}$$

where $\boldsymbol{V}_c = [V_x, V_y, 0]^T$ is the current velocity in $\{n\}$.

Define the velocity tracking errors $\tilde{u}_r \triangleq u_r - u_{rd}, \tilde{v}_r \triangleq v_r - v_{rd}$. Furthermore, consider the case where control laws have been designed to ensure that $\boldsymbol{\xi} = \mathbf{0}$ is an UGAS equilibrium point, where $\boldsymbol{\xi} = [\tilde{u}_r, \tilde{v}_r]^T$. The speed of the current is bounded by $V_{\max} \geq \sqrt{V_x^2 + V_y^2}$, and $\dot{\boldsymbol{V}}_c = \mathbf{0}$.

Consider the case where the desired path is a straight line, and that the desired heading is normal to the path, with path following in the starboard direction. In other words, the desired heading is given by

$$\psi_d \triangleq \gamma_p - \pi/2, \tag{A.2}$$

where γ_p is the path tangential angle.

Guidance law

Let the guidance law be given by

$$\begin{aligned} u_{rd} &= U_{rd} \cos\left(-\tilde{\psi} + \frac{\pi}{2} - \arctan\left(\frac{y_e + \sigma y_{\text{int}}}{\Delta}\right)\right) \\ v_{rd} &= U_{rd} \sin\left(-\tilde{\psi} + \frac{\pi}{2} - \arctan\left(\frac{y_e + \sigma y_{\text{int}}}{\Delta}\right)\right) \\ \dot{y}_{\text{int}} &= \frac{\Delta y_e}{\Delta^2 + (y_e + \sigma y_{\text{int}})^2} \end{aligned} \tag{A.3}$$

where σ, Δ are positive constants and $U_{rd} > 0$ the desired relative speed.

Crosstrack error dynamics

The dynamics of the crosstrack error is given by

$$\dot{y}_e = -\dot{x}\sin\left(\gamma_p\right) + \dot{y}\cos\left(\gamma_p\right) \tag{A.4}$$

Inserting the desired heading and Eq. (A.1) gives

$$\begin{aligned} \dot{y}_e =& -\dot{x}\cos\left(\psi_d\right) - \dot{y}\sin\left(\psi_d\right) \\ =& -\left[u_r\cos(\psi) - v_r\sin(\psi) + V_x\right]\cos(\psi_d) \\ & -\left[u_r\sin(\psi) + v_r\cos(\psi) + V_y\right]\sin(\psi_d) \\ =& -u_r\left[\cos(\psi)\cos(\psi_d) + \sin(\psi)\sin(\psi_d)\right] \\ & + v_r\left[\sin(\psi)\cos(\psi_d) - \cos(\psi)\sin(\psi_d)\right] - \begin{bmatrix} V_x & V_y \end{bmatrix}\begin{bmatrix}\cos(\psi_d) \\ \sin(\psi_d)\end{bmatrix} \end{aligned} \tag{A.5}$$

By introducing the tracking errors, this can be written as

$$\begin{aligned} \dot{y}_e =& -\left(u_{rd} + \tilde{u}_r\right)\left[\cos(\psi_d + \tilde{\psi})\cos(\psi_d) + \sin(\psi_d + \tilde{\psi})\sin(\psi_d)\right] \\ & + \left(v_{rd} + \tilde{v}_r\right)\left[\sin(\psi_d + \tilde{\psi})\cos(\psi_d) - \cos(\psi_d + \tilde{\psi})\sin(\psi_d)\right] \\ & - \begin{bmatrix} V_x & V_y \end{bmatrix}\begin{bmatrix}\cos(\psi_d) \\ \sin(\psi_d)\end{bmatrix} \end{aligned} \tag{A.6}$$

By using the standard trigonometric identities

$$\begin{aligned} \sin(a \pm b) &= \sin(a)\cos(b) \pm \cos(a)\sin(b) \\ \cos(a \pm b) &= \cos(a)\cos(b) \mp \sin(a)\sin(b) \end{aligned} \tag{A.7}$$

this can be further reduced to

$$\begin{aligned} \dot{y}_e =& -\left(u_{rd} + \tilde{u}_r\right)\cos(\tilde{\psi}) + \left(v_{rd} + \tilde{v}_r\right)\sin(\tilde{\psi}) - \begin{bmatrix} V_x & V_y \end{bmatrix}\begin{bmatrix}\cos(\psi_d) \\ \sin(\psi_d)\end{bmatrix} \\ =& -u_{rd}\cos(\tilde{\psi}) + v_{rd}\sin(\tilde{\psi}) - \begin{bmatrix} V_x & V_y \end{bmatrix}\begin{bmatrix}\cos(\psi_d) \\ \sin(\psi_d)\end{bmatrix} \\ & - \tilde{u}_r\cos(\tilde{\psi}) + \tilde{v}_r\sin(\tilde{\psi}) \end{aligned} \tag{A.8}$$

Introducing the guidance law yields

$$\begin{aligned}\dot{y}_e =& -U_{rd}\cos\left(-\tilde{\psi}+\frac{\pi}{2}-\arctan\left(\frac{y_e+\sigma y_{\text{int}}}{\Delta}\right)\right)\cos(\tilde{\psi})\\ &+U_{rd}\sin\left(-\tilde{\psi}+\frac{\pi}{2}-\arctan\left(\frac{y_e+\sigma y_{\text{int}}}{\Delta}\right)\right)\sin(\tilde{\psi})\\ &-\begin{bmatrix}V_x & V_y\end{bmatrix}\begin{bmatrix}\cos(\psi_d)\\ \sin(\psi_d)\end{bmatrix}-\tilde{u}_r\cos(\tilde{\psi})+\tilde{v}_r\sin(\tilde{\psi})\\ =&U_{rd}\sin\left(-\arctan\left(\frac{y_e+\sigma y_{\text{int}}}{\Delta}\right)\right)-\begin{bmatrix}V_x & V_y\end{bmatrix}\begin{bmatrix}\cos(\psi_d)\\ \sin(\psi_d)\end{bmatrix}\\ &-\tilde{u}_r\cos(\tilde{\psi})+\tilde{v}_r\sin(\tilde{\psi})\\ =&-\frac{U_{rd}}{\sqrt{\Delta^2+(y_e+\sigma y_{\text{int}})^2}}(y_e+\sigma y_{\text{int}})-\begin{bmatrix}V_x & V_y\end{bmatrix}\begin{bmatrix}\cos(\psi_d)\\ \sin(\psi_d)\end{bmatrix}\\ &-\tilde{u}_r\cos(\tilde{\psi})+\tilde{v}_r\sin(\tilde{\psi})\end{aligned} \tag{A.9}$$

Furthermore, define

$$u_{cd}\triangleq\cos(\psi_d)V_x+\sin(\psi_d)V_y \tag{A.10}$$

which is recognized as the component of the current velocity which works normal to the desired path.

Finally, we are left with the system

$$\begin{aligned}\dot{y}_{\text{int}} &= \frac{\Delta y_e}{\Delta^2+(y_e+\sigma y_{\text{int}})^2}\\ \dot{y}_e &= -\frac{U_{rd}}{\sqrt{\Delta^2+(y_e+\sigma y_{\text{int}})^2}}(y_e+\sigma y_{\text{int}})-u_{cd}-\tilde{u}_r\cos(\tilde{\psi})+\tilde{v}_r\sin(\tilde{\psi})\end{aligned} \tag{A.11}$$

Uniqueness of equilibrium point

It can be shown that on the manifold $\boldsymbol{\xi}=\mathbf{0}$, the system (A.11) has a unique equilibrium point at

$$\begin{aligned}y_e^{\text{eq}} =&0\\ y_{\text{int}}^{\text{eq}} =&-\frac{\Delta}{\sigma}\frac{u_{cd}}{\sqrt{U_{rd}^2-u_{cd}^2}}\end{aligned} \tag{A.12}$$

From (A.11), its trivial to see that $y_e^{\text{eq}}=0$. The calculation of the equilibrium point $y_{\text{int}}^{\text{eq}}$ yields

$$\frac{s}{\sqrt{1+s^2}}=-\frac{u_{cd}}{U_{rd}} \tag{A.13}$$

where $s\triangleq\sigma y_{\text{int}}^{\text{eq}}/\Delta$. This yields

$$s=\pm\frac{u_{cd}}{\sqrt{U_{rd}^2-u_{cd}^2}} \tag{A.14}$$

However, from (A.13) in can be seen that s and u_{cd} will have opposite signs, thus confirming the uniqueness of the equilibrium in (A.12).

Error variables and cascaded system

Introduce the error variables

$$\begin{aligned} e_1 &\triangleq y_{\text{int}} - y_{\text{int}}^{\text{eq}} \\ e_2 &\triangleq y_e + \sigma e_1 \end{aligned} \tag{A.15}$$

Since the current is irrotational and the desired path straight, we have $\dot{y}_{\text{int}}^{\text{eq}} = 0$. The error variable dynamics is then given by

$$\begin{aligned} \dot{e}_1 &= -\frac{\sigma\Delta}{\Delta^2 + (e_2 + \sigma y_{\text{int}}^{\text{eq}})^2} e_1 + \frac{\Delta}{\Delta^2 + (e_2 + \sigma y_{\text{int}}^{\text{eq}})^2} e_2 \\ \dot{e}_2 &= -\frac{\sigma^2\Delta}{\Delta^2 + (e_2 + \sigma y_{\text{int}}^{\text{eq}})^2} e_1 - \frac{U_{rd}\sqrt{\Delta^2 + (e_2 + \sigma y_{\text{int}}^{\text{eq}})^2} - \sigma\Delta}{\Delta^2 + (e_2 + \sigma y_{\text{int}}^{\text{eq}})^2} e_2 \\ &\quad - f(e_2) u_{rd} - \tilde{u}_r \cos(\tilde{\psi}) + \tilde{v}_r \sin(\tilde{\psi}) \end{aligned} \tag{A.16}$$

where

$$f(e_2) \triangleq 1 - \frac{\sqrt{\Delta^2 + (\sigma y_{\text{int}}^{\text{eq}})^2}}{\sqrt{\Delta^2 + (e_2 + \sigma y_{\text{int}}^{\text{eq}})^2}} \tag{A.17}$$

Furthermore, $f(e_2)$ is bounded by

$$|f(e_2)| \leq \frac{|e_2|}{\sqrt{\Delta^2 + (e_2 + \sigma y_{\text{int}}^{\text{eq}})^2}} \tag{A.18}$$

It can be shown that (A.18) holds by squaring both side of the equation 2 times.

Furthermore, this can be written as

$$\begin{bmatrix} \dot{e}_1 \\ \dot{e}_2 \end{bmatrix} = \boldsymbol{f}_1(t, e_2) + \boldsymbol{g}(t, \tilde{\psi})\boldsymbol{\xi} \tag{A.19}$$

with

$$\begin{aligned} \boldsymbol{f}_1(t, e_2) &\triangleq \begin{bmatrix} -\frac{\sigma\Delta}{\Delta^2+(e_2+\sigma y_{\text{int}}^{\text{eq}})^2} e_1 + \frac{\Delta}{\Delta^2+(e_2+\sigma y_{\text{int}}^{\text{eq}})^2} e_2 \\ -\frac{\sigma^2\Delta}{\Delta^2+(e_2+\sigma y_{\text{int}}^{\text{eq}})^2} e_1 - \frac{U_{rd}\sqrt{\Delta^2+(e_2+\sigma y_{\text{int}}^{\text{eq}})^2} - \sigma\Delta}{\Delta^2+(e_2+\sigma y_{\text{int}}^{\text{eq}})^2} e_2 - f(e_2) u_{rd} \end{bmatrix} \\ \boldsymbol{g}(t, \tilde{\psi}) &\triangleq \begin{bmatrix} -\cos(\tilde{\psi}) \\ \sin(\tilde{\psi} \end{bmatrix} \end{aligned} \tag{A.20}$$

This can be seen as a cascaded system where the nominal system

$$\begin{bmatrix} \dot{e}_1 \\ \dot{e}_2 \end{bmatrix} = \boldsymbol{f}_1(t, e_2) \tag{A.21}$$

is perturbed by the tracking errors through the term $\boldsymbol{g}(t, e_2)\boldsymbol{\xi}$.

Stability of cascaded system

Lemma 2. The nominal system (A.21) is uniformly globally asymptotically stable (UGAS) and uniformly locally exponentially stable (ULES).

Proof. Consider the radially unbounded, positive definite Lyapunov function candidate

$$V = \frac{1}{2}\sigma^2 e_1^2 + \frac{1}{2}e_2^2 \tag{A.22}$$

The time-derivative of V is

$$\begin{aligned}\dot{V} =& -\frac{\sigma^3\Delta}{\Delta^2 + (e_2 + \sigma y_{\text{int}}^{\text{eq}})^2}e_1^2 - \frac{U_{rd}\sqrt{\Delta^2 + (e_2 + \sigma y_{\text{int}}^{\text{eq}})^2} - \sigma\Delta}{\Delta^2 + (e_2 + \sigma y_{\text{int}}^{\text{eq}})^2}e_2^2 \\ &- f(e_2)u_{rd}e_2 \\ \leq& -\sigma^3\Delta\bar{e}_1^2 - \left[U_{rd}\sqrt{\Delta^2 + (e_2 + \sigma y_{\text{int}}^{\text{eq}})^2} - \sigma\Delta\right]\bar{e}_2^2 + |f(e_2)||e_2|V_{\max} \\ \leq& -\sigma^3\Delta\bar{e}_1^2 - \Delta\left(U_{rd} - V_{\max} - \sigma\right)\bar{e}_2^2\end{aligned} \tag{A.23}$$

where

$$\begin{aligned}\bar{e}_1 &\triangleq \frac{e_1}{\sqrt{\Delta^2 + (e_2 + \sigma y_{\text{int}}^{\text{eq}})^2}} \\ \bar{e}_2 &\triangleq \frac{e_2}{\sqrt{\Delta^2 + (e_2 + \sigma y_{\text{int}}^{\text{eq}})^2}}\end{aligned} \tag{A.24}$$

This can be written as

$$\dot{V} \leq -\begin{bmatrix}\bar{e}_1 & \bar{e}_2\end{bmatrix}\begin{bmatrix}\sigma^3\Delta & 0 \\ 0 & \Delta(U_{rd} - V_{\max} - \sigma)\end{bmatrix}\begin{bmatrix}\bar{e}_1 \\ \bar{e}_2\end{bmatrix} = -\begin{bmatrix}\bar{e}_1 & \bar{e}_2\end{bmatrix}\boldsymbol{W}\begin{bmatrix}\bar{e}_1 \\ \bar{e}_2\end{bmatrix} \tag{A.25}$$

By choosing $U_{rd} > \sigma + V_{\max}$, $\boldsymbol{W}$ is positive definite. The positive definiteness of $\boldsymbol{W}$ ensures that (A.21) is uniformly globally asymptotically stable, UGAS.

Furthermore, the inequality $\dot{V} \leq -\bar{\lambda}_1|\bar{e}_1|^2 - \bar{\lambda}_2|\bar{e}_2|^2$ holds in a neighborhood of the origin for some constants $\bar{\lambda}_1, \bar{\lambda}_2 > 0$ and thus in any ball $\mathcal{B}_r \triangleq \{|e_2| \leq r\}, r > 0$, $\dot{V}$ can be upper bounded by $\dot{V} \leq -\lambda_1|e_1|^2 - \lambda_2|e_2|^2$, where $\lambda_i = \bar{\lambda}_i/((r + y_{\text{int}}^{\text{eq}})^2 + \Delta^2)$, $i = 1, 2$. This gives that the system is also uniformly locally exponentially stable, ULES. □

Finally the stability of the cascaded system (A.19) is analyzed. Clearly, $\boldsymbol{g}(t, e_2)$ is bounded. Furthermore, $\boldsymbol{\xi}$ is bounded and the origin of $\boldsymbol{\xi}$ is UGAS. Then, by Theorem 2 in [48] and Lemma 8 in [47], the origin of the cascaded system (A.19) is both UGAS and ULES. The convergence of e_1 and e_2 to their origins yields the convergence of y_e to zero and y_{int} to $y_{\text{int}}^{\text{eq}}$. By switching the sign in front of $\pi/2$ in Eqs. (A.2)-(A.3), the same can be shown for path following towards the port side. This concludes the proof. □

Appendix B

Paper to be Submitted to IEEE Journal of Oceanic Engineering

This appendix includes a draft of the paper which is to be submitted to IEEE Journal of Oceanic Engineering. It is written in co-operation with Dr. Walter Caharija and Prof. Kristin Ytterstad Pettersen.

Bibliography

[1] G. Antonelli. *Underwater Robots.* Springer, 2018.

[2] B. O. Arnesen, S. S. Sandøy, I. Schjølberg, J. A. Alfredsen, and I. B. Utne. "Probabilistic Localization and Mapping of Flexible Underwater Structures using Octomap." In: *2018 European Control Conference.* (Limassol, Cyprus). IEEE, June 2018.

[3] World Bank. "Prospects for Fisheries and Aquaculture." In: *World Bank Report* 83177 (2013).

[4] S. Barkby, S. Williams, O. Pizarro, and M. Jakuba. "An Efficitent Approach to Bathymetric SLAM." In: *The 2009 IEEE/RSJ Internation Conference on Intelligent Robots and Systems.* (St. Louis, USA). Oct. 2009, pp. 219–224.

[5] G. Bartolini, A. Pisano, E. Punta, and E. Usai. "A survey of applications of second-order sliding mode control to mechanical systems." In: *International Journal of Control* 76 (2003), pp. 875–892.

[6] E. Børhaug, A. Pavlov, and K. Y. Pettersen. "Integral LOS Control for Path Following of Underactuated Marine Surface Vessels in the Presence of Constant Ocean Currents." In: *Proc.of the 47th IEEE Conference on Decision and Control.* (Cancun, Mexico). Dec. 2008.

[7] I. L. G. Borlaug, K. Y. Pettersen, and J. T. Gravdahl. "Trajectory tracking for an articulated intervention AUV using a super-twisting algorithm in 6DOF." In: *11th IFAC Conference on Control Applications in Marine Systems, Robotics, and Vehicles.* (Opatija, Croatia). Vol. 11. Sept. 2018, pp. 311–316.

[8] M. Breivik and T. I. Fossen. "Guidance-based path following for autonomous underwater vehicles." In: *Proc.of OCEANS 2005 MTS/IEEE.* Sept. 2005, 2807–2814 Vol. 3.

[9] M. Brunner, U. Rosolia, J. Gonzales, and F. Borrelli. "Repetitive learning model predictive control: An autonomous racing example." In: *2017 IEEE 56th Annual Conference on Decision and Control (CDC).* (Melbourne, Australia). IEEE, Dec. 2017, pp. 1157–1162.

[10] M. Bujarbaruah, X. Zhang, U. Rosolia, and F. Borrelli. "Adaptive MPC for Iterative Tasks." In: *2018 IEEE Conference on Decision and Control (CDC).* (Miami Beach, Fl, USA). Dec. 2018.

[11] M. Caccia, R. Bono, G. Bruzzone, and G. Veruggio. "Bottom-following for remotely operated vehicles." In: *Control Engineering Practice* 11 (2003), pp. 461–470.

[12] W. Caharija. "Integral Line-of-Sight Guidance and Control of Underactuated Marine Vehicles." PhD thesis. Norwegian University of Science and Technology, 2014.

[13] W. Caharija, K. Y. Pettersen, M. Bibuli, P. Calado, E. Zereik, J. Braga, J. T. Gravdahl, A. J. Sørensen, M. Milovanović, and G. Bruzzone. "Integral Line-of-Sight Guidance and Control of Underactuated Marine Vehicles: Theory, Simulations, and Ex-

periments." In: *IEEE Transactions on Control Systems Technology* 24.5 (Sept. 2016), pp. 1623–1642.

[14] W. Caharija, K. Y. Pettersen, and J. T. Gravdahl. "Path Following of Marine Surface Vessels with Saturated Transverse Actuators." In: *American Control Conference.* (Washington, DC, USA). IEEE, 2013, pp. 546–553.

[15] W. Caharija, A. J. Sørensen, K. Y. Pettersen, M. Greco, and J. T. Gravdahl. "Path Following Control of Underactuated Surface Vessels in the Presence of Multiple Disturbances." In: *18th European Control Conference.* (Napoli, Italy). June 2019, pp. 2551–2558.

[16] M. Candeloro, F. Dezi, A. J. Sørensen, and S. Longhi. "Analysis of Multi-objective Observer for UUVs." In: *3rd IFAC Workshop on Navigation, Guidance and Control of Underwater Vehicles.* (Porto, Portugal). Ed. by Fernando Lobo Pereira. Elsevier Ltd., 2012, pp. 343–348.

[17] M. Candeloro, A. J. Sørensen, S. Longhi, and F. Dukan. "Observers for Dynamic Positioning of ROVs with Experimental Results." In: *9th IFAC Conference on Manoeuvring and Control of Marine Craft.* (Arenzano, Italy). Ed. by G. Bruzzone and M. Caccia. Elsevier Ltd., 2012, pp. 85–90.

[18] F. Dukan. "ROV Motion Control Systems." PhD thesis. Norwegian University of Science and Technology, 2014.

[19] F. Dukan and A. J. Sørensen. "Sea Floor Geometry Approximation and Altitude Control of ROVs." In: *Control Engineering Practice* 29 (Aug. 2014), pp. 135–146.

[20] O. Egeland and J. T. Gravdahl. *Modeling and Simulation for Automatic Control.* Marine Cybernetics, 2002.

[21] Industri Energi. *Over halvparten av innaskjærsdykkerne har fryktet for liv og helse.* 2018. URL: `https://www.industrienergi.no/nyhet/over-halvparten-av-innaskjaersdykkerne-har-fryktet-for-liv-og-helse/` (visited on 11/18/2019).

[22] O. M. Faltinsen. *Sea Loads on Ships and Offshore Structures.* Cambridge Ocean Technology. Cambridge University Press, 1990.

[23] Martin Føre, Kevin Frank, Tomas Norton, Eirik Svendsen, Jo Arve Alfredsen, Tim Dempster, Harkaitz Eguiraun, Win Watson, Annette Stahl, Leif Magne Sunde, Christian Schellewald, Kristoffer R. Skøien, Morten O. Alver, and Daniel Berckmans. "Precision fish farming: A new framework to improve production in aquaculture." In: *Biosystems Engineering* 173 (2018), pp. 176–193.

[24] T. I. Fossen. *Handbook of Marine Craft Hydrodynamics and Motion Control.* John Wiley & Sons, Ltd., 2011.

[25] T. I. Fossen, M. Breivik, and R. Skjetne. "Line-of-Sight Path Following of Underactuated Marine Craft." In: *Proc.of the IFAC MCMC'03.* (Girona, Spain). IFAC, 2003.

[26] T. I. Fossen and K. Y. Pettersen. "On Uniform Semiglobal Exponential Stability (USGES) of Proportional Line-of-Sight Guidance Laws." In: *Automatica* 50 (2014), pp. 2912–2917.

[27] E. Fredriksen and K.Y. Pettersen. "Global κ-exponential way-point maneuvering of ships: Theory and experiments." In: *Automatica* 42.4 (2006), pp. 677–687.

[28] L. C. Gansel, S. Rackebrandt, F. Oppedal, and T. A. McClimans. "Flow Fields Inside Stocked Fish Cages and the Near Environment." In: *Journal of Offshore Mechanics and Arctic Engineering* 136 (Aug. 2014).

[29] P. Ioannou and J. Sun. *Robust Adaptive Control.* Dover Publications, 1996.

[30] Ø. Jensen, T. Dempster, Eva Thorstad, I. Uglem, and A. Fredheim. “Escapes of fish from Norwegian sea-cage aquaculture: causes, consequences, and prevention.” In: *Aquaculture Environment Interactions* 1 (Aug. 2010), pp. 71–83.

[31] T. A. Johansen and T. I. Fossen. “Control Allocation - A Survey.” In: *Automatica* 49 (5 2013), pp. 1087–1103.

[32] H. K. Khalil. *Nonlinear Systems.* Prentice Hall, Inc., 2002.

[33] P. Klebert, Ø. Patursson, P. C. Endresen, P. Rundtop, J.Birkevold, and H. W. Rasmussen. “Three-dimensional deformation of a large circular flexible sea cage in high currents: Field experiment and modeling.” In: *Ocean Engineering* 104 (2015), pp. 511–520.

[34] D. Kristiansen, V. Aksnes, B. Su, P. Lader, and H. V. Bjelland. “Environmental Description inf the Design of Fish Farms at Exposed Locations.” In: *Proc. ASME 2017 36th International Conference on Ocean, Offshore and Arctic Engineering.* (Trondheim, Norway). ASME, June 2017.

[35] D. Kristiansen, P. Lader, Ø. Jensen, and D. Fredriksson. “Experimental Study of An Aquaculture Net Cage in Waves and Current.” In: 29.3 (2014), pp. 324–340.

[36] P. Lader, T. Dempster, A. Fredheim, and Ø. Jensen. “Current induced net defomrations in full-scale sea-cages for Atlantic salmon (Salmo salar).” In: *Aquaculture Engineering 38* 38 (2008), pp. 52–65.

[37] P. Lader, D. Kristiansen, M. Alver, H. V. Bjelland, and D. Myrhaug. “Classification of Aquaculture Locations in Norway With Respect to Wind Wave Exposure.” In: *Proc. ASME 2017 36th International Conference on Ocean, Offshore and Arctic Engineering.* 2017.

[38] K. S. Lee, I. Chin, and H. J. Lee. “Model Predictive Control Technique Combined with Iterative Learning for Batch Processes.” In: *AIChE* 45 (10 1999), pp. 2175–2187.

[39] A. Levant. “Sliding order and sliding accuracy in sliding mode control.” In: *International Journal of Control* 58 (1993), pp. 1247–1263.

[40] A. Loria and E. Panteley. “Cascaded nonlinear time-varying systems: analysis and design.” In: *Advanced Topics in Control Systems Theory.* Ed. by F. Lamnabhi-Lagarrigue, A. Loria, and E. Panteley. London: Springer Verlag, 2004. Chap. 2, pp. 23–64.

[41] S. Moe, W. Caharija, K. Y. Pettersen, and I. Schjølberg. “Path Following of Underactuated Marine Surface vessels in the Presence of Unknown Ocean Currents.” In: *American Control Conference.* (Portland, OR, USA). IEEE, 2014, pp. 3856–3861.

[42] S. Moe, K. Y. Pettersen, T. I. Fossen, and J. T. Gravdahl. “Line-of-sight curved path following for underactuated USVs and AUVs in the horizontal plane under the influence of ocean currents.” In: *2016 24th Mediterranean Conference on Control and Automation (MED).* June 2016, pp. 38–45.

[43] H. Moe-Føre, A. Fredheim, and O. S. Hopperstad. “Structural analysis of aquaculture net cages in current.” In: *Journal of Fluids and Structures* 26 (2010), pp. 503–516.

[44] T. Mylvaganam and A. Astolfi. “A Nash Game Approach to Mixed H_2/H_∞ Control for Input-Affine Nonlinear Systems.” In: *IFAC-PapersOnLine* 49 (18 2016), pp. 1024–1029.

[45] The Society of Naval Architects and Marine Engineers. “Nomenclature for treating the Motion of a Submerged Body Through a Fluid.” In: *Technical and Research Bulletin* 1-5 (1950).

[46] Standard Norge. *"NS 9415:2009 Marine fish farms. Requirements for desing, dimensioning, production, installation and operation.* Norsk Standard No. NS 9415, Norges Standariseringsforbund, 2009.

[47] Elena Panteley, Erjen Lefeber, Antonio Loria, and Henk Nijmeijer. “Exponential Tracking Control of a Mobile Car Using a Cascaded Approach.” In: *IFAC Proceedings Volumes* 31.27 (1998). IFAC Workshop on Motion Control (MC’98), Grenoble, France, 21-23 September, pp. 201–206.

[48] Elena Panteley and Antonio Loria. “On global uniform asymptotic stability of nonlinear time-varying systems in cascade.” In: *Systems & Control Letters* 33.2 (1998), pp. 131–138.

[49] K. Y. Pettersen and E. Lefeber. “Way-point tracking control of ships.” In: *Proc.of the 40th IEEE Conference on Decision and Control.* Vol. 1. Dec. 2001, 940–945 vol.1.

[50] K. J. Reite, M. Føre, K. G. Aarsæther, J. Jensen, P. Rundtop, L. T. Kyllingstad, P. C. Endresen, D. Kristiansen, V. Johansen, and A. Fredheim. “FhSim - Time Domain Simulations of Marine Systems.” In: *Proc.of the ASME 2014 33rd International Conference on Ocean, Offshore and Arctic Engineering.* (San Fransisco, USA). June 2014.

[51] R. Richardsen, M. Stoud Myhre, H. Bull-Berg, and I. L. T. Grindvoll. *Nasjonal betydning av sjømatnæringen - En verdiskapings- og ringvirkningsanalyse med data fra 2016 og 2017.* SINTEF, 2018.

[52] U. Rosolia and F. Borrelli. “Learning Model Predictive Control for Iterative Tasks. A Data-Driven Control Framework.” In: *IEEE Transaction on Automatic Control* 63 (7 2018), pp. 1883–1896.

[53] D. Rudolph and T. A. Wilson. “Doppler Velocity Log Theory and Preliminary Considerations for Design and Construction.” In: *Proc.of Southeastcon 2012.* IEEE, 2012.

[54] P. Rundtop and K. Frank. “Experimental Evaluation of Hydroacoustic Instruments for ROV Navigation Along Aquaculture Net Pens.” In: *Aquaculture Engineering* 74 (Sept. 2016), pp. 143–156.

[55] S. S. Sandøy, T. Matsuda, T. Maki, and I. Schjølberg. “Rao-Blackwellized Particle Filter with Grid-Mapping for AUV SLAM Using Forward-Looking Sonar.” In: *2018 OCEANS - MTS/IEEE Kobe Techno-Oceans.* (Kobe, Japan). IEEE, May 2018.

[56] Y. B. Shtessel, J. A. Moreno, F. Plestan, L. M. Fridman, and A. S. Poznyak. “Supertwisting Adaptive Sliding Mode Control: a Lyapunov Design.” In: *49th IEEE Conference on Decision and Control.* (Atlanta, Ga, USA). Vol. 49. Dec. 2010, pp. 5009–5113.

[57] Y. B. Shtessel, M. Taleb, and F. Plestan. “A novel adaptive-gain supertwisting sliding mode controller: Methodology and application.” In: *Automatica* 48 (5 2012), pp. 759–769.

[58] J. J. E. Slotine and W. Li. *Applied Nonlinear Control.* Prentice Hall, 1991.

[59] E. D. Sontag. “A remark on the converging-input converging-state property.” In: *IEEE Transactions on Automatic Control* 48.2 (Feb. 2003), pp. 313–314.

[60] A. J. Sørensen. “Structural issues in the design and operation of marine control systems.” In: *Annual Reviews in Control* 29 (1 2005), pp. 125–149.

[61] B. Su, K. J. Reite, M. Føre, K. G. Aarsæther, M. Alver, P. C. Endresen, D. Kristiansen, J. Haugen, W. Caharija, and A. Tsarau. “A Multipurpose Framework for Modelling and Simulation of Marine Aquaculture Systems.” In: *International Conference on Offshore Mechanics and Arctic Engineering.* (Glasgow, Scotland). Vol. 6. Dec. 2019.

[62] M. Wrzos-Kaminska, T. Mylvaganam, K. Y. Pettersen, and J. T. Gravdahl. “Collision Avoidance using Mixed H_2/H_∞ Control for and Articulated Intervention-AUV.” 2020.

Herman Bjørn Amundsen

Master's thesis

NTNU
Norwegian University of
Science and Technology